Ph.D thesis

Study of $c\overline{s}$ mesons at KEKB electron-positron collider

Graduate School of Tohoku University
Department of Physics

Yoshinari Mikami

February 2005

Acknowledgment

First of all, I would like to express my special thanks for Prof. Hitoshi Yamamoto. I learned many things from him about not only physics but also humanity. His physics was always interesting and his supervising was always strong. I could write this thesis with his abilities, advice and kindness. Just only as his student, I obtained much profit.

I'm grateful for Prof. Kazuo Abe. He recommended me to study the topic of new phenomena of $c\overline{s}$ mesons because he knew it can contribute our collaboration and the study of new phenomena is interesting with many unknown things. He really contributed on journal publication significantly. I could enjoy studying this new topic thanks to him.

I appreciate the kindness of Prof. A. Yamaguchi. He opened my study intention and his long experience teaches me many important things. Starting hardware experience from his teaching give me much confidence. I will express my thanks to Prof. Kouya Abe. He encouraged me every time from the time I was a student of under-graduated school. His education was always standing on the merits of students. I also express my gratitude to Dr. T. Nagamine. His software ability was great support for Tohoku students. During I was staying in Sendai, I had no concern about problems of programming, networks and computing because he was there. I also appreciate Mrs. K. Tamae. She was very kind from the beginning of my joining in the laboratory of Research Center of Neutrino Science. She encouraged me many times and also having a warm heart for students. I want to thank to old and current Tohoku BELLE's post doctoral researcher and Ph.D students whore Dr. S. Narita, Dr. M. Yamaga, Dr. Tetsuo Abe, Dr. O. Tajima, Peter, Jerry and Manabu Saigo. They are good teammates as Tohoku group and helped me many times.

I'm happy with working in KLM operation. The members, Dr. E. Nakano, Wang san, Dr. I. Higuchi, Fumiaki Handa, Yousuke Yusa, Tapas, Deb, Nitesh and Dash are good colleague for the smooth operation. I hope it is stable up to the end of BELLE operation. I was lucky to join SVD group in a few month to obtain another experience of hardware in BELLE detector. It's the central part of our detector and it was very interesting to join the group in exciting periods. They are hearty group and I especially thank to Prof. J. Haba for giving me such a good chance of experience. I also thank to Sato san who had professional ability in his works.

The staffs of KEK are very productive and friendly. It's hard to list all names but I really appreciates to be surrounded by superior scientists and hearty staffs. Especially those who are the same generations scientists, Dr. I. Nakamura, Dr. Y. Ushiroda, Dr. S. Nishida, Dr. T. Higuchi, Dr. H. Kakuno, ... give me good stimuli and encouraged me with many ways in anytime. There are so many professors who encouraged or helped me in this BELLE Collaboration. I especially appreciate their kindness of Prof. F. Takasaki, Prof. M. Yamauchi, Prof. H. Aihara, Prof. T. Iijima, Prof. Y.J. Kwon, Prof. A. Bonder, Prof. T. Browder, Prof. B. Yabsley, Prof. Y. Sakai, Prof. S. Olsen, Prof. Geroge How, Prof. M. Nakao, Dr. V. Eiges, Dr. Y. Iwasaki, ..., they were very kind, and sometimes even if they had strong attitude against me, it was just aiming for my education. The staffs of KEKB people make great performance for high luminosity. Their achievements are world records and it provides us much profits. We could not make results without their continuous great efforts. The members of KamLAND Collaboration had been great impressive for me. I liked to see their energetic working style during their construction period while I had been studying in Sendai. It was good experience to be same laboratory and staying with them. The staffs and students of Tohoku University are great help for me. I learned ten years in this University and they encouraged, stimulated and opened my scientific interests even if during I was not good student. I especially thanks to teachers during I was in Sendai, Prof. A. Suzuki, Prof. O. Hashimoto, Prof. M. Yamaguchi, Prof. K. Inoue, Prof. J. Shirai, Prof. F. Suekane, Prof. M. Koga, Prof. T. Hayashino, Dr. T. Hasegawa, Dr. S. Hatakeyama, they are kind even though different collaboration and good directors in my home institute.

The roommates of Tsukuba building F2 are good friends in every times. John, Jack, Jerry, Jan, Chinchi, Eric, Enari san, Hokuue kun, Kataoka san, Park san, Saitoh kun, Dr. Y. Unno, Jasna, Craig, Tony, Nick, Tapas, Deb ..., sometimes I came here just to see them. BELLE students, Tohoku students and friends who I could be acquainted with or who is also fighting with science gave me much interests and the list is too long to write here. I especially appreciate for their help of old roommates of Tohoku Ph.D course whore Toshiyuki Iwamoto, Hiroshi Ogawa, Sanshiro Enomoto, Hideki Watanabe, Haruo Ikeda, Yoshihito Gando, and Kyo Nakajima. The friends who played sports together with, who eats lunch or dinner with same table or who discussed issues something about world problems are also too long list and I can remember only girl's names as Chihiro san, S.U. Kataoka san, Imoto san, Jingzhi, Kirika san, Minori san ..., and it's good memory.

I would forget some important names, then it's not due to lack of my memory ability but due to so many good friends were there.

In last, I want to thank to my family for continuously great supports in my long student life. I could write this thesis with them and their love.

February 2005,
Yoshinari Mikami

Abstracts

Measurement of the D_{sJ} Resonance Properties (Phys. Rev. Lett. 92, 012002 (2004))

Abstract(1)

We report measurements of two D_{sJ} resonance's masses, widths, and branching fractions in the continuum production. From the measurements of $D_{sJ}^+(2317) \rightarrow D_s^+\pi^0$ and $D_{sJ}^+(2457) \rightarrow D_s^{*+}\pi^0$, we determine their masses to be $M(D_{sJ}^+(2317)) = 2317.2 \pm 0.5$ (stat) $\pm$ 0.9 (syst) and $M(D_{sJ}^+(2457)) = 2456.5 \pm 1.3$ (stat) $\pm$ 1.3 (syst). We determine the ratio of branching fraction times cross section to be $(Br(D_{sJ}^+(2457) \rightarrow D_s^{*+}\pi^0) \times \sigma(D_{sJ}^+(2457)))/(Br(D_{sJ}^+(2317) \rightarrow D_s^+\pi^0) \times \sigma(D_{sJ}^+(2317))) = 0.29 \pm 0.06$ (stat) ± 0.03 (syst) and $(Br(Ds(2457) \rightarrow D_s\,\pi^0) \times \sigma(D_{sJ}^+(2457)))/(Br(Ds(2317) \rightarrow D_s\,\pi^0) \times \sigma(D_{sJ}^+(2317))) \leq 0.06$ $(90\% CL)$. We set upper limit for the branching fraction ratio to be $(Br(Ds(2457) \rightarrow D_s\pi^0))/(Br(Ds(2457) \rightarrow D_s^*\pi^0)) \leq 0.21$ $(90\% CL)$. We observe for the first time of the decay modes $D_{sJ}^+(2457) \rightarrow D_s\pi^+\pi^-$ and $D_{sJ}^+(2536) \rightarrow D_s\pi^+\pi^-$ modes. We determine the branching fraction ratio to be $(Br(D_{sJ}^+(2536) \rightarrow D_s^+\pi^+\pi^-))/(Br(D_{sJ}^+(2457) \rightarrow D_s^+\pi^+\pi^-)) = 1.05 \pm 0.32\,(stat) \pm 0.06\,(syst)$ and $(Br(D_{sJ}^+(2457) \rightarrow D_s^+\pi^+\pi^-))/(Br(D_{sJ}^+(2457) \rightarrow D_s^{*+}\pi^0)) = 0.14 \pm 0.04\,(stat) \pm 0.02\,(syst)$. We set upper limits for the branching fraction ratio to be $(Br(D_{sJ}^+(2317) \rightarrow D_s^+\pi^+\pi^-))/(Br(D_{sJ}^+(2317) \rightarrow D_s^+\pi^0)) \leq 4 \times 10^{-3}$ (90% $C.L.$). We observe for a radiative decay mode $D_{sJ}^+(2457) \rightarrow D_s^+\gamma$. We determine the branching fraction ratio to be $Br(D_{sJ}^+(2457) \rightarrow D_s^+\gamma)/Br(D_{sJ}^+(2457) \rightarrow D_s^{*+}\pi^0) = 0.55 \pm 0.13$ (stat) $\pm$ 0.08 (syst). We set upper limits for the branching fraction ratio to be $(Br(D_{sJ}(2317)^+ \rightarrow D_s^+\gamma))/(Br(D_{sJ}(2317)^+ \rightarrow D_s^+\pi^0)) \leq 0.05$, $(Br(D_{sJ}^+(2317) \rightarrow D_s^{*+}\gamma))/(Br(D_{sJ}^+(2317) \rightarrow D_s^+\pi^0)) \leq 0.18$ (90% $C.L.$), and $(Br(D_{sJ}^+(2457) \rightarrow D_s^{*+}\gamma))/(Br(D_{sJ}^+(2457) \rightarrow D_s^{*+}\pi^0)) \leq 0.31$ (90% $C.L.$). This analysis is based on 86.9 fb^{-1} taken with the BELLE detector and the KEKB accelerator. These results are consistent with spin-parity assignments of 0^+ for the $D_{sJ}(2317)$ and 1^+ for the $D_{sJ}(2457)$.

Study of $|V_{ub}|$ with Using D_s Endpoint (Very preliminary, BELLE NOTE#690, in progress)

Abstract(2)

We report the study of $b \to u\ D_s^-$ decay using $b \to c\ D_s^-$ endpoint at BELLE experiment. We obtain the CKM matrix elements of $|V_{ub}| = (3.79 \pm 1.67\ \text{(stat)} \pm 0.72\ \text{(syst)} \pm 0.72\ \text{(theo)}) \times 10^{-3}$ as preliminary result. This analysis is based on $(152.0 \pm 0.7) \times 10^6\ B\overline{B}$ pairs collected with the BELLE detector and the KEKB accelerator. (Very Preliminary, BELLE NOTE#690, in progress.)

Contents

List of Figures

List of Tables

Chapter 1

Introduction

(The first part)
Measurement of the D_{sJ} Resonance Properties

1.1 Newly found $c\bar{s}$ states

Recently two new narrow resonances were observed in $D_s^+\pi^0$ and $D_s^{*+}\pi^0$ final state. BaBar collaboration observed new narrow resonance at (2316.8 ± 0.4) MeV/c^2 (less than $D\ K$ mass threshold) from isospin violating $D_{sJ}(2317) \rightarrow D_s^{\pm}\pi^0$ decay. They quote a conservative systematic error in the mass determination of less than 3 MeV/c^2 and conclude the natural width of this state is less than 10 MeV/c^2. CLEO collaboration confirmed this state and claimed the evidence for another state at 2463 MeV/c^2 in $D_s^*\pi^0$. They quote a mass splitting of $D_{sJ}(2317)$ with respect to the D_s to be $350.4 \pm 1.2 \pm 1.0$ MeV/c^2 and its natural width $\Gamma < 7$ MeV at 90% C.L. They find the mass splitting of $D_{sJ}(2463)$ with respect to D_s^{*+} to be $351.6 \pm 1.7(stat) \pm 1.0(syst)$ MeV/c^2 and its natural width $\Gamma < 7$ MeV at 90% C.L.

There is a well established doublet of $J^P = (0^-,\ 1^-)$ which correspond to D_s and $D_s^*(2112)$ in the S-wave of the $c\bar{s}$ system. In the P-wave case, we can consider two doublets of $(0^+,\ 1^+)$ for $j_q = 1/2$ and $(1^+,\ 2^+)$ for $j_q = 3/2$, where j_q denote total light quark angular momentum that is defined by sum of light quark angular momentum and orbital angular momentum of the s quark in the $c\bar{s}$ system as shown in figure 1.1. The conventional states of $D_s(2536)$ and $D_s(2573)$ are suitable to 1^+ and 2^+ in the $L = 1$ states. Ignoring the fact that their masses are lower than expectations based on quark potential models, a natural interpretation for these two new states is that they are 0^+ and 1^+ of $J = 1/2$, $L = 1$ excitations of the $c\bar{s}$ state as shown in figure 1.1, where J and L denote the total angular momentum and orbital angular momentum of the s quark in the $c\bar{s}$ system also as shown in figure 1.1.

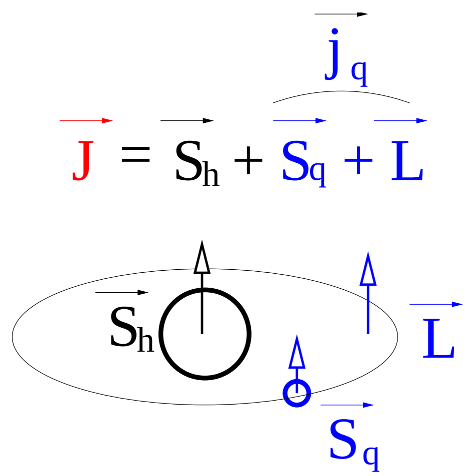

Figure 1.1: Angular momentum in the $c\bar{s}$ system

If the masses of new states are higher than the threshould which is to decay into highly allowed modes such as DK or D^*K final states with large fraction, then the natural width should be broader than the case of masses are smaller as to decay only into for suppressed modes. Otherwise, if only suppressed modes such as isospin violation decay mode with small fraction are allowed due to masses are smaller than the threshould for broader partial width decay, then the intrinsic width should be smaller.

We have investigated these states using Belle data. Our first goal here is to confirm these states and to assign spin-parity for these new states. Since the invariant mass of $D_s^+\pi^0$ in $D_{sj}(2457)$ is very close to that of $D_{sj}(2317)$ due to the mass splitting between $D_{sj}(2457)$ and $D_{sj}(2317)$ is close to the that of $D_s^*(2112)$ and D_s, we expect significant feed-across background in each signal region from the other state. A careful evaluation of these backgrounds requires a large and clean data sample. Once the existence of these state are confirmed, we determine the quantum numbers of these states, namely their spin-parity assignments. In order to determine these quantum number, we search for other

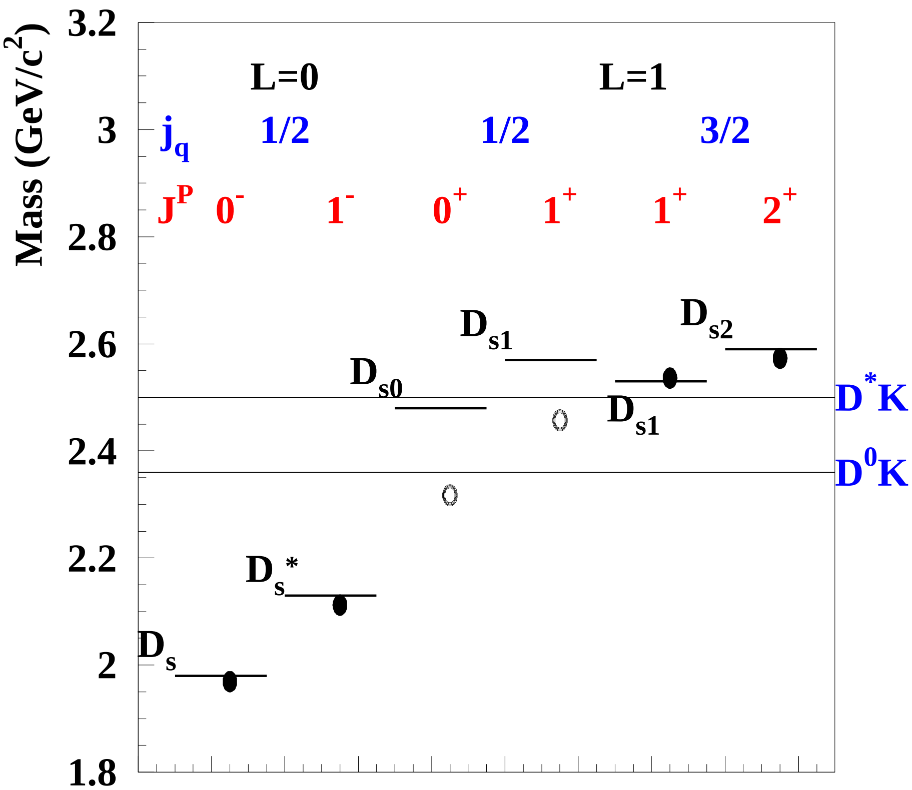

Figure 1.2: Filled circle shows previously established $c\bar{s}$ states, open circle shows newly found $c\bar{s}$ states, short bars mean the prediction of masses in potential model and long bars represent the mass threshould for expected highly allowed modes.

decay modes that are either allowed or forbidden under various spin-parity assignment.

(The second part)
Study of $|V_{ub}|$ with Using D_s Endpoint

1.2 Kobayashi Maskawa Mechanism

When it was beginning of our universe, particles and anti-particles would exist with equal ratio if they are produced from pair production. The problem is that we can see almost only particles in the present universe. As a reason why such a unbalance exist can be considered as origined in CP violation. The CP violation was found with weak interaction decay of K meson in 1964. In 1973, Kobayashi-Maskawa proved that if quark have three generations, it would contain CP violation as a natural result [1]. In 1980s, Sanda and Carter showed the decay of B meson would have large CP asymmetries [2]. Therefore, in order to get certain proof that CP violation is due to Kobayashi Maskawa mechanism, the experiment of B factory was started in 1995. If the probability amplitude of weak interaction have a complex phase, quarks and anti-quarks could behave differently. The BELLE experiment proved it with B meson decay and the test of Kobayashi Maskawa mechanism is important.

The KM matrix has the probability amplitude of weak interaction as each matrix element.

$$V_{KM} = \begin{pmatrix} V_{ud} & V_{us} & V_{ub} \\ V_{cd} & V_{cs} & V_{cb} \\ V_{td} & V_{ts} & V_{tb} \end{pmatrix}. \tag{1.1}$$

The matrix has four degrees of freedom for three generations of quarks. The four degrees consist of three degrees of rotation and one degree of complex phase as shown in following argument. In general, n $\times$ n matrix have $2n^2$ degrees of freedom. Unitarity requires to reduce n^2 degrees of freedom, relative phase of 2n quarkes reduce (2n-1) degrees of freedom, and rotation need n(n-1)/2 degrees of freedom. Then the remained degrees are calculated as following,

$$2n^2 - n^2 - (2n-1) - n(n-1)/2 = (n-1)(n-2)/2. \tag{1.2}$$

This (n-1)(n-2)/2 are degrees of freedom for complex phase. Therefore if quarks have greater than 3 generations, it mean that they have complex phases. In particular, 3 generations of quarks have n(n-1)/2 = 3 rotation parameters and (n-1)(n-2)/2 = 1 complex phase parameter. The KM matrix can be written with 4 parameters θ_1, θ_2, θ_3, δ as shown,

$$V_{KM} = \begin{pmatrix} cos\theta_1 & sin\theta_1 & 0 \\ -sin\theta_1 & cos\theta_1 & 0 \\ 0 & 0 & 1 \end{pmatrix} \begin{pmatrix} 1 & 0 & 0 \\ 0 & cos\theta_2 & sin\theta_2 \\ 0 & -sin\theta_2 & cos\theta_2 \end{pmatrix} \begin{pmatrix} 1 & 0 & 0 \\ 0 & 1 & 0 \\ 0 & 0 & e^{i\delta} \end{pmatrix} \begin{pmatrix} 1 & 0 & 0 \\ 0 & cos\theta_3 & sin\theta_3 \\ 0 & -sin\theta_3 & cos\theta_3 \end{pmatrix} \tag{1.3}$$

$$= \begin{pmatrix} cos\theta_1 & sin\theta_1 cos\theta_3 & sin\theta_1 sin\theta_3 \\ -sin\theta_1 cos\theta_2 & cos\theta_1 cos\theta_2 cos\theta_3 - sin\theta_2 sin\theta_3 e^{i\delta} & cos\theta_1 cos\theta_2 sin\theta_3 + sin\theta_2 cos\theta_3 e^{i\delta} \\ sin\theta_1 sin\theta_2 & -cos\theta_1 sin\theta_2 cos\theta_3 - cos\theta_2 sin\theta_3 e^{i\delta} & -cos\theta_1 sin\theta_2 sin\theta_3 + cos\theta_2 cos\theta_3 e^{i\delta} \end{pmatrix}. \tag{1.4}$$

In order to compare each matrix elements easily, we use the replacement of the 4 parameters θ_1, θ_2, θ_3, δ with λ, A, ρ, η. Then λ and A are defined by $\lambda \equiv |V_{us}| \sim 0.22$ and by $A\lambda^2 \equiv |V_{cb}| \sim 0.04$ (A is of order unity). If only second order of λ is taken into account, the V_{KM} is described as

$$V_{KM} = \begin{pmatrix} 1-\lambda^2/2 & \lambda & 0 \\ -\lambda & 1-\lambda^2/2 & A\lambda^2 \\ 0 & -A\lambda^2 & 1 \end{pmatrix} + O(\lambda^3). \tag{1.5}$$

If $|V_{ub}|$ and $|V_{td}|$ are replaced with arbitrary third order of λ, they can be written as $|V_{ub}| = A\lambda^3(\rho - i\eta)$ and as $|V_{td}| = A\lambda^3(\alpha - i\beta)$, then the V_{KM} is described as

$$V_{KM} = \begin{pmatrix} 1-\lambda^2/2 & \lambda & A\lambda^3(\rho - i\eta) \\ -\lambda & 1-\lambda^2/2 & A\lambda^2 \\ A\lambda^3(\alpha - i\beta) & -A\lambda^2 & 1 \end{pmatrix} + O(\lambda^4), \tag{1.6}$$

where, unitrarity ($V_{KM}V_{KM}^\dagger = I$) requires $\alpha = 1 - \rho$, and $\beta = \eta$. Eventually, the KM matrix to the third order in λ becomes

$$V_{KM} = \begin{pmatrix} 1-\lambda^2/2 & \lambda & A\lambda^3(\rho - i\eta) \\ -\lambda & 1-\lambda^2/2 & A\lambda^2 \\ A\lambda^3(1 - \rho - i\eta) & -A\lambda^2 & 1 \end{pmatrix} + O(\lambda^4). \tag{1.7}$$

(Wolfenstein expression [5])

In order to prove CP violation, whether KM matrix have irreducible complex phase or not is investigated. Then it was used that V_{KM} must satisfy unitarity,

$$V_{KM}^{\dagger} V_{KM} = I, \tag{1.8}$$

the orthogonality of the d-column and the b-column leads

$$V_{ud}V_{ub}^* + V_{cd}V_{cb}^* + V_{td}V_{tb}^* = 0. \tag{1.9}$$

The three component of above equation can be written in complex plane, and they form a triangle. If it is drawn in (ρ, η) plane, the unitarity triangle becomes as shown below. Then, three angle ϕ_1, ϕ_2, and ϕ_3 are defined.

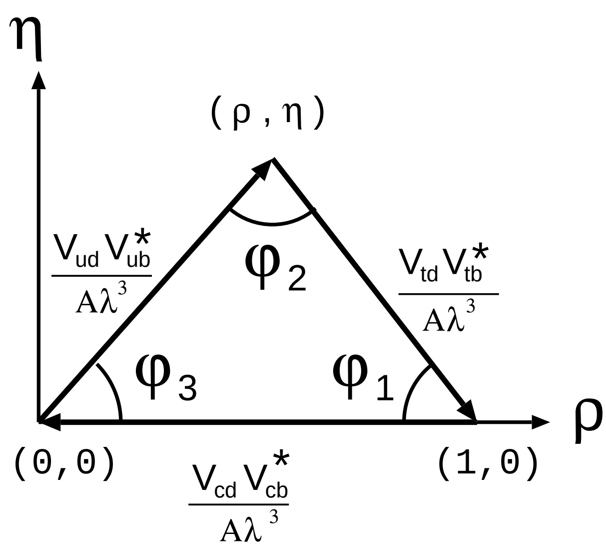

If the angle ϕ_1 or ϕ_3 is not zero, KM matrix should have complex phase. Already, BaBar collaboration and Belle collaboration showed that $sin2\phi_1$ is not zero [3] [4]. It means CP violation, but whether Kobayashi-Maskawa theory is right or not depends on whether unitarity triangle is closed or not. Parameter λ and A are well known and $|V_{ud}|$ can be written with λ, therefore the measurement of $|V_{ub}|$ gives one side of the triangle which is opposite to ϕ_1. Thus, measurement of $|V_{ub}|$ is important because this measurement make it possible to confirm KM theory is correct or not.

Chapter 2

BELLE experiment

For the purpose of studying CP violation in B meson system, BELLE experiment was started. In order to prove the difference between particle and anti-particle except for the combination both the sign of the charge and parity, large amount of $B\overline{B}$ pair is produced with e^+e^- collider. Then, e^+ and e^- are collided on $\Upsilon(4S)$ resonance energy which is 10.58 GeV in the center of mass frame, and more than 96% of $\Upsilon(4S)$ decay into $B\overline{B}$ pair. We accumulated 350 million $B\overline{B}$ pair data by February, 2005. High statistics of $B\overline{B}$ data enables us to measure large CP asymmetry and test of Kobayashi Maskawa theory.

2.1 KEKB accelerator

KEKB accelerator is using storage ring of 8.0 GeV electron and 3.5 GeV positron to make them collide and produce large amount of $B\overline{B}$ pair. Each ring have 5000 bunches which were stored in 3 km rings, and they collide in each 2 ns with the angle of 11 mrad. High energy ring (HER) have 1.4×10^{10} electron per bunch and low energy ring (LER) have 3.3×10^{10} positron with design beam current 1.1 A and 2.6 A for HER and LER. They have asymmetry energy because $B\overline{B}$ were required to boost in laboratory frame in order to get the large difference of decay length between B and $\overline{B}$ for studying CP asymmetry. Boost factor can be calculated as

$$\beta\gamma = (E_{e^-} - E_{e^+})/\sqrt{s} = (\text{ 8.0 - 3.5 })/10.58 = 0.425$$

The general view of KEKB accelerator is described in Figure 2.1.

2.2 BELLE detector

Belle detector consist of some devices such as sub-detectors, beam-pipe, solenoid magnet and so on. In order to detect various particles, each sub-detector were designed and have been developed continuously. Sub-detectors without K_L/μ detector were located inside of the super-conducting solenoid of 1.5T magnet field. Feature and performance of each devices are as follows.

2.2.1 Silicon Vertex Detector (SVD)

When CP violation is proved with $B\overline{B}$ mixing, the flight length difference of $B\overline{B}$ pair must be measured. Silicon Vertex Detector (SVD) has four layers of 300 μm thick Double Sided Silicon Detector (DSSD), and it is located just around beam pipe with the 3.3$\sim$ 5.8cm radius and 22$\sim$34cm length. The required resolution of vertex difference is more than 100 μm on the beam axis.

2.2.2 Central Drift Chamber (CDC)

Drift chamber was located around SVD to measure tracks, momentum and dE/dx of charged particles. Central Drift Chamber(CDC) is filled with low material gas mixture(50% He and 50% C_2H_6) which can ionize charged particles. CDC is small cell chamber that have 50 anode wires and 3 cathode strip layers, then the 50 anode wire were divided into 32 axial and 18 stereo wire to reconstruct 3-dimensional track. Momentum can be measured from curvature radius of track in the 1.5T magnet field. Measurement of specific ionization (dE/dx) make it possible to identify particles. This chamber covers 77mm to 880mm in radius and 17° to 150° in polar angle, and have 8,400 readout channels for anode and 1,792 channels for cathode.

The spatial resolution are 130 μm in the transverse plane of the beam axis, and less than 2mm in the beam axis, which means transverse momentum resolution σ/p_t is $\sqrt{(}(0.19p_t)^2+0.34^2)\%$ with GeV/c. The resolution of dE/dx is 6.9%.

2.2.3 Aerogel Cherenkov Counter (ACC)

The role of Aerogel Cherenkov Counter (ACC) is particle identification of kaon or pion in the high momentum region that is greater than 1.2 GeV/c. ACC detect pion with Cherenkov light which is emitted in Aerogel whose reflective index is 1.01 $\sim$ 1.03. Cherenkov light can be measured when particle velocity exceeds light of velocity in the material, then the reflective index was chosen as kaon don't emit Cherenkov light. Aerogel block is 12 $\times$ 12 $\times$ 12 cm^3 typically, and equip with fine-mesh photo multiplier tubes (FMPMT). There are 960 counter in barrel region and 228 counter are in endcap region.

2.2.4 Time Of Flight counter (TOF)

For the aim of measuring velocity of particles, Time Of Flight counter (TOF) is installed. This counter can distinguish between kaon or pion in the momentum region below about 1.2 GeV/c. For the 1.2 m flight pass, the required resolution is 100 ps. The length of this counter is 3 m, and 128 counters was located. Each pair of two TOF have trigger Sintilation Counter (TSC).

K/π Separation We can separate kaon and pion with combining informations of likelihood from ACC, TOF and CDC in each momentum region. The typical separation distribution with using the decay mode $D^{*+} \rightarrow D^0\pi^+$ and $D^0 \rightarrow K^-\pi^+$ where the kaon and pion tracks in the two-body decay kinematic region are selected by requiring 2.40 GeV/c $< P^* <$ 2.85 GeV/c are shown in figure 2.10.

2.2.5 Electromagnetic CaLorimeter (ECL)

In order to measure energy deposit of photon or electron with scintillation light, CsI crystal was located. The number of crystal are 8,736 and typically they are 5.5 $\times$ 5.5 $\times$ 30 cm^3 that is 16 radiation length. Shower of electromagnetic interaction was measured with 3 $\times$ 3 or 5 $\times$ 5 crystal set, and the ratio of energy in this two region is used to know shower shape. This calorimeter covers with the poler angle of 12.01° to 31.36° and 32.2° to 128.7° for barrel and endcap region.

The resolution with 5 $\times$ 5 crystal is $\sigma_E/E = 0.066$ %/E $\oplus$ 0.81 $\%/E^{1/4} \oplus 1.34$ % and the position resolution is $\sigma_{pos} = 0.5\mathrm{cm}/\sqrt{E}$ with GeV/c.

Electron identification Electrons are identified with the ratio of energy to momentum (E/p). It is close to 1 for electrons. And, we use the ratio of enrgy sum in 3 $\times$ 3 crystal set to enrgy sum in 5 $\times$ 5 crystal set (E9/E25). This use the difference between electromagnetic shower shape and hadronic shower shape. In addition to E/p and E9/E25, we use matching of an extrapolated track position and a cluster position at ECL, dE/dx in CDC, light yeild in ACC, and time of flight in TOF for electron identification. We calculate the likelihood value with pobability density function of these values in Monte Carlo.

2.2.6 Extreme Forward Calorimeter (EFC)

EFC is the detector for electron or photon that was located in extreme forward and backward which covers around the beam axis. EFC was made from 2cm $\times 2cm$ BGO ($Bi_4Ge_3O_{12}$) crystals because EFC was exposed in high radiation of photons from synchrotoron radiation or spent electron ($\sim$ 5 MRad per year). Typical cross-section is $12X_0$ for forward and $10.5X_0$ is backward. They cover $6.4^\circ \sim 11.5^\circ$ or $163.3^\circ \sim 171.2^\circ$ for forward or backward.

2.2.7 $\mathbf{K}_L^0 \cdot \mu$ detector (KLM)

In order to detect muon or K_L, KLM detector was instolled. The KLM consist of Resistive Plate Counter (RPC) and 4.7cm-thick iron that have 14$\sim$15 layers. RPC is one of spark chamber that is filled with gas mixture(30% Ar, 62% HFC134a, 8% C_3H_{10}). Then the charged particle are measured in RPC and the particle that penetrated through irons are identified as muon. The secondary particles of interaction between K_L and iron are measured as direction of K_L cluster. Simoltaniously the iron plays the role of return yoke. KLM detector covers $20^\circ \sim 155^\circ$ with polar angle.

Muon identification We identfy muons with charged particles which penetrated through iron layers in KLM. Then, charged tracks which are measured in SVD and CDC are extrapolated into KLM and they are assosiated with KLM hits. We use two quantities for muon identification; one is ΔR which is defined as the difference between expected range of track and measured range of track in KLM. Another is χ_r^2 which is normalized transverce deviation of all hits assosiated with the track. We use probability density function of these two value with tracks of muons, pions and kaons in Monte Carlo to calculate the likelihood.

Better Precision Inner trackers The BELLE detector is making improvement continuously. In 2003 summer, we replaced inner more part of CDC with two layers of small cell chamber (sCDC) and SVD are replaced from three layer with four layer (SVD2), then inner most layer of SVD2 is now located closer to the interaction point with a smaller radius beryllium beam pipe. We improved the detector performance as to be more precise decay vertex for B, better reconstraction of charged track for low momentum and less deadtime in DAQ with newly developed electronics.

2.3 Trigger

The design values of trigger and data acquision is 200Hz for typical trigger, 500Hz for maximum trigger, 30kB/event for data size, and 15 MB/s for data transfer speed.

The trigger consist of sub-detector trigger and central trigger which is called Global Decision Logic (GDL). The sub-detector trigger was combined into GDL. Then two independent trigger exist, one is track trigger and another is energy trigger. The track trigger consist of CDC r-ϕ track, TOF trigger, and number of isolated ECL cluster trigger. The energy trigger is based on ECL energy sum. The basic hadronic skim is a logical OR of next 4 qualification: tight 2 track trigger, loose 3 track trigger, number of isolated cluster is greater than 4, and energy sum is larger than 1 GeV. The exact definition and condition of triggers are in the BELLE note [15]. The efficiency of each trigger are greater than 97%, therefore the final trigger efficiency is greater then 99.9%.

The timing signal is decided from TOF or ECL trigger that are adjusted to 1.85 μs from the event crossing, and after timing trigger 0.35 μs is used for GDL processing, totally trigger timing is adjusted to 2.2 μs from the event crossing.

After the software trigger which have almost 100% efficiency for hadronic event, each event is classified into some categories. In the endpoint analysis, we used hadron like events, which called "HadronBJ" that is categolized as standerd hadronic event. The conditions of "HadronBJ" are as following,

- Number of 'good' track multiplicity is greater than 3.
  ('good' means $p_t > 0.1$GeV, $|dr| < 2.0$cm, and $|dz| < 4.0$cm)
- Visible energy of tracks and photons(E_{vis}), is greater than 20 % of $\sqrt{s}$
- Momentum balance of z compornet; $|\Sigma p_z| \leq 0.5\sqrt{s}$
- Primary event vertex is around interraction point; $|r| < 1.5$cm and $|z| < 3.5$cm
- Sum of energy deposited in ECL; $0.18\text{GeV} < E_{sum} < 0.8\text{GeV}$
- Number of ECL clusters in $-0.7 < \cos\theta < 0.9$ is greater than 2
- Heavy jet mass; $M_{jet} > 0.25E_{vis}$ or $M_{jet} > 1.8$GeV
  (Heavy jet mass means essencially τ mass)
- average of ECL cluster energy is smaller than 1GeV

2.4 Data AcQuisition (DAQ)

The read out from sub-detector and trigger are running in parallel. The signal from all sub-detectors except for the SVD are digitized by a unified readout system based on Q-to-T convertion using FASTBUS controller and transfered to the event building fram through a 100base-TX network. The data from SVD are processed by a PC-based readout system and sent to the event building farm directly via the network. The event building farm is based on switchless event building technology and consists of three layers of PC servers. The first layer servers recieve the data from the VME readout system and perform partial event building for connected subdetectors. Software trigger processing is also performed and a veto signal can be sent to the second layer servers to reject the event data from other layer servers. The final event building is done on the layer three server and the event is sent to the tape recording system and also to the real-time reconstruction farm.

2.5 Computing system

BELLE accumulate more than 1 million $B\overline{B}$ pairs in one good day. This correspond to about 1.2TB of raw data per day. The amount of raw and processed data accumulated so far exceed 1.4PB. BELLE's computing model has been traditional one and has been very successful. Raw data are transferred from Tsukuba experimental hall to the computing center via optical fiber where they are directly written to DTF2 tapes. Recently, a new path has been added to an online PC farm where we run the first DST production and write output data onto a new hierarchical strage management system consisting of IDE raid disks and tape library. The tape library can hold 1.2PB of data on 500GB tapes. The final data processing is done on PC farms. The output data files for physics analysis are written to IDE raid disks and final user physics analysis job are also run on PC farms. The network for data transfer now extends to collaboration universities using dedicated 1 Gbps lines.

2.6 Software tool

The overview of the data analysis and Monte Carlo simulation is shown on 2.19. The raw data which are acquited with BELLE detector are processed by reconstruction tools such as tracking of charged particle, measuring of energy and particle identification. utputs of reconstruction tools is called Data Summary Tape (DST) and it is converted to more compact data set that is called Mini Data Summary Tape (MDST) for user analysis. When we simulate with BELLE detector, we use QQ generator [11] or EvtGen generator as event generator which is originally developed by CLEO collaboration and modified for BELLE detector [12], then we use two detector simulation; one is full detector simulator (GSIM) that generates detector response in the same form as real data.

Event generator Event generator simulates physical process of decay chains. Then, we use each decay mode and branching fraction in the result of CLEO group which are modified for BELLE detector. Decay modes and branching fractions are recorded in a decay table, and user can controll them by chainging the decay table. The outputs of decay information with QQ are stred in HEPEVT table [13]. There are two main states as initial state; one is $\Upsilon(4S)$ and another is $q\overline{q}$ (continuum prosess). Most of $\Upsilon(4S)$ decay into $B\overline{B}$ pair, and on the energy of $\Upsilon(4S)$ resonance, the main background is $e^+e^- \to q\overline{q}$ event ($\sigma(e^+e^- \to q\overline{q}) \simeq 3\sigma(e^+e^- \to \Upsilon(4S))$).

Geant (full) detector SIMulator (GSIM) The full detector simulator (GSIM) is based on GEANT [14] which is developed in CERN for the simulation of reaction between particles and materials in the detector. The data from HEPEVT table are inputed into GSIM, and GSIM traces the behavior of each particles in the detector and generates detector responce which is the same form with real data output. GSIM takes much time (~ 30 sec/event) because of tracing each particle one by one for the precise reactions with materials.

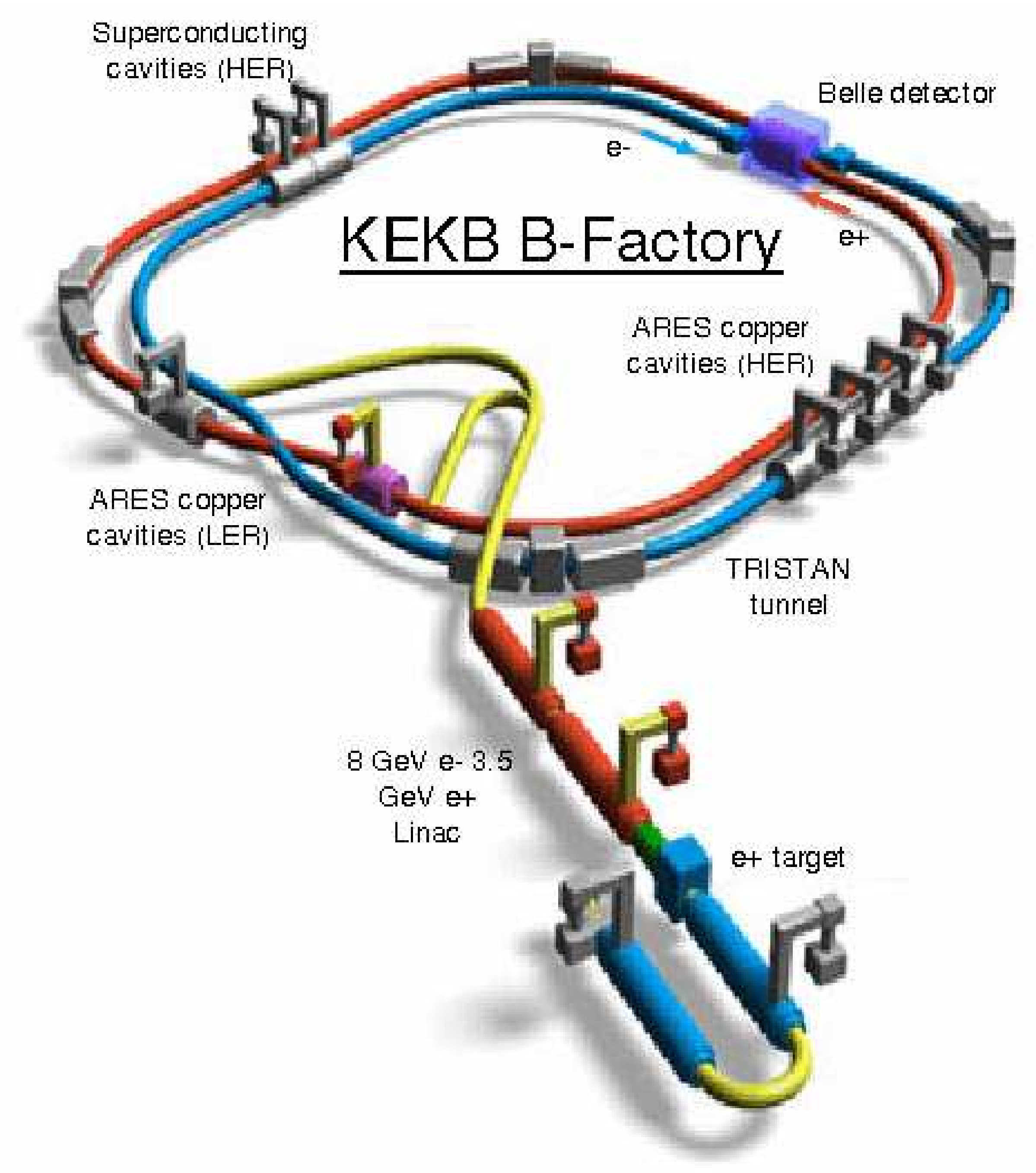

Figure 2.1: KEKB accelerator

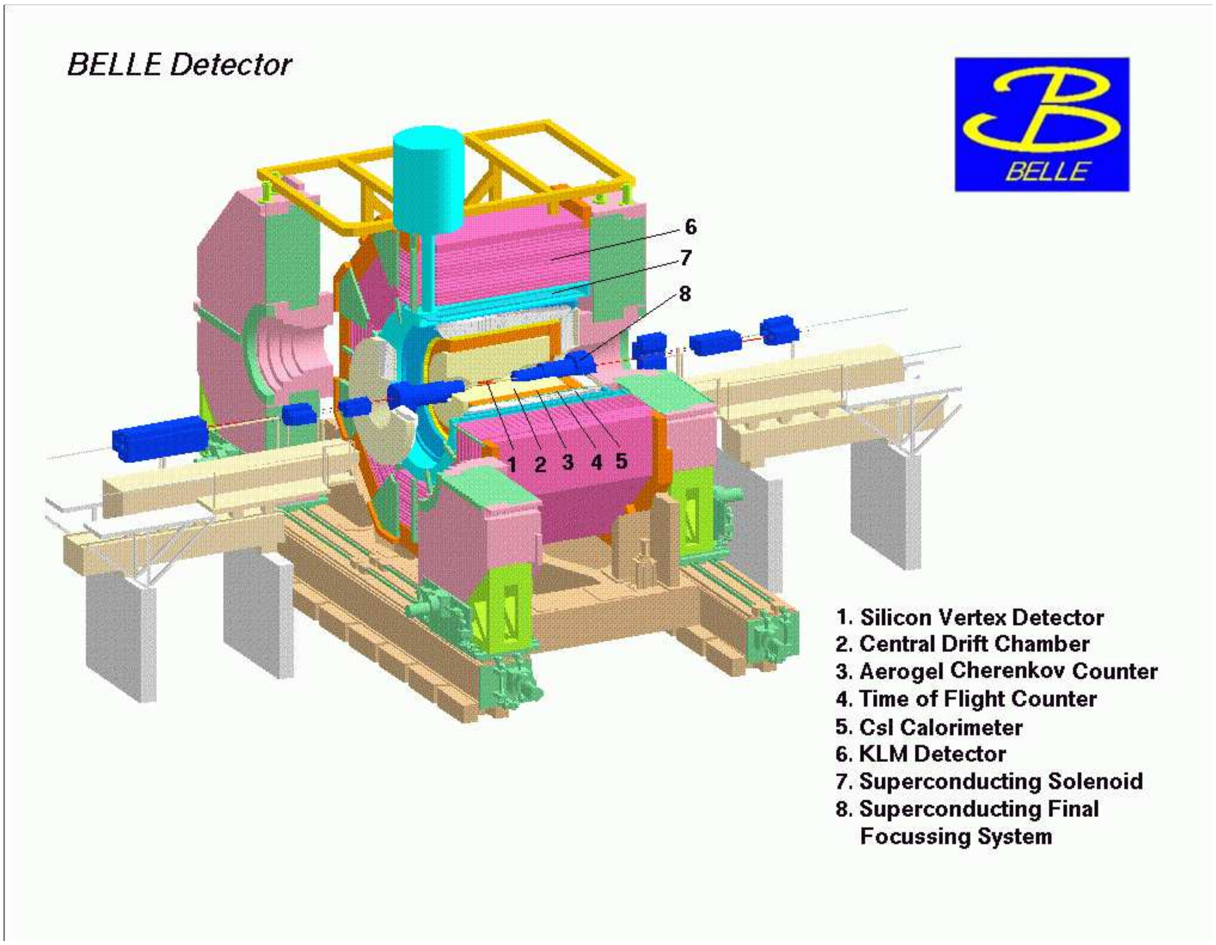

Figure 2.2: BELLE detector

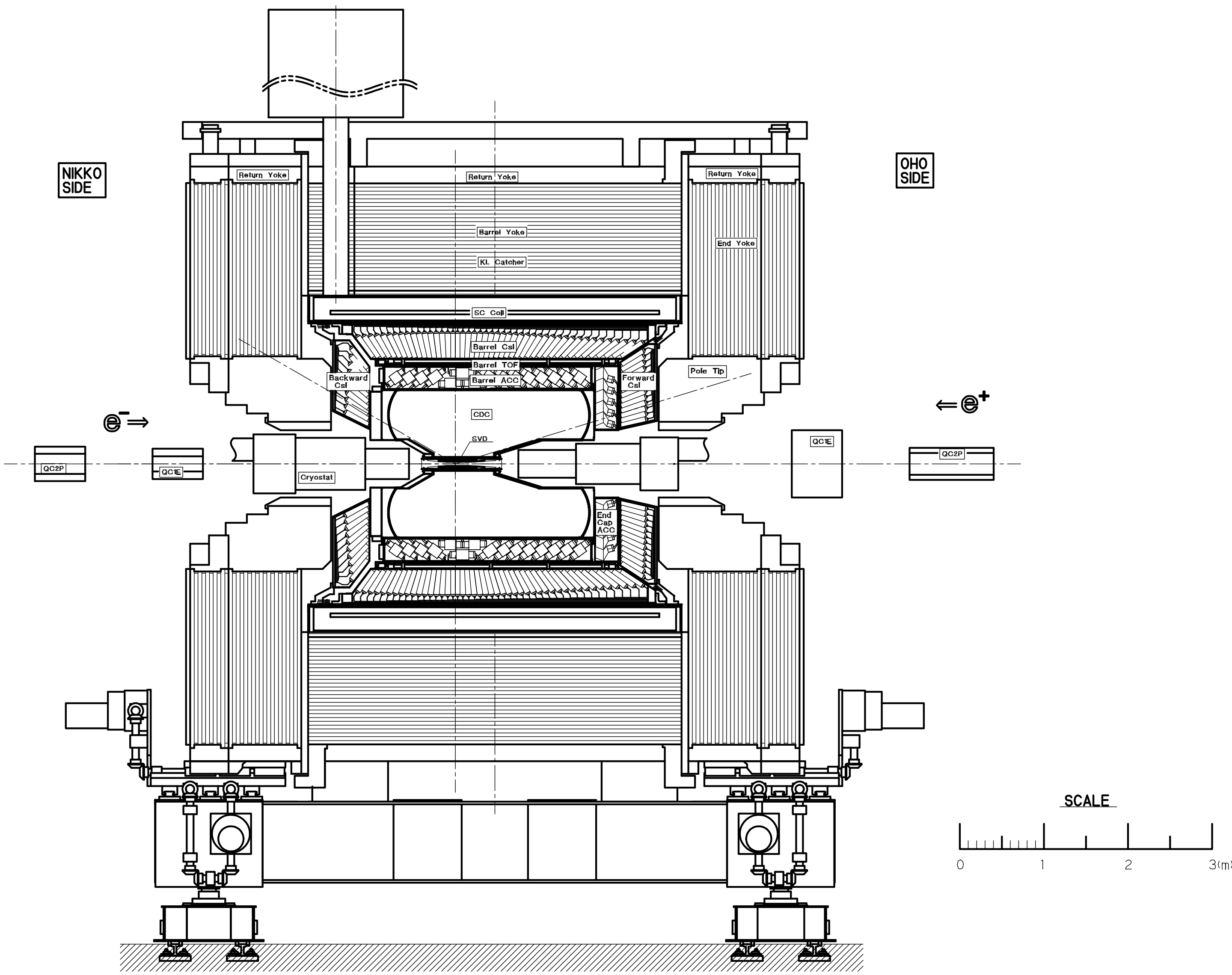

Figure 2.3: BELLE detector side view

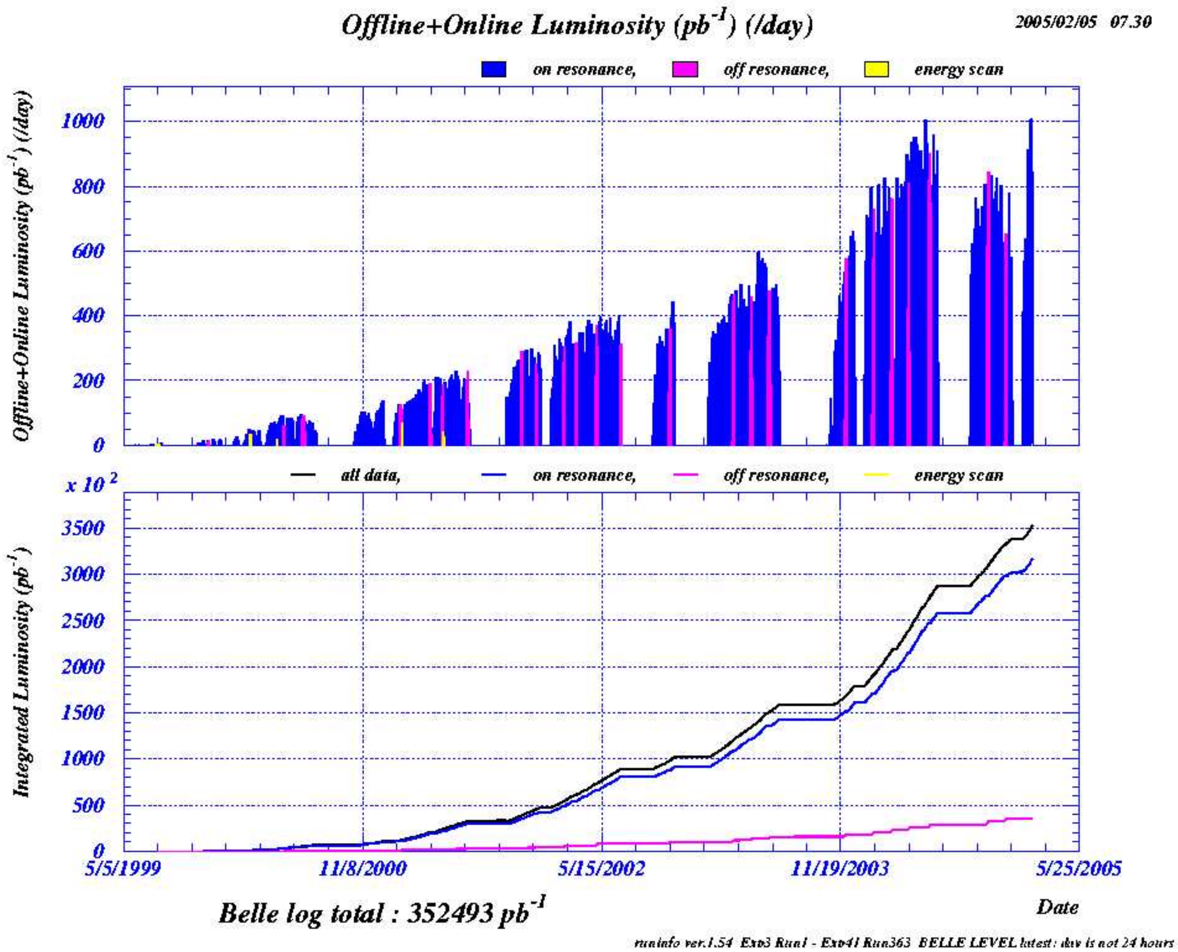

Figure 2.4: Integrated luminosity

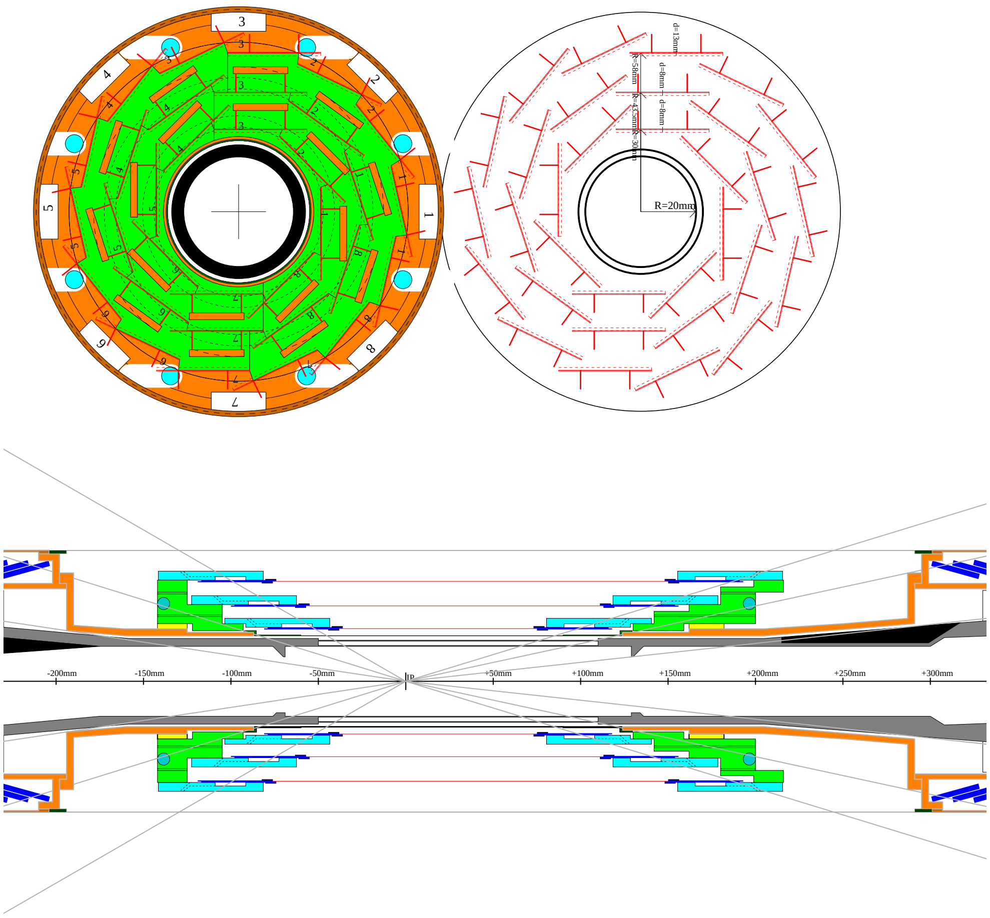

Figure 2.5: Silicon Vertex Detector (SVD)

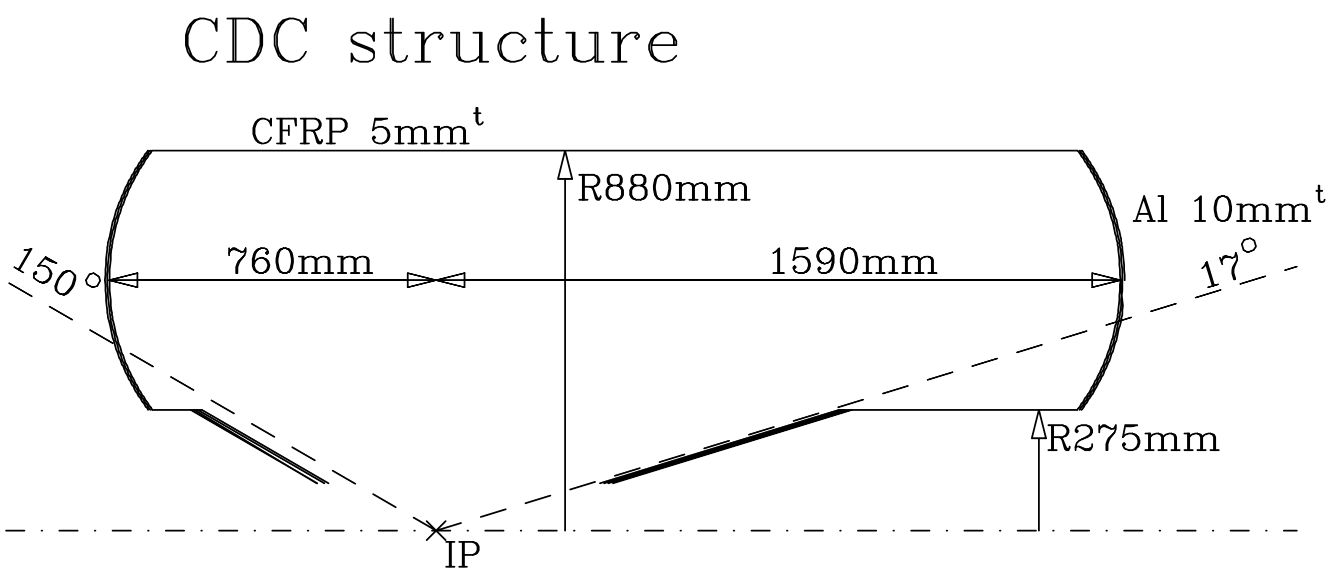

Figure 2.6: Central Drift Chamber (CDC)

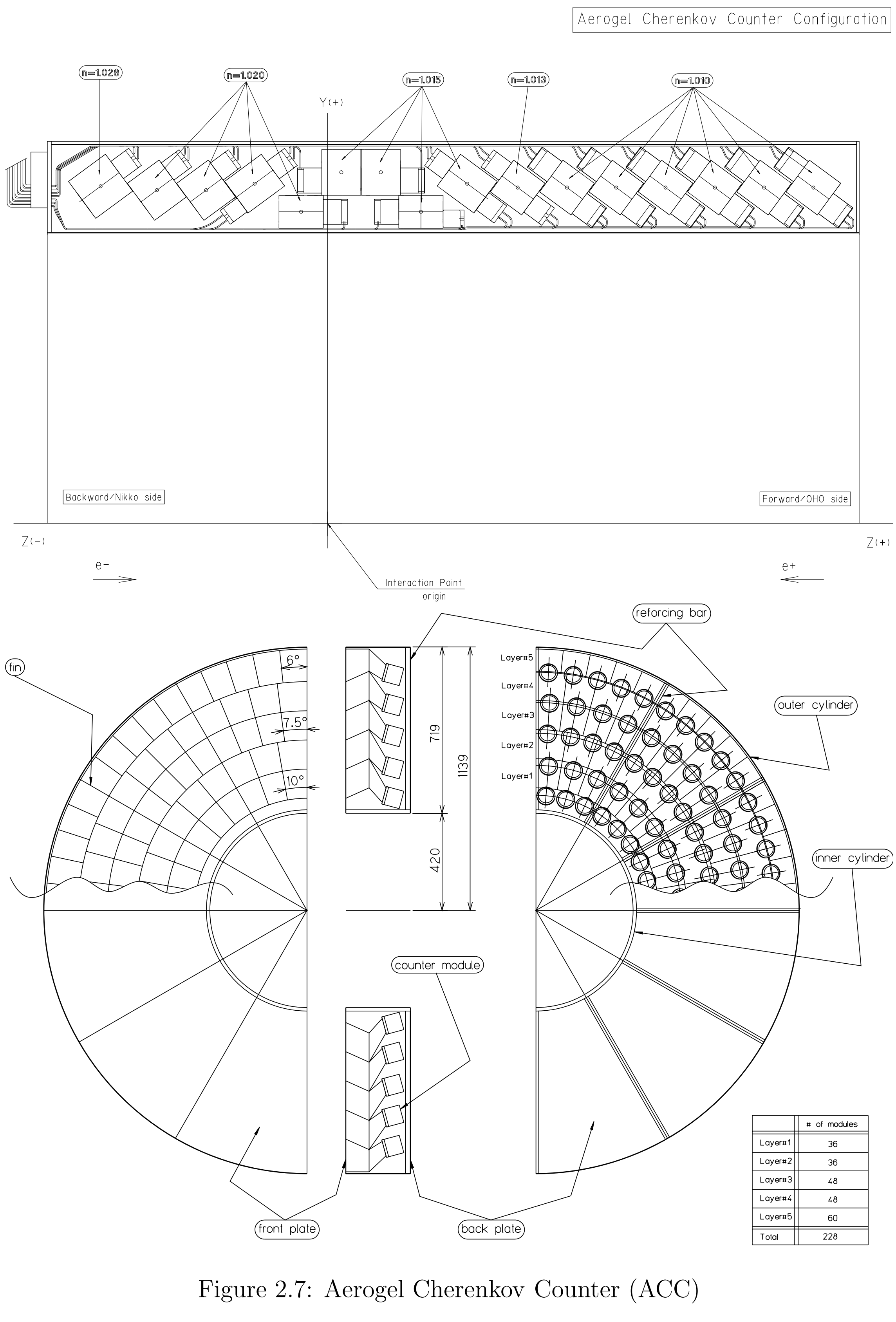

Figure 2.7: Aerogel Cherenkov Counter (ACC)

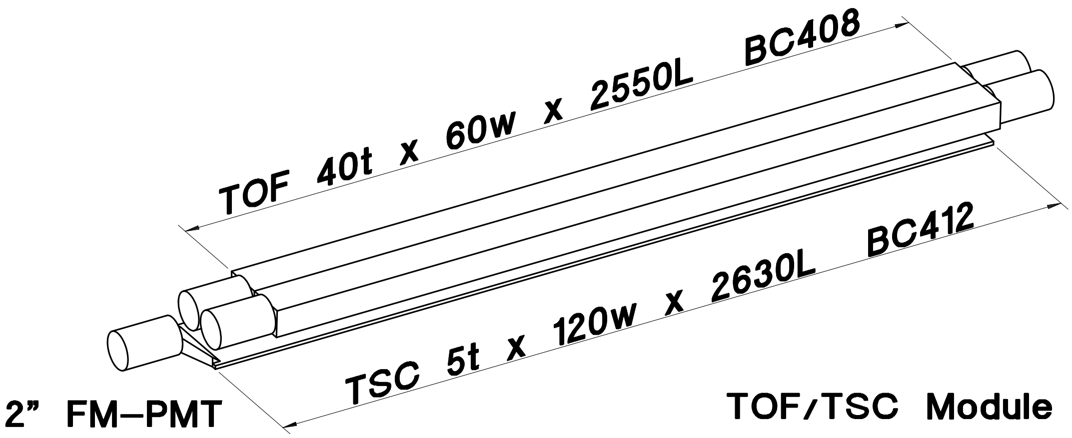

Figure 2.8: Time Of Flight counter (TOF)

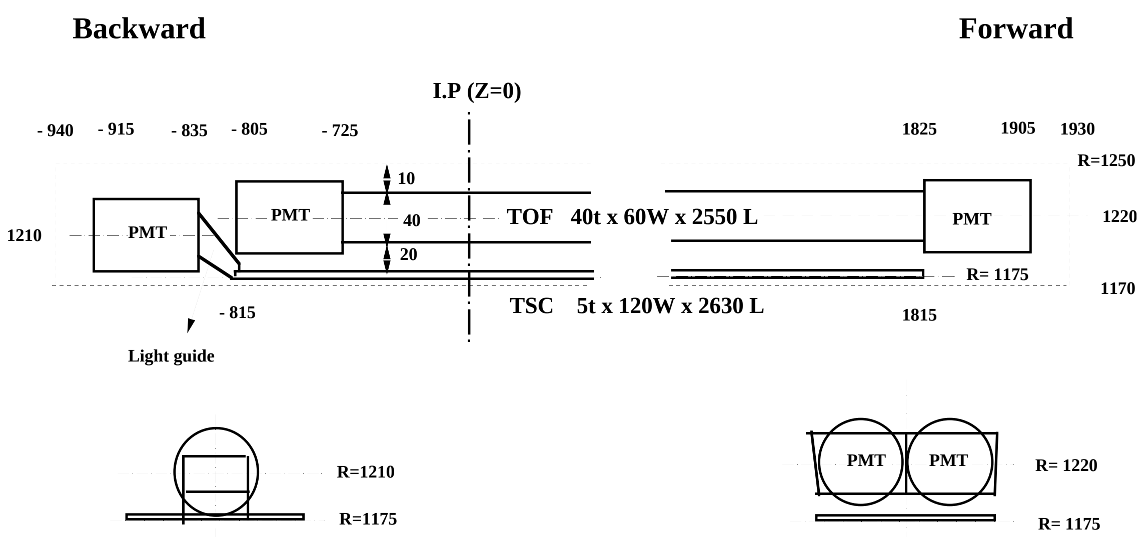

Figure 2.9: Trigger Scintillation Counter (TSC)

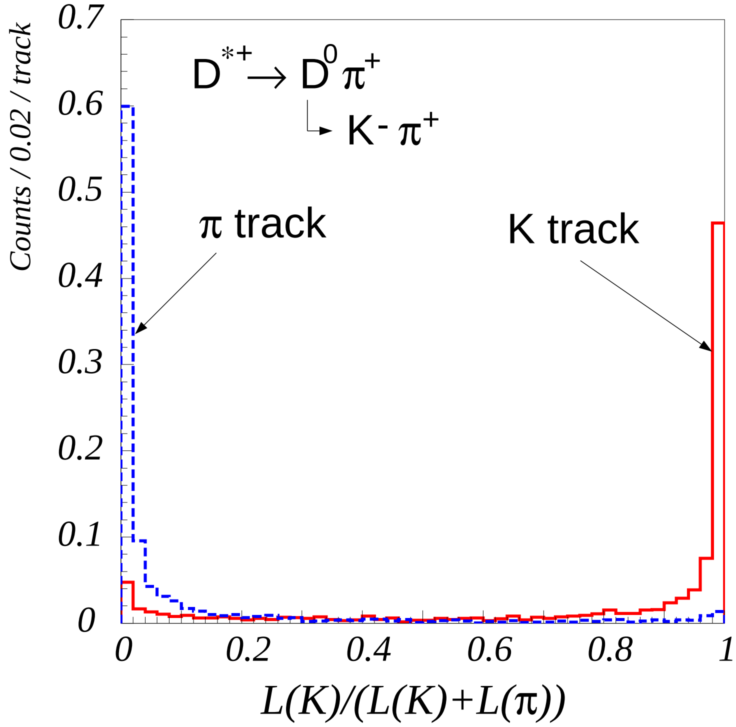

Figure 2.10: Likelihood ratio for K/π separation

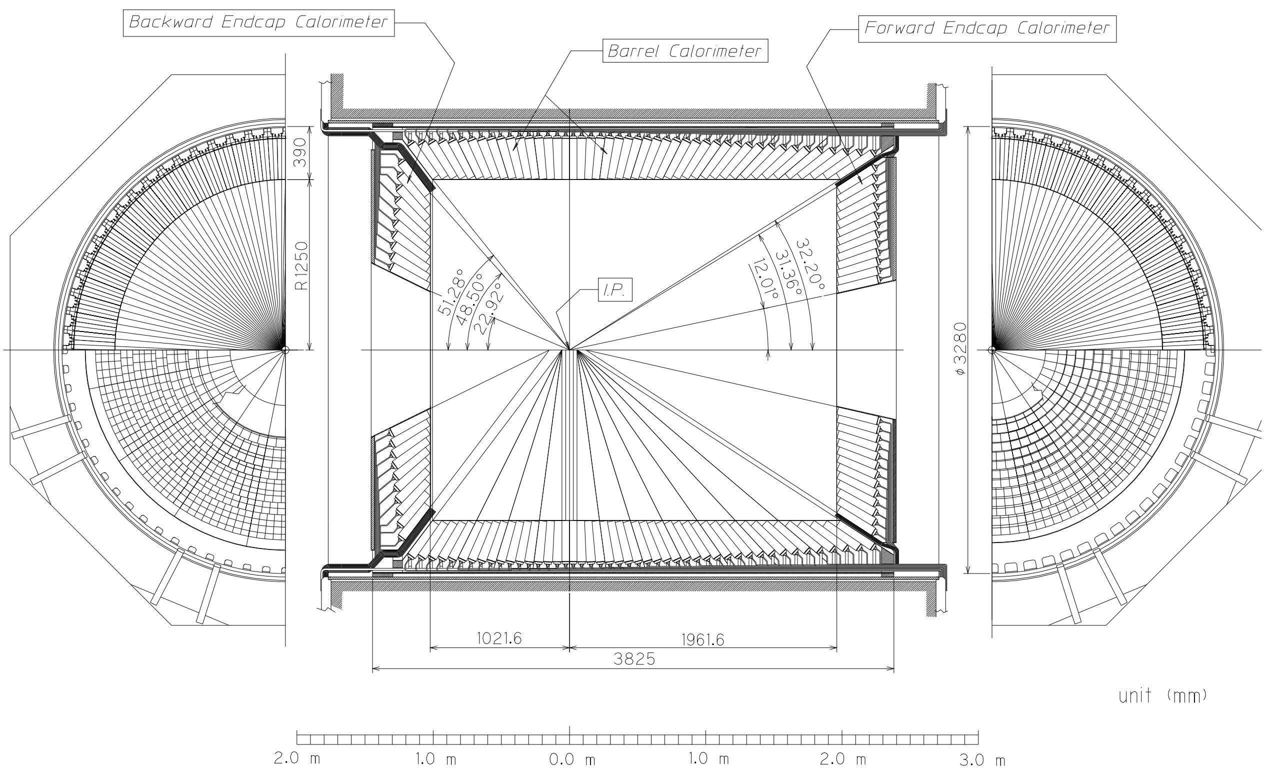

Figure 2.11: Electromagnetic CaLorimeter (ECL)

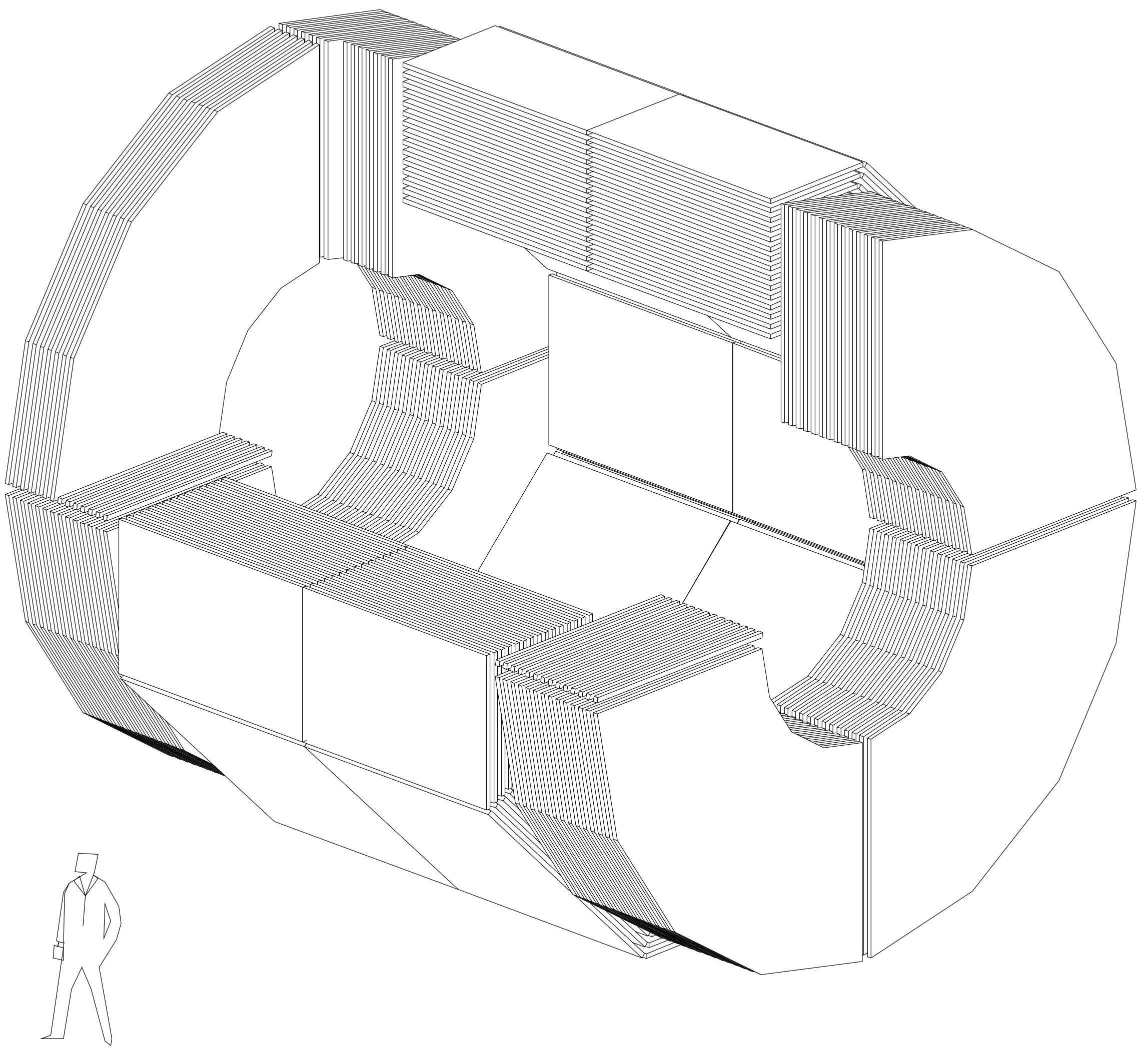

Figure 2.12: K_L^0 · μ detector(KLM)

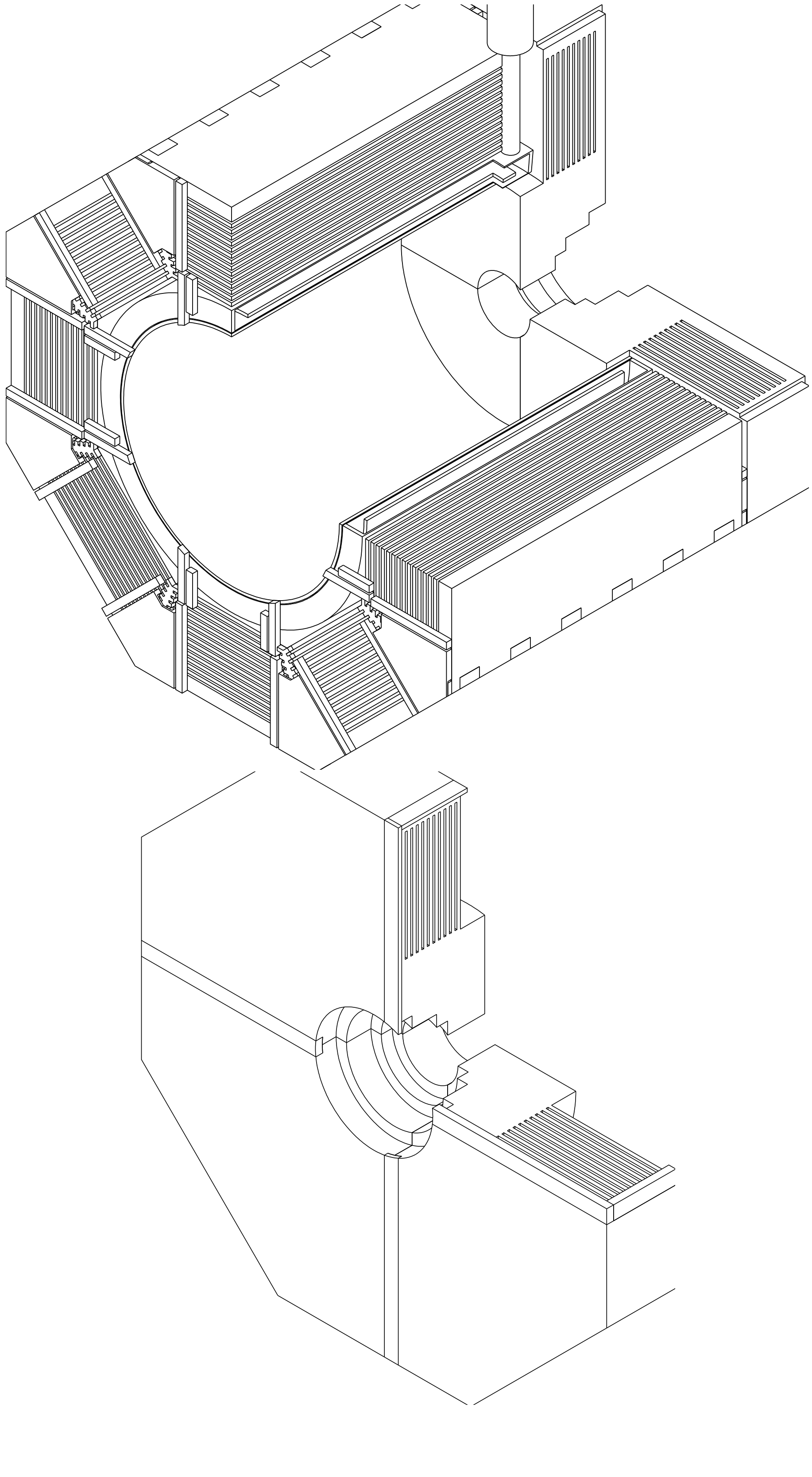

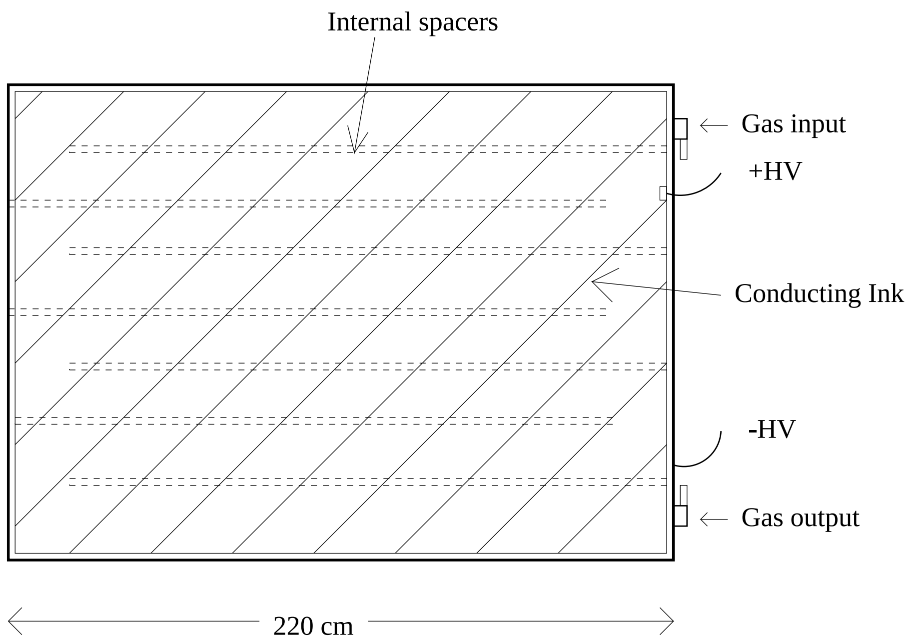

Figure 2.13: Barrel RPC

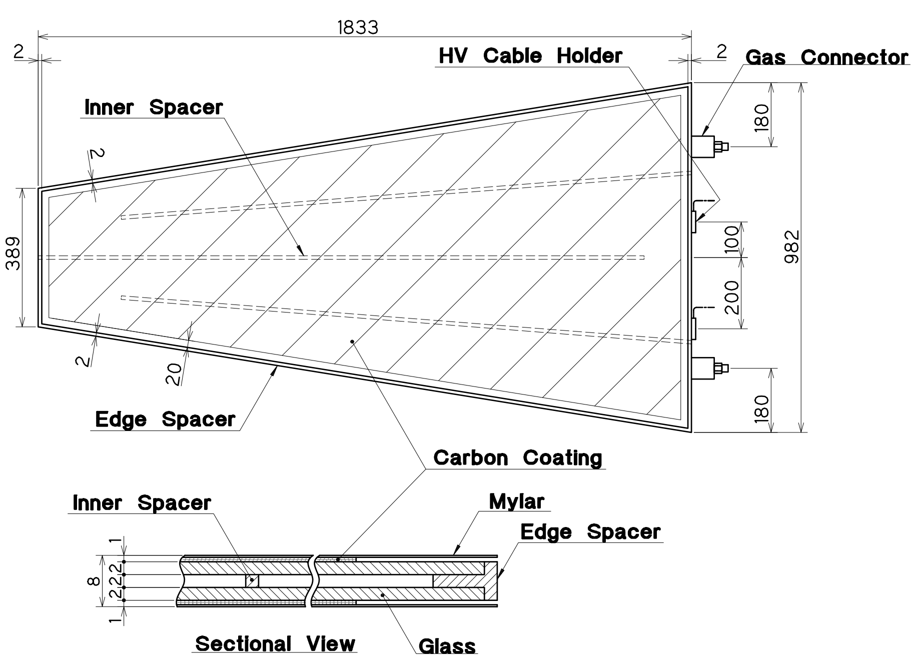

Figure 2.14: Endcap RPC

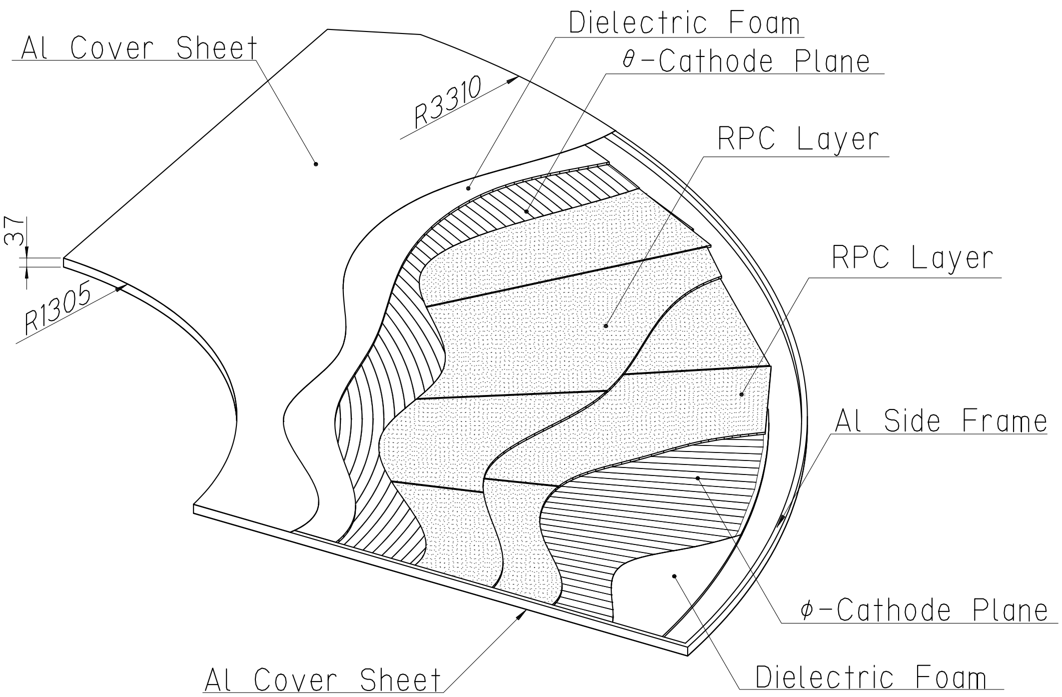

Figure 2.15: Layer structure (KLM)

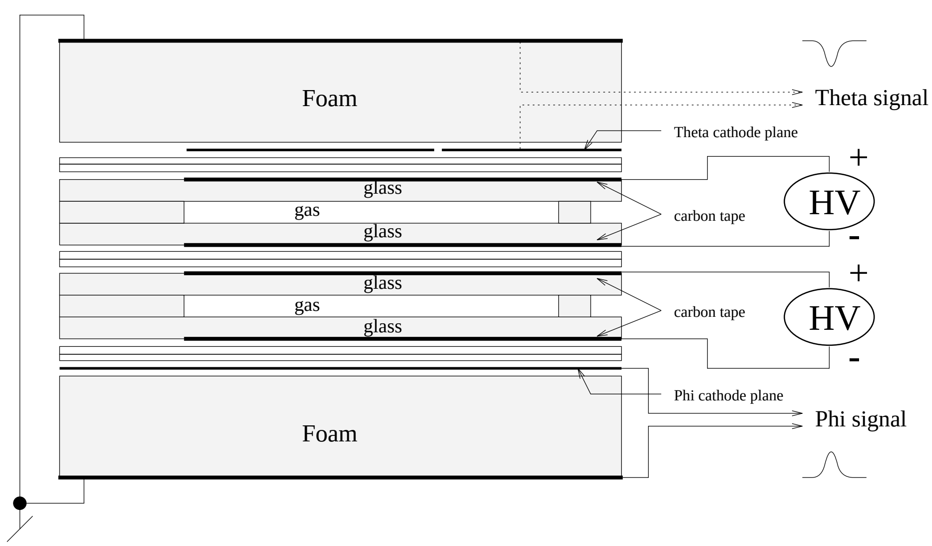

Figure 2.16: RPC super-layer

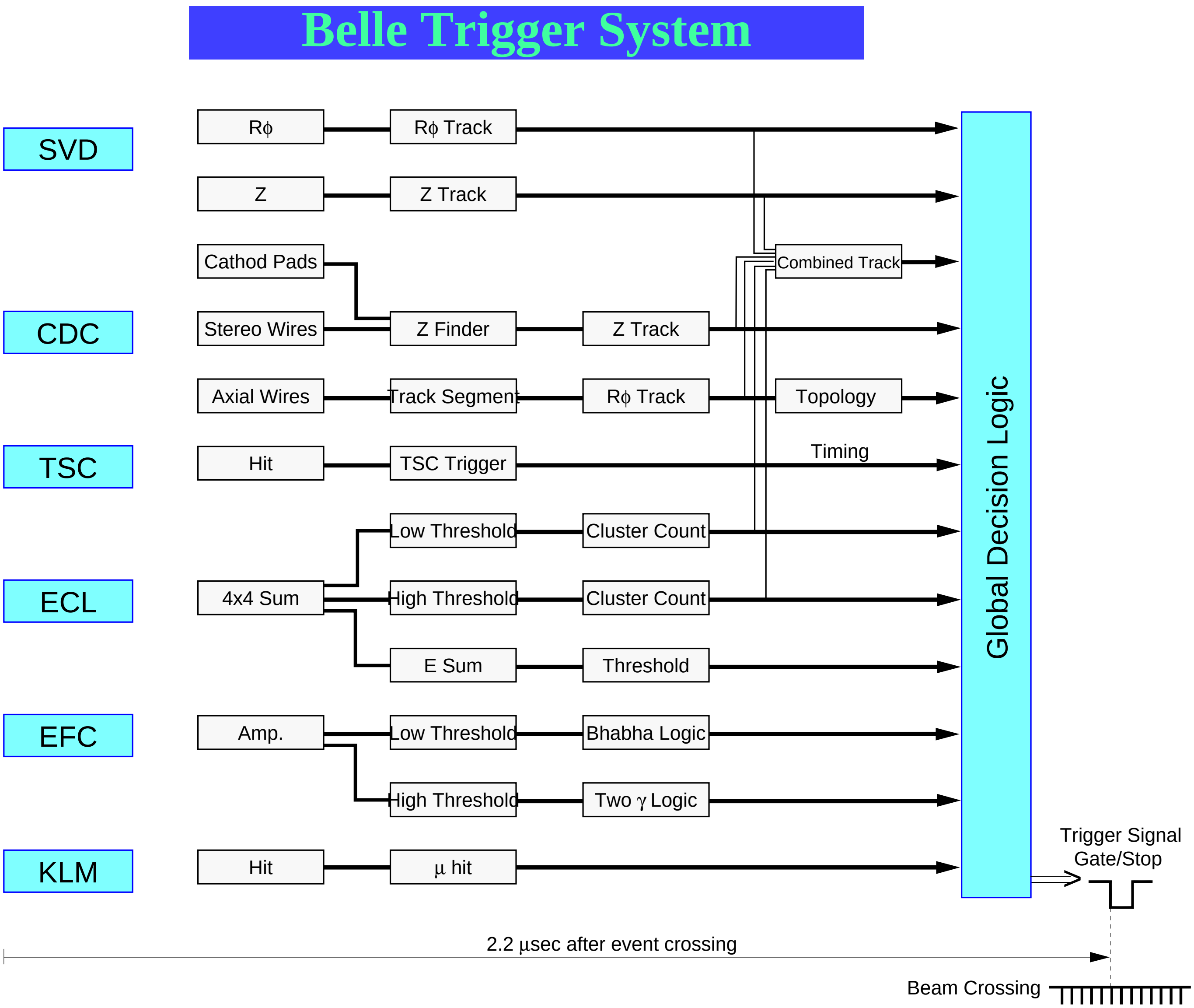

Figure 2.17: Trigger system

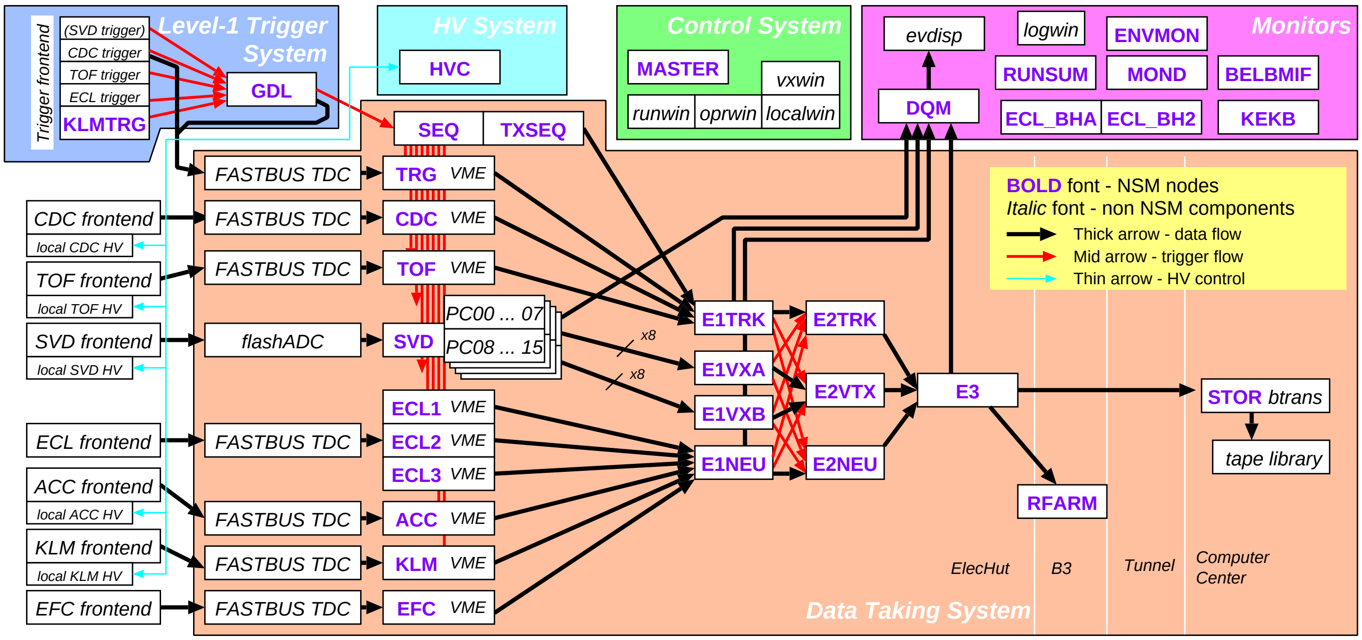

Figure 2.18: Daq system

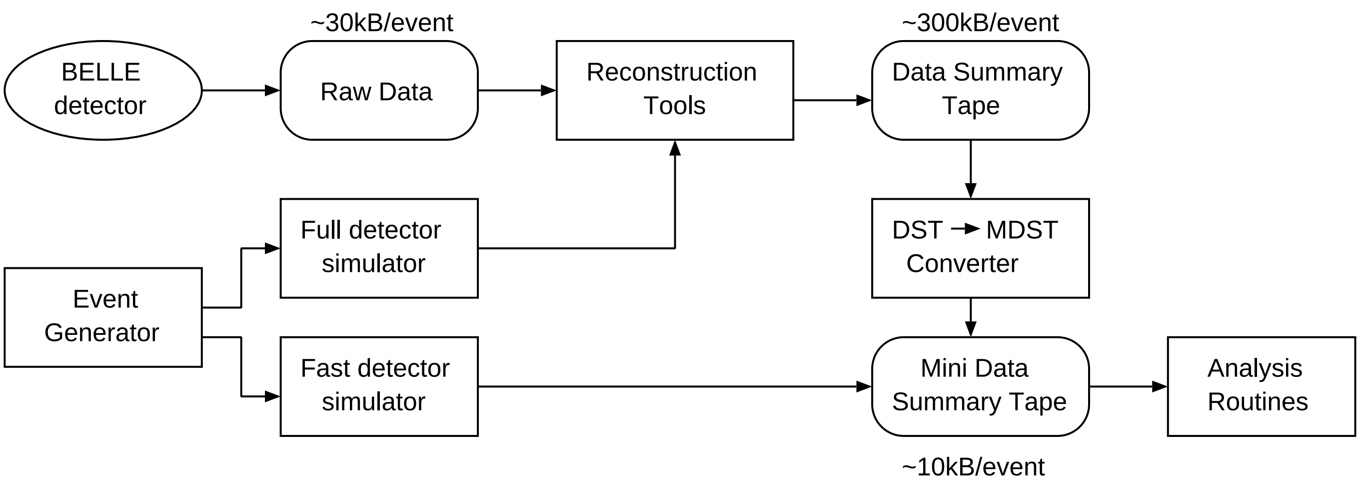

Figure 2.19: Flow of analysis

Chapter 3

Measurement of the D_{sJ} Resonance Properties

Abstract

We report measurements of two D_{sJ} resonance's masses, widths, and branching fractions in the continuum production. From the measurements of $D_{sJ}^+(2317) \to D_s^+\pi^0$ and $D_{sJ}^+(2457) \to D_s^{*+}\pi^0$, we determine their masses to be $M(D_{sJ}^+(2317)) = 2317.2 \pm 0.5$ (stat) $\pm$ 0.9 (syst) and $M(D_{sJ}^+(2457)) = 2456.5 \pm 1.3$ (stat) $\pm$ 1.3 (syst). We determine the ratio of branching fraction times cross section to be $(Br(D_{sJ}^+(2457) \to D_s^{*+}\pi^0) \times \sigma(D_{sJ}^+(2457)))/(Br(D_{sJ}^+(2317) \to D_s^+\pi^0) \times \sigma(D_{sJ}^+(2317))) = 0.29 \pm 0.06$ (stat) ± 0.03 (syst) and $(Br(Ds(2457) \to D_s\,\pi^0) \times \sigma(D_{sJ}^+(2457)))/(Br(Ds(2317) \to D_s\,\pi^0) \times \sigma(D_{sJ}^+(2317))) \leq 0.06$ $(90\% CL)$. We set upper limit for the branching fraction ratio to be $(Br(Ds(2457) \to D_s\pi^0))/(Br(Ds(2457) \to D_s^*\pi^0)) \leq 0.21$ $(90\% CL)$. We observe for the first time of the decay modes $D_{sJ}^+(2457) \to D_s\pi^+\pi^-$ and $D_{sJ}^+(2536) \to D_s\pi^+\pi^-$ modes. We determine the branching fraction ratio to be $(Br(D_{sJ}^+(2536) \to D_s^+\pi^+\pi^-))/(Br(D_{sJ}^+(2457) \to D_s^+\pi^+\pi^-)) = 1.05 \pm 0.32\ (stat) \pm 0.06\ (syst)$ and $(Br(D_{sJ}^+(2457) \to D_s^+\pi^+\pi^-))/(Br(D_{sJ}^+(2457) \to D_s^{*+}\pi^0)) = 0.14 \pm 0.04\ (stat) \pm 0.02\ (syst)$. We set upper limits for the branching fraction ratio to be $(Br(D_{sJ}^+(2317) \to D_s^+\pi^+\pi^-))/(Br(D_{sJ}^+(2317) \to D_s^+\pi^0)) \leq 4 \times 10^{-3}$ (90% $C.L.$). We observe for a radiative decay mode $D_{sJ}^+(2457) \to D_s^+\gamma$. We determine the branching fraction ratio to be $Br(D_{sJ}^+(2457) \to D_s^+\gamma)/Br(D_{sJ}^+(2457) \to D_s^{*+}\pi^0) = 0.55 \pm 0.13$ (stat) $\pm$ 0.08 (syst). We set upper limits for the branching fraction ratio to be $(Br(D_{sJ}(2317)^+ \to D_s^+\gamma))/(Br(D_{sJ}(2317)^+ \to D_s^+\pi^0)) \leq 0.05$, $(Br(D_{sJ}^+(2317) \to D_s^{*+}\gamma))/(Br(D_{sJ}^+(2317) \to D_s^+\pi^0)) \leq 0.18$ (90% $C.L.$), and $(Br(D_{sJ}^+(2457) \to D_s^{*+}\gamma))/(Br(D_{sJ}^+(2457) \to D_s^{*+}\pi^0)) \leq 0.31$ (90% $C.L.$). This analysis is based on 86.9 fb^{-1} taken with the BELLE detector and the KEKB accelerator. (BELLE NOTE#603)

3.1 Introduction

The narrow $D_s\pi^0$ resonance at 2317 MeV/c^2, recently observed by the BaBar collaboration [19], is naturally interpreted as a P-wave excitation of the $c\bar{s}$ system. The observation of a nearby and narrow $D_s^*\pi^0$ resonance by the CLEO collaboration [20] supports this view, since the mass difference of the two observed states is consistent with the expected hyperfine splitting for a P-wave doublet with total light-quark angular momentum $j = 1/2$ [21, 22]. The observed masses are, however, considerably lower than potential model predictions [24] and similar to those of the $c\bar{u}$ $j = 1/2$ doublet states recently reported by Belle [25]. This has led to speculation that the new $D_s^{(*)}\pi^0$ resonances, which we denote D_{sJ}, may be exotic mesons [26, 27, 28, 29, 30, 31]. Measurements of the D_{sJ} quantum numbers and branching fractions (particularly those for radiative decays), will play an important role in determining the nature of these states. In this paper we report measurements of the D_{sJ} masses, widths and branching fractions using a sample of $e^+e^- \to c\bar{c}$ events collected with the Belle detector [33] at the KEKB collider [34].

3.2 Data Set

We used hadronic events produced in e^+e^- annihilation at the KEKB accelerator and collected with BELLE detector. The data set has an integrated luminosity of 78.1 fb^{-1} taken at the $\Upsilon(4S)$ resonance (referred to as on-resonance data) and 8.8 fb^{-1} at a center of mass energy that is 60 MeV below the peak (referred to as off-resonance data or continuum data).

3.3 Reconstruction of ϕ, D_s, π^0, and D_s^{*+}

We use $D_s^+ \to \phi\pi^+$ and $\phi \to K^+K^-$ decay channels for D_s^+ reconstruction because it has the best combination of detection efficiency, branching ratio, and background suppression. To identify kaons or pions, we apply a mode dependent requirement on the ratio $L_K/(L_K+L_\pi)$ or $L_\pi/(L_K+L_\pi)$. We form K^+K^- invariant mass by requiring one track has $L_K/(L_K+L_\pi) > 0.5$ and another track has $L_K/(L_K + L_\pi) > 0.2$. Figure 4.11 shows the K^+K^- invariant mass distribution. We apply impact-parameter cuts of d_r and d_z which are the length between interaction point and the closest point of charged track in r and z direction respectively as to be $|d_r|$ less than 0.5 cm and $|d_z|$ less than 2 cm. The ϕ candidates must satisfy $M(K^+K^-)$ to be within 10 MeV/c^2 of the nominal ϕ mass. We use the ϕ helicity angle θ_H, which is the angle between the direction of the K^+ and the $D_s^\pm$ in the ϕ rest frame. The signal follows a $cos^2\theta_H$ distribution while the background is flat in $cos\theta_H$.

We require $|cos\theta_H|$ to be greater than 0.35. We reconstruct D_s^+ candidate in $D_s^+ \to \phi\pi^+$ decay by combining pion and ϕ candidates. We require $L_\pi/(L_K + L_\pi) > 0.1$ for the pion candidates. The invariant mass distribution for $\phi\pi^+$ that is applied continuum region momentum cut for $D_s\pi^0$ system as $P^*(D_s\pi^0) \geq 3.5$ GeV/c in the $\Upsilon(4S)$ frame is shown in Figure 4.12. The D_s candidates must satisfy $M(\phi\pi^+)$ to be within 10 MeV/c^2 of the D_s^+ nominal mass. We use the D_s^+ sideband region for background study that is defined as an average of $1.920 < M(\phi\pi^+) < 1.940$ GeV/c^2 and $1.998 < M(\phi\pi^+) < 2.018$ GeV/c^2.

For the π^0 reconstruction we require the energies of both photons to be greater than 100 MeV in the $\Upsilon(4S)$ frame. The $\gamma\gamma$ invariant mass distribution is shown in Figure 3.3. That is also applied continuum region momentum cut for $D_s\pi^0$ system as $P^*(D_s\pi^0) \geq 3.5$ GeV/c in the $\Upsilon(4S)$ frame. The π^0 candidates must have the $M(\gamma\gamma)$ within 10 MeV/c^2 of the π^0 nominal mass. We define the π^0 sideband region for background study as $0.105 \leq M_{\gamma\gamma} \leq 0.115$ GeV/c^2 and $0.155 \leq M_{\gamma\gamma} \leq 0.165$ GeV/c^2.

We reconstruct D_s^{*+} in the $D_s^+\gamma$ final state. We require the photons from the D_s^{*+} to have energy greater than 100 MeV in the $\Upsilon(4S)$ frame. The mass difference $M(D_s^+\gamma) - M(D_s^+)$ distribution is shown in Figures 3.4. That is also applied continuum region momentum cut for $D_s^*\pi^0$ system as $P^*(D_s^*\pi^0) \geq 3.5$ GeV/c in the $\Upsilon(4S)$ frame. The D_s^{*+} candidates must satisfy $0.127 \leq (M_{D_s^+\gamma} - M_{D_s^+}) \leq 0.157$ GeV/c^2. We define the D_s^{*+} sideband region for background study as an average of $0.087 \leq (M_{D_s^+\gamma} - M_{D_s^+}) \leq 0.117$ GeV/c^2 and $0.167 \leq (M_{D_s^+\gamma} - M_{D_s^+}) \leq 0.197$ GeV/c^2.

3.4 Monte Carlo Data

We need Monte Carlo simulations for production and decay of these new states. These simulations are used to estimate the experimental resolution for the resonance widths, detection efficiencies, and to understand the backgrounds due to feed-across. For the production of $D_{sJ}^+(2317)$ in continuum events, we replace the D_{0s}^+ with $D_{sJ}^+(2317)$ in the assumption of same fragmentation for them and let it decay to $D_s^+\pi^0$ according to a phase space. We assign the mean value as 2317.0 MeV and assign the intrinsic width of $D_{sJ}^+(2317)$ as 0 MeV/c^2. For the production of $D_{sJ}^+(2457)$ in continuum events, we replace $D_{s1}'^+$ with $D_{sJ}^+(2457)$ and let it decay to $D_s^{*+}\pi^0$ according to phase space. We assign the mean value as 2459.0 MeV and assign the intrinsic width of $D_{sJ}^+(2457)$ as 0 MeV/c^2.

3.5 Study of $D_s(2317)^+ \to D_s^+\pi^0$

The invariant mass distribution for $D_s^+\pi^0$ combinations with center of mass momentum $p^*(D_s^+\pi^0)$ greater than 3.5 GeV/c is shown in Figure 3.5. This requirement removes $D_s^+\pi^0$ combinations from B decays. The mass difference $M(D_s^+\pi^0) - M_{D_s^+}$ is shown in Figure 3.6. Also shown are the backgrounds from the D_s^+ sideband (dark dotted lines) and π^0 sideband (light dotted lines). A clear peak in the 2.32 GeV/c^2 mass region is visible in addition to a peak at 2.1 GeV/c^2 corresponding to $D_s^{*+}(2112) \to D_s^+\pi^0$. No peak is seen in the sideband distributions. We extract the raw yield, mean, and σ of the peak from both mass distribution and mass difference distribution by using a single Gaussian to model for the signal shape and a third order polynomial function for the background shape. We obtain the following results for raw yield with $87fb^{-1}$ data,

- From the $D_{sJ}(2317)$ mass distribution:
  - Raw yield $= 867 \pm 44$
  - Mean 2317.0 ± 0.5 MeV/c^2
  - $\sigma = 7.9 \pm 0.5$ MeV/c^2
    (statistical error only)
- From the mass difference distribution:
  - Raw yield $= 886 \pm 46$
  - Mean 348.3 ± 0.5 MeV/c^2
    (correspond to 2316.8 ± 0.5 MeV/c^2)

- $\sigma = 8.2 \pm 0.5$ MeV/c^2
  (statistical error only)

In the invariant mass calculation, we substitute the D_s^+ nominal mass and use the π^0 momentum which is recalculated after the mass constraint fit. For the mass difference calculation, only the π^0 mass constraint fit is used. Both methods give consistent results and our measured mass is in good agreement with BaBar and CLEO results. Extraction of signal yields, mean, and observed width after feed-across correction will be discussed in later section. The extraction of natural width from the observed width will be also discussed in the section.

3.6 Study of $D_s(2457)^+ \to D_s^{*+}\pi^0$

Figures 3.7 and 3.8 show the invariant mass distribution $M(D_s^{*+}\pi^0)$ and mass difference $M(D_s^{*+}\pi^0) - M_{D_s^{*+}}$ distribution. The momentum cut $p^*(D_s^{*+}\pi^0) > 3.5$ GeV/c is applied. A clear peak is observed in the 2.46 GeV/c^2 region as reported by BaBar and CLEO.

We extract the yield, mean, and σ of the peak from the mass distribution and the mass difference distribution using the same method as for the $D_{sJ}(2317)$ case. Results of the fitting by single Gaussian for raw yield with $87fb^{-1}$ data are following.

- From the $D_{sJ}(2457)$ mass distribution:
  - Raw yield $= 206 \pm 25$
  - Mean $=2457.1 \pm 1.3$ MeV/c^2
  - $\sigma = 7.4 \pm 1.5$ MeV/c^2
    (statistical error only)
- From the mass difference distribution:
  - Raw yield $= 207 \pm 25$
  - Mean $= 344.7 \pm 1.0$ MeV/c^2
    (correspond to 2457.1 ± 1.0 MeV/c^2)
  - $\sigma = 7.4 \pm 1.1$ MeV/c^2
    (statistical error only)

Again both methods give consistent results. For the rest of this article, we use the mass difference only. Extraction of signal yields, mean, and observed width after feed-across correction will be discussed in later section. The extraction of natural width from the observed width will be also discussed in the section.

3.7 Experimental Resolution

We estimate the experimental resolution for the resonance widths using the signal Monte Carlo events. Since we observe a clear peak for $D_s^{*+} \to D_s^+\pi^0$ in the data, we use the decay chain to compare experimental resolution with the Monte Carlo. Figure 3.9 show the mass difference $M(D_s^+\pi^0) - M_{D_s^+}$ distribution near the $D_s^{*+}(2112)$ mass region. Figure 3.10 shows the corresponding MC distribution. Fitting with a single Gaussian for signal shape and a threshold function for background give following results.

- Data:
  - Mean = (144.3 ± 0.1) MeV/c^2
    (correspond to 2112.8 ± 0.1 MeV/c^2)
  - $\sigma = (1.0 \pm 0.1)$ MeV/c^2
    (statistical error only)
- MC:
  - Mean = (143.9 ± 0.1) MeV/c^2
    (correspond to 2112.4 ± 0.1 MeV/c^2)
  - $\sigma = (1.0 \pm 0.1)$ MeV/c^2
    (statistical error only)

The observed mean 144.3 ± 0.1 MeV/c^2 corresponds to a D_s^{*+} mass of 2112.8 ± 0.1 MeV/c^2. This agrees with the PDG2002 value of 2112.4 ± 0.7 MeV/c^2. The observed width is in good agreement with MC. We conclude that we can obtain reliable estimate of the experimental resolution from the MC result when extract the natural widths.

Figures 3.11 and 3.12 show each mass difference distribution $M(D_s^+\pi^0) - M_{D_s^+}$ and $M(D_s^{*+}\pi^0) - M_{D_s^{*+}}$ of signal Monte Carlo from $D_{sJ}(2317)$ and $D_{sJ}(2457)$ respectively. We fit the $M(D_s^+\pi^0) - M_{D_s^+}$ MC distribution with a single Gaussian for signal shape and a third order polynomial function for background shape. In the case of $D_{sJ}(2457)$, there is a background peak of miss combination with random photon, therefore we fit the $M(D_s^{*+}\pi^0) - M_{D_s^{*+}}$ MC distribution after D_s^* sideband distribution was subtracted bin by bin. Each fitting give us following results.

- For $D_{sJ}(2317)$:
  - Mean = 348.7 ± 0.2 MeV/c^2
    (correspond to 2317.2 ± 0.2 MeV/c^2)

  - $\sigma = 7.1 \pm 0.2$ MeV/c^2
    (statistical error only)

- For $D_{sJ}(2457)$:
  - Mean $= 347.5 \pm 0.2$ MeV/c^2
    (correspond to 2459.9 ± 0.2 MeV/c^2)
  - $\sigma = 6.1 \pm 0.2$ MeV/c^2
    (statistical error only)

We conclude that our experimental resolution for each mass is 7.1 ± 0.2 MeV/c^2 for $D_{sJ}(2317)$ and 6.1 ± 0.2 MeV/c^2 for $D_{sJ}(2457)$.

3.8 Background estimation

Since the kinematics of the $D_s(2457) \to D_s^* \pi^0$ decay is similar to the $D_s(2317) \to D_s \pi^0$, background due to reflections from another state can also make peaks in each signal region. Reflection background for the $D_s(2457) \to D_s^{*+} \pi^0$ can come from D_s^+ and π^0, originating from $D_s(2317) \to D_s^+ \pi^0$, which are combined with random photon and happens to pass the $|M(D_s^+ \gamma) - M_{D_s^{*+}}| < 15$ MeV/c^2 requirement. Reflection background for the $D_s(2317) \to D_s^+ \pi^0$ can come from D_s^+ and π^0 originating from $D_s(2457) \to D_s^+ \gamma \pi^0$.

This effect is clearly demonstrated by data distribution in Figure 3.13 and 3.14. Figure 3.13 shows the $M(D_s^* \pi^0) - M_{D_s^{*+}}$ distributions from the data for the D_s^+ signal and sideband regions. There is no peak in the D_s^+ sideband. On the other hand, a reflection is clearly seen in the D_s^{*+} sideband distributions as shown in Figure 3.14. The definitions for the D_s^{*+} signal and sideband regions are shown in Figure 3.4. Both lower and higher sideband regions are chosen to be equal to the area under the peak in the signal region, and an average of the two regions is used as the sideband distribution.

A broader peak in the D_s^{*+} sideband distribution is a result of the feed-up background plus the broken combination background as described in the previous subsections. These should be present in the distribution for the D_s^{*+} signal region as well. We therefore must separate these components in order to extract signal yields, means and the correct observed widths of the resonances.

3.8.1 Feed-up from D_{sJ}(2317) to D_{sJ}(2457)

Figure 3.15(a) cross points show the $M(D_s^{*+} \pi^0) - M_{D_s^{*+}}$ distribution obtained from the $D_{sJ}(2317)$ signal MC events. A clear peak seen near 2.46 GeV/c^2 resonance is a result of D_s^+ and π^0 from $D_{sJ}(2317)$ combining with random photon and the $D_s^+ \gamma$ combination satisfying the D_s^{*+} requirement. A fit using a Gaussian for the feed-up peak and linear function for the smooth background gives the mean of (351.9 ± 2.5) MeV/c^2 which correspond to (2464.3 ± 2.5) MeV/c^2 and σ of (12.3 ± 1.8) MeV/c^2. The peak position is slightly higher than the signal, and the width is about twice wider than the signal width. The χ^2/n.d.f is 4.5/4 in this fitting. Figure 3.15(a) histogram show the $M(D_s^{*+} \pi^0) - M_{D_s^{*+}}$ distribution by using D_s^* sideband region obtained from the same $D_{sJ}(2317)$ signal MC events. We can confirm that the D_s^* sideband is containing the feed-up peak with the same shape and same fraction. We define the feed-up fraction as a yield ratio of the feed-up events to the $D_{sJ}(2317)$ events that are correctly reconstructed as signal. We estimate the fraction as $f^{\rm up} = (9.2 \pm 1.8)\%$.

3.8.2 Feed-down from $D_{sJ}(2457)$ to $D_{sJ}(2317)$

Figures 3.15(b) show the $M(D_s^+\pi^0) - M_{D_s^+}$ distributions from the $D_{sJ}(2457)$ signal Monte Carlo events. A clear feed-down peak can be seen near 2.32 GeV/c^2 which comes from D_s^+ and π^0 combination from $D_{sJ}(2457)$ decay. We obtain the mean of (346.8 ± 1.0) MeV/c^2 which correspond to (2315.3 ± 1.0) MeV/c^2 and the σ of (14.9 ± 0.8) MeV/c^2. The peak is slightly lower than the signal peak and the width is about twice as wide as the signal width. The χ^2/n.d.f is 23/19 in this fitting. This feed-down mean value depends directly on the input mean value of $D_{sJ}(2457)$ that is 2459.0 MeV/c^2. Otherwise, we find the true mean of $D_{sJ}(2457)$ is 2456.6 MeV/c^2 as described later, therefore we use (344.4 ± 1.0) MeV/c^2 as the feed-down mean value. The feed-down fraction which is defined as a yield ratio of the feed-down events to correctly reconstructed $D_{sJ}(2457)$ events. The feed-down fraction is estimated as $f^{\rm down} = (132 \pm 13)\%$.

3.8.3 Broken combination from $D_{sJ}(2457)$ to $D_{sJ}(2457)$

Figures 3.15(c) show the $M(D_s^{*+}\pi^0) - M_{D_s^{*+}}$ distributions from the D_s^{*+} sideband region in the $D_{sJ}(2457)$ MC. A peak comes from a random photon combined with D_s^+ from $D_{sJ}(2457)$ decay when the combination satisfies the D_s^{*+} requirement and then forming peak around 2.46 GeV/c^2. We obtain the mean of (347.8 ± 4.2) MeV/c^2 which correspond to (2460.2 ± 4.2) MeV/c^2 and $\sigma = (19.5 \pm 3.6)$ MeV/c^2. The peak coincides with the signal within the error, but the width is wider than the signal. The χ^2/n.d.f is 14/32 in this fitting. This broken-combination mean value depends directly on the input mean value of $D_{sJ}(2457)$ that is 2459.0 MeV/c^2. Otherwise, we find the true mean of $D_{sJ}(2457)$ is 2456.6 MeV/c^2 as described later, therefore we use (345.4 ± 4.2) MeV/c^2 as the broken-combination mean value. The broken-combination fraction which is defined as a yield ratio of the broken-combination events to correctly reconstructed $D_{sJ}(2457)$ events. The broken-combination fraction is estimated as $f^{\rm broken} = (15.6 \pm 3.5)\%$.

3.9 Signal yields extraction

Since D_s^* sideband contains both feed-up background and broken-combination background, we extract $D_{sJ}(2457)$ signal with subtraction of D_s^* sideband's $M(D_s^{*+}\pi^0) - M_{D_s^{*+}}$ distribution from D_s^* signal's $M(D_s^{*+}\pi^0) - M_{D_s^{*+}}$ distribution bin by bin as shown in Figure 3.16. We fit the $M(D_s^{*+}\pi^0) - M_{D_s^{*+}}$ distribution with single Gaussian for signal shape and 2nd polynomial for background shape. After the extraction of true yields of $D_{sJ}(2457)$, we fit the $M(D_s^{+}\pi^0) - M_{D_s^{+}}$ distribution with single Gaussian for signal shape, Monte Carlo predicted Gaussian for feed-down component, and 3rd polynomial for combinatorial background shape as shown in Figure 3.17. The fitting results are as following,

- From the $M(D_s^{*+}\pi^0) - M_{D_s^{*+}}$ distribution after sideband subtraction:
  - Signal yield = 125.8 ± 25
  - Mean =344.1 ± 1.3 MeV/c^2
    (correspond to 2456.5 ± 1.3 MeV/c^2)
  - $\sigma = 5.8 \pm 1.3$ MeV/c^2
    (statistical error only)
- From the $M(D_s^{+}\pi^0) - M_{D_s^{+}}$ distribution with sideband subtraction method:
  - Signal yield = 761 ± 44
  - Mean =348.7 ± 0.5 MeV/c^2
    (correspond to 2317.2 ± 0.5 MeV/c^2)
  - $\sigma = 7.6 \pm 0.5$ MeV/c^2
    (statistical error only)

3.10 Systematics of D_{sJ} properties

We estimate systematic uncertainty of yields, mean, and observed width both for $D_{sJ}(2317)$ and $D_{sJ}(2457)$ respectively. In the $D_{sJ}(2457)$ case, we use linear function as different parameterization for combinatorial background estimation. We assign the mean shift uncertainty with the difference between input MC mean and measured MC mean value. We estimate the photon energy correction factor from the difference between the measured mass difference 144.3 $\pm$ 0.1 MeV/c^2 and PDG value 143.8 $\pm$ 0.4 MeV/c^2. We assign the difference 0.5 $\pm$ 0.4 MeV/c^2 as photon energy systematic uncertainty. In the $D_{sJ}(2317)$ case, we vary $\pm 1\sigma$ of yields, mean, and observed width for feed-up Gaussian shape, and we also changed $\pm 1\sigma$ of statistics for yields of the $D_{sJ}(2457)$. We use 2nd polynomial function to estimate combinatorial background parameterization uncertainty. We also assign the mean shift uncertainty with the mean value statistics in signal Monte Carlo. We assign photon energy systematic uncertainty same as the case of $D_{sJ}(2457)$. We use D_s^* sideband to estimate feed-up events in data, and the feed-up event number is well consistent between D_s^* signal region and D_s^* sideband region in MC. We estimate the error of yields in sideband subtraction from the uncertainty of feed-up events correspond to $\pm$ 3 σ of signal Gaussian region in MC. We estimate the uncertainty of mean in sideband subtraction from the difference between mean of feed-up in D_s^* signal region and mean of feed-up in D_s^* sideband region. We estimate the uncertainty of observed width in sideband subtraction from the difference between sideband- subtraction method and simultaneous method which described in next section. Those systematics are summarized in the Table 3.1 and 3.2.

Table 3.1: Systematics of $D_{sJ}(2457)$ with bin-by-bin subtraction method

$D_{sJ}(2457)$	Yield	dM (Mean) [MeV/c^2]	Observed width [MeV/c^2]
Combinatorial B.G. parameterization (linear)	$\pm$ 6.8%	$\pm$0.1	$\pm$0.3
Photon energy calibration	-	$\pm$0.6	$\pm$0.1
Mean shift in signal MC	-	$\pm$0.9	-
Sideband B.G. subtraction	$\pm$6.5%	$\pm$0.2	$\pm$0.3
PDG D_s^* Mean	-	($\pm$ 0.7)	-
Total	$\pm$ 9.4%	$\pm$ 1.1 (1.3)	$\pm$ 0.4

Table 3.2: Systematics of $D_{sJ}(2317)$ with bin-by-bin subtraction method

$D_{sJ}(2317)$	Yield	dM (Mean) [MeV/c^2]	Observed width [MeV/c^2]
Feed-down fraction ($\pm\sigma$)	$\pm$1.8%	*negligible* -0.1	-0.1 $+0.1$
Feed-down Mean ($\pm\sigma$)	negligible	-0.1 $+0.1$	*negligible* *negligible*
Feed-down width ($\pm\sigma$)	$\pm$ 0.6%	-0.1 *negligible*	*negligible* *negligible*
$D_{sJ}(2457)$ Yield ($\pm\sigma$)	$\pm$ 3.5%	*negligible* -0.1	-0.2 $+0.2$
B.G. parameterization (2nd polynomial)	negligible	negligible	negligible
Photon energy calibration	-	$\pm$0.6	$\pm$0.1
Mean shift in signal MC	-	$\pm$ 0.3	-
PDG D_s Mean	-	($\pm$ 0.6)	-
Total	$\pm$ 4.0%	$\pm$ 0.7 (0.9)	$\pm$ 0.3

3.11 Consistency check with simultaneous fitting

We perform a simultaneous fit to the two mass difference distributions, $M(D_s^+\pi^0) - M_{D_s^+}$ and $M(D_s^{*+}\pi^0) - M_{D_s^{*+}}$ with including the reflection effects. We use the following fitting functions

$$\begin{aligned}\Delta M(2317) &= A_1 G(\mu_1, \sigma_1) + 1.32 A_2 G(\mu^{\mathrm{down}}, \sigma^{\mathrm{down}}) \\ \Delta M(2457) &= A_2 G(\mu_2, \sigma_2) + 0.092 A_1 G(\mu^{\mathrm{up}}, \sigma^{\mathrm{up}}) + 0.156 A_2 G(\mu^{\mathrm{broken}}, \sigma^{\mathrm{broken}})\end{aligned} \tag{3.1}$$

The $G(\mu, \sigma)$ is a Gaussian with a mean μ and a sigma σ. Free parameters in this fitting are the true yields A_1 and A_2, the means μ_1 and μ_2, and the widths σ_1 and σ_2 both for $D_{sJ}(2317)$ and $D_{sJ}(2457)$. All other parameter are fixed from the MC prediction. Fitting results for two distribution are shown in Figure 3.18 respectively with each component. Input parameters and the fitting result are summarized in Table 3.3.

These results are consistent with bin-by-bin subtraction method for mean and observed width. We observe 151 ± 23 events for the $D_{sJ}(2457) \to D_s^{*+}\pi^0$ decay by simultaneous fitting. In the case of yields, MC prediction for feed-up and broken-combination are smaller because of the difference of background photon between data and MC. Otherwise feed-down should be well described because it's just missing of the signal photon. Therefore we use sideband subtraction method for $D_{sJ}(2457)$. The comparison between two method are summarized in the Table 3.4.

Table 3.3: Summary of simultaneous fitting results for data

Resonance	Parameter	Narrow Gaussian (true signal)	Wide Gaussian (feed-across)	Lower wide Gaussian (broken combination)
$D_{sJ}(2317)$	Yield	740 ± 52	195 ± 30 ($1.32A_2$)	-
	Mean (MeV/c^2)	348.7 ± 0.5	344.4 (fixed)	-
	σ (MeV/c^2)	7.4 ± 0.5	14.9 (fixed)	-
$D_{sJ}(2457)$	Yield	148 ± 23	68 ± 4.8 ($0.092A_1$)	23 ± 3.6 ($0.156A_2$)
	Mean (MeV/c^2)	343.7 ± 1.0	351.9 (fixed)	345.4 (fixed)
	σ (MeV/c^2)	6.1 ± 1.1	12.3 (fixed)	19.5 (fixed)

Table 3.4: Comparison of results for two counting methods

Resonance	Parameter	Simultaneous fitting	Bin-by-bin sideband subtraction
$D_{sJ}(2317)$	Yield	740 ± 52	$761 \pm 44 \pm 30$
	dM (MeV/c^2)	348.7 ± 0.5	$348.7 \pm 0.5 \pm 0.7$
	Mean (MeV/c^2)	2317.2 ± 0.5	$2317.2 \pm 0.5 \pm 0.9$
	σ (MeV/c^2)	7.4 ± 0.5	$7.6 \pm 0.5 \pm 0.3$
$D_{sJ}(2457)$	Yield	148 ± 23	$126 \pm 25 \pm 12$
	dM (MeV/c^2)	343.7 ± 1.0	$344.1 \pm 1.3 \pm 1.1$
	Mean (MeV/c^2)	2456.1 ± 1.0	$2456.5 \pm 1.3 \pm 1.3$
	σ (MeV/c^2)	6.1 ± 1.1	$5.8 \pm 1.3 \pm 0.4$

First error is statistical and second is systematic error.

3.12 Branching ratio times cross section

The partial efficiencies for $D_{sJ}(2317) \to D_s\ \pi^0$ and $D_{sJ}(2457) \to D_s^*\ \pi^0$ with 3.5 GeV/c momentum cut are $(8.18 \pm 0.24)\%$ and $(4.68 \pm 0.14)\%$ respectively. Then we estimate the branching ratio times cross section as

$$\frac{Br(D_{sJ}(2457) \to D_s^*\ \pi^0)}{Br(D_{sJ}(2317) \to D_s\ \pi^0)} \times \frac{\sigma(Ds(2457), P^* \geq 3.5GeV/c)}{\sigma(Ds(2317), P^* \geq 3.5GeV/c)} = \frac{126/4.7\%}{761/8.2\%} = 0.29 \pm 0.06\ (stat) \pm 0.03\ (syst) \tag{3.2}$$

The systematic error of photon efficiency was evaluated from π^0 efficiency ratio between MC and data as 3.3 % [32]. Systematic errors are summarized on Table 3.5.

Table 3.5: Summary of systematics for branching ratio times cross section

Error source	systematic uncertainty
Systematics of $D_{sJ}(2457)$ yields	9.4 %
Systematics of $D_{sJ}(2317)$ yields	4.0 %
Photon efficiency	3.3 %
$D_{sJ}(2457) \to D_s^*\ \pi^0$ MC statistics	3.0 %
$D_{sJ}(2317) \to D_s\ \pi^0$ MC statistics	2.9 %
Total	11 %

If a particle decay into pair of pseudoscalar, the spin of parent particle and orbital angular momentum of final state is equal from angular momentum conservation. Then the parity of final state which is represent as (-1) × (-1) × $(-1)^L$ is equal to (-1) × (-1) × $(-1)^J$. It means if we decide the spin of a particle, we can decide the parity from whether it decay into pair of pseudoscalar or not. We assign the upper limit for $D_sJ(2457)^+ \to D_s^+\pi^0$ mode by fitting on $D_sJ(2457)^+$ region of Figure 3.6 with signal shape predicted from MC. We use the efficiency 11% and obtain the fitted result as 22 ± 22 event respectively. Then we extract the upper limit with the assumption of Gaussian and use the 90% of the positive area.

$$\frac{Br(Ds(2457) \to D_s\ \pi^0) \times \sigma(D_{sJ}^+(2457))}{Br(Ds(2317) \to D_s\ \pi^0) \times \sigma(D_{sJ}^+(2317))} \leq 0.06\ (90\%CL) \tag{3.3}$$

$$\frac{Br(Ds(2457) \to D_s\ \pi^0)}{Br(Ds(2457) \to D_s^*\ \pi^0)} \leq 0.21\ (90\%CL) \tag{3.4}$$

3.13 Radiative decays

3.13.1 $D_{sJ} \to D_s\gamma$

The $D_s(2317) \to D_s\gamma$ decay is forbidden if $D_s(2317)$ has a spin 0 state from the angular momentum conservation. $D_s(2457) \to D_s\gamma$ is allowed if $D_s(2457)$ is 1^+ state or 1^- state. Figure 3.19 shows the mass difference distribution for $D_s\gamma$ obtained by combining the D_s signal candidate with photons above $E^*_\gamma = 600$ MeV after removing all photons that form a π^0. The cut criteria for photon energy was optimized to maximize the F.O.M which defined as $S/\sqrt{S+N}$ from signal MC and data sideband. We require $p^*(D_{sJ} > 3.5)$ GeV/c. The histogram is from D_s^+ sideband region. We use a double Gaussian as signal shape and 3rd oder polynomial as background. Then we fix the double Gaussian's shape except for the total yields and narrow widths. The ratio of narrow Gaussian to wide Gaussian is 0.67 ± 0.21, two Gaussian's mean difference is 14.3 ± 4.1 MeV/c^2, and the wider Gaussian's width is 17.6 ± 2.0 MeV/c^2. The observed signal yield is $152 \pm 18(stat)$ events. The double counting fraction was estimated as less than 1% from signal MC. This exclude a possibility of $D_s(2457)$ being $0^\pm$ state. We correct mean value with the difference between input $D_s(2457)$ mean value of 2459.0 MeV/c^2 and measured narrow Gaussian's mean value of 2459.6 MeV/c^2 in MC. From the measured narrow Gaussian's mean value of 2460.1 MeV/c^2 in data, we determined the mean value as 2459.5 MeV/c^2 after signal shape correction.

- $D_{sJ}(2457) \to D_s\gamma$ Data;
  - Narrow Gaussian's $\Delta M = 491.6 \pm 1.3$ MeV/c^2
  - Narrow Gaussian's $M = 2460.1 \pm 1.3$ MeV/c^2
  - Narrow Gaussian's $\sigma = 8.0 \pm 1.1$ MeV/c^2
  - $\Delta M = 491.0 \pm 1.3$ MeV/c^2
  - $M = 2459.5 \pm 1.3$ MeV/c^2
    (statistical error only)

- $D_{sJ}(2457) \to D_s\gamma$ MC;
  - Narrow Gaussian's $\Delta M = 491.1 \pm 0.9$ MeV/c^2
  - Narrow Gaussian's $M = 2459.6 \pm 0.9$ MeV/c^2

– Narrow Gaussian's $\sigma = 8.5 \pm 0.8$ MeV/c^2
(statistical error only)

The systematics for $D_{sJ}(2457) \to D_s\gamma$ are summarized in Table 3.6. We measure $D_{sJ}(2112) \to D_s\gamma$ with same cut criteria as Figure 3.22. The measured mass difference's mean is 145.5 ± 0.4 MeV/c^2, otherwise PDG value is 143.8 ± 0.4 MeV/c^2. We assign the difference 1.7 ± 0.6 MeV/c^2 as systematic uncertainty. We check the generic charm MC correspond to ∼120 fb^{-1} in order to estimate unexpected reflection Figure 3.20. Then we fit with signal shape and the reflection background is estimated as 16.3 ± 10.7 events after normalize to data. We assign the error as unexpected reflection uncertainty. We change background shape from 3rd polynomial to 2nd polynomial, and vary $\pm 1\sigma$ for the fixed variable of signal shape in the systematic study.

Table 3.6: Summary of systematics for $D_{sJ}(2457) \to D_s\gamma$

$D_{sJ}(2457)$	Yield	dM (Mean) [MeV/c^2]
B.G. parameterization (2nd polynomial)	± 3.9%	±0.1
Photon energy calibration	-	±1.8
Mean shift in signal MC	-	±0.5
Ratio of two Gaussian ($\pm\sigma$)	∓ 3.1%	±0.2
Mean difference of two Gaussian ($\pm\sigma$)	± 1.4%	∓ 0.1
Wider Gaussian's width ($\pm\sigma$)	± 1.4%	±0.1
PDG D_s Mean	-	(± 0.6)
Generic charm MC statistics	±7.0%	-
Total	±8.8%	±1.9 (±2.0)

We calculate the partial efficiency for $D_sJ(2457)^+ \to D_s^+\gamma$ with 3.5 GeV/c momentum cut as (10.2 ± 0.3) %. We extract the branching fraction ratio of two decay mode as

$$\frac{Br(D_sJ(2457)^+ \to D_s^+\gamma)}{Br(D_sJ(2457)^+ \to D_s^{*+}\pi^0)} = 0.55 \pm 0.13\ (stat) \pm 0.08\ (syst) \tag{3.5}$$

Systematic errors are summarized on Table 3.5. The systematic error of π^0 efficiency was evaluated from the efficiency ratio between MC and data in the BELLE note #645 as 4.6 %. We assign one photon systematic error conservatively because two photon energy in $D_sJ(2457)^+ \to D_s^+\gamma$ and $D_s(2112)^+ \to D_s^+\gamma$ are different.

Table 3.7: Summary of systematics for $D_sJ(2457)$ branching ratio

Error source	systematic uncertainty
Systematics of $D_{sJ}(2457)^+ \to D_s^{*+}\pi^0$ yields	9.4 %
Systematics of $D_{sJ}(2457)^+ \to D_s^+\gamma$ yields	8.8 %
π^0 efficiency	4.6 %
γ efficiency	3.3 %
$D_{sJ}(2457)^+ \to D_s^{*+}\pi^0$ MC statistics	3.0 %
$D_{sJ}(2457)^+ \to D_s^+\gamma$ MC statistics	2.9 %
E_γ^* cut dependence	1.6 %
Total	15 %

We also assign the upper limit for $D_sJ(2317)^+ \to D_s^+\gamma$ mode by fitting on $D_sJ(2317)^+$ region of Figure 3.19 with signal shape predicted from MC. We use the efficiency and fitted result as 8.2% and 11 $\pm$ 16 event respectively. Also we extract the upper limit with the assumption of Gaussian and use the 90% of the area.

$$\frac{Br(Ds(2317) \to D_s\ \gamma)}{Br(Ds(2317) \to D_s\ \pi^0)} \leq 0.05\ (90\%CL) \tag{3.6}$$

3.13.2 $D_{sJ} \to D_s^* \gamma$

Both 0^+ and 1^+ states are allowed to decay to $D_s^*\gamma$. Figure 3.23 shows the mass difference distribution for $D_s^*\gamma$ - D_s^* where D_s^* signal candidates are combined with photons which have $E_\gamma^* > 400$ MeV after removing all photons that form a π^0. The cut criteria for photon energy was optimized to maximize the F.O.M which defined as $S/\sqrt{S+N}$ from signal MC and data sideband. We require $p^*(D_{sJ} > 3.5)$ GeV/c. We use each Gaussian as signal shape and 3rd oder polynomial as background. Then we fix the Gaussian's shape except for the total yields. The partial efficiency is $(2.0 \pm 0.4)\%$ for $D_{sJ}(2317)$ and $(5.0 \pm 0.6)\%$ for $D_{sJ}(2457)$. The observed yields is 13 ± 10 events for$D_{sJ}(2317)$ and 21 ± 11 events for$D_{sJ}(2457)$. No peak is visible at the region correspond to both 2.32 and 2.46 GeV/c^2. We set upper limits for these branching fraction ratio.

$$\frac{Br(D_s(2317)^+ \to D_s^{*+}\gamma)}{Br(D_s(2317)^+ \to D_s^+\pi^0)} < 0.18(90\%C.L.) \tag{3.7}$$

$$\frac{Br(D_s(2457)^+ \to D_s^{*+}\gamma)}{Br(D_s(2457)^+ \to D_s^{*+}\pi^0)} < 0.31(90\%C.L) \tag{3.8}$$

Then we assume Gaussian and use the positive area. We only use statistic error to set upper limits. Efficiency was deviated with $\pm\sigma$ conservative value.

3.14 First observation of $D_{sJ} \to D_s\pi^+\pi^-$

The $D_s(2317)$ is not allowed to decay to $D_s\pi^+\pi^-$ if it is 0^+ state. Figure 3.24 shows the mass distribution for $D_s\pi^+\pi^-$ where the D_s signal candidates are combined with $\pi^+\pi^-$ pairs. Pions are required to satisfy one $L_\pi/(L_\pi + L_K) > 0.9$ and another $L_\pi/(L_\pi + L_K) > 0.1$. Mass of $D_{sJ}(2457)$ is below than $D_sK\pi$ threshold and PID cuts variation dose not affect signal efficiency and it's for combinatorial background suppression. Momentum cuts is applied that one P^*_π is greater than 300 MeV/c. These cut values are decided from F.O.M. analysis in order to observe this decay mode. We require $\pi^+\pi^-$ invariant mass to be $|M_{\pi^+\pi^-} - M_{K_s}| \geq 15MeV/c^2$ to reduce $\pi^+\pi^-$ pairs from K^0_s. We also require $p^*(D_s\pi^+\pi^-) > 3.5$GeV/c. Partial efficiency for three states are (14.4 ± 1.1)% for $D_{sJ}(2317)$, (15.9 ± 0.3)% for $D_{sJ}(2457)$, and (14.3 ± 0.3)% for $D_{sJ}(2536)$ respectively. Observed yields are -4.5 ± 2.9(stat) for $D_{sJ}(2317)$, 59.7 ± 11.5(stat) for $D_{sJ}(2457)$ and 56.5 ± 13.4(stat) for $D_{sJ}(2536)$. Signal widths were fixed by MC prediction. Background shape is 3rd order polynomial. Systematic errors are summarized on Table 3.8 and Table 3.9. There is no clear yields in the region for $D^+_{sJ}(2317) \to D^+_s\pi^+\pi^-$. The Monte Carlo efficiency is (14.4+-1.1)% and we fitted data by the signal shape for this mode from Monte Carlo and then the yields was -4.0 ± 2.9. We deviated 90% C.L. upper limit from the yield of 2.9 times 1.65 σ and then two efficiencies are with one sigma consevative value.

Table 3.8: Systematics of $D^+_{sJ}(2457) \to D^+_s\pi^+\pi^-$ analysis

	$D_{sJ}(2457)$ Yield	$D_{sJ}(2457)$ Mean [MeV/c^2]	$\frac{Br(D^+_{sJ}(2536)\to D^+_s\pi^+\pi^-)}{Br(D^+_{sJ}(2457)\to D^+_s\pi^+\pi^-)}$
$D_{sJ}(2457)$ Signal shape ($\pm\sigma$)	± 1.2%	negligible	±2.6%
$D_{sJ}(2536)$ Signal shape ($\pm\sigma$)	-	-	±3.3%
B.G. parameterization	± 0.2%	negligible	±1.6%
$\pi^\pm$ momentum calibration	-	± 1.4	-
MC statistics $D_{sJ}(2457)$	-	± 0.1	±2.2%
MC statistics $D_{sJ}(2536)$	-	-	±2.4%
Mean shift in signal MC	-	± 0.1	-
Without $\pi^\pm$ momentum cut	-	±0.6	±1.5%
PDG	-	(0.6)	-
Total	± 1.2%	± 1.5 (1.6)	± 5.7%

$$\frac{Br(D_{sJ}^{+}(2457) \to D_s^+\pi^+\pi^-)}{Br(D_{sJ}^{+}(2457) \to D_s^{*+}\pi^0)} = 0.14 \pm 0.04(stat) \pm 0.02(syst) \tag{3.9}$$

$$\frac{Br(D_{sJ}^{+}(2317) \to D_s^+\pi^+\pi^-)}{Br(D_{sJ}^{+}(2317) \to D_s^{+}\pi^0)} \leq 4 \times 10^{-3} \text{ } (90\% \text{ } C.L.) \tag{3.10}$$

Assuming the same fragmentation function for the $D_{sJ}(2536)$ and $D_{sJ}(2457)$, we establish the the cross section times branching fraction ratio

$$\frac{Br(D_{sJ}^{+}(2536) \to D_s^+\pi^+\pi^-)}{Br(D_{sJ}^{+}(2457) \to D_s^{+}\pi^+\pi^-)} = 1.05 \pm 0.32(stat) \pm 0.06(syst) \tag{3.11}$$

Table 3.9: Summary of $\frac{Br(D_{sJ}^{+}(2457) \to D_s^+\pi^+\pi^-)}{Br(D_{sJ}^{+}(2457) \to D_s^{*+}\pi^0)}$ systematics

Error source	systematic uncertainty
Systematics of $D_{sJ}(2457) \to D_s^{*+}\pi^0$ yields	9.4 %
Systematics of $D_{sJ}(2457) \to D_s^{+}\pi^+\pi^-$ yields	1.2 %
π^0 efficiency	4.6 %
γ efficiency	3.3 %
Charged tracking efficiency	2 %
$D_{sJ}(2457) \to D_s^{+}\pi^+\pi^-$ MC statistics	2.2 %
$D_{sJ}(2457) \to D_s^{*+}\pi^0$ MC statistics	3.0 %
$\pi^{\pm}$ momentum cut	3.9 %
Total	13 %

3.15 Masses and natural widths

We measured means both for $D_{sJ}(2317)$ and $D_{sJ}(2457)$ as

- For $D_{sJ}(2317)$:
  - $\Delta M = 348.7 \pm 0.5\ (stat) \pm 0.7\ (syst)$ MeV/c^2
    $M = 2317.2 \pm 0.5\ (stat) \pm 0.9\ (syst)$ MeV/c^2

- For $D_{sJ}(2457)$:
  - $\Delta M = 344.1 \pm 1.3\ (stat)\ 1.1\ (syst)$ MeV/c^2
    $M = 2456.5 \pm 1.3\ (stat)\ 1.3\ (syst)$ MeV/c^2

Table 3.10 is the comparison of $D_sJ(2457)$ mean value in three decay modes. We use $D_sJ(2457)^+ \rightarrow D_s^{*+}\pi^0$ because of lower systematic error. In the $D_{sJ}(2457)^+ \rightarrow D_s^+\gamma$ analysis, E_γ^* cut is very tight for the calibration mode $D_s(2112)^+ \rightarrow D_s^+\gamma$. In the $D_{sJ}(2457)^+ \rightarrow D_s^+\pi^+\pi^-$ analysis, phase space is limited because the $P_{\pi^\pm}^*$ cut criteria is the value optimized for the observation. Then the calibration mode $D_{sJ}(2536)^+ \rightarrow D_s^+\pi^+\pi^-$ is also limited by phase space. Both $D_{sJ}(2457)^+ \rightarrow D_s^+\gamma$ and $D_{sJ}(2457)^+ \rightarrow D_s^+\pi^+\pi^-$ case, the mean difference between calibration mode and PDG value was assigned as photon energy calibration or pion momentum calibration respectively. Then the signal mean was not calibrated by the calibration mode's mean in order to avoid the biased calibration.

Table 3.10: Comparison of $D_{sJ}(2457)$ mean value

Decay mode	$D_{sJ}(2457)$ mean value MeV/c^2
$D_{sJ}(2457)^+ \rightarrow D_s^{*+}\pi^0$	$2456.5 \pm 1.3 \pm 1.1(1.3)$
$D_{sJ}(2457)^+ \rightarrow D_s^+\gamma$	$2459.5 \pm 1.3 \pm 1.9(2.0)$
$D_{sJ}(2457)^+ \rightarrow D_s^+\pi^+\pi^-$	$2459.9 \pm 0.9 \pm 1.5(1.6)$
CLEO($D_{sJ}(2457)^+ \rightarrow D_s^{*+}\pi^0$)	2463 $\pm$ 1.7(stat) $\pm$ 1.0(sys)
BaBar($D_{sJ}(2457)^+ \rightarrow D_s^{*+}\pi^0$)	2457 $\pm$ 1(stat)

Our result is consistent with BaBar but significantly below that of CLEO which will be fitting for row peak.

The observed widths and MC predicted detector resolution are

- For $D_{sJ}(2317)$:
  - Data; $\sigma = 7.6 \pm 0.5$ $(stat) \pm 0.3$ $(syst)$ MeV/c^2
    MC; $\sigma = 7.1 \pm 0.2$ $(stat)$ MeV/c^2

- For $D_{sJ}(2457)$:
  - Data; $\sigma = 5.8 \pm 1.3$ $(stat) \pm 0.4$ $(syst)$ MeV/c^2
    MC; $\sigma = 6.0 \pm 0.2$ $(stat)$ MeV/c^2

The observed width for the $D_{sJ}(2317)$ is 7.6 ± 0.6 MeV/c^2 by adding statistics and systematics uncertainty in quadratic. It is consistent with the experimental resolution from MC of 7.1 ± 0.2 MeV/c^2. The observed width for the $D_{sJ}(2457)$ in $D_{sJ}(2457)^+ \to D_s^{*+}\pi^0$ mode is 5.8 ± 1.4 MeV/c^2 by adding statistics and systematics uncertainty in quadratic. It is consistent with the resolution of 6.0 ± 0.2 MeV/c^2 from MC. We calculate natural widths for the physical region in the 2-dimensional plots of observed width and detector resolution as Figure 3.25, and set the upper limits by taking 90% of natural width. We set upper limits for the natural widths as $\Gamma(D_{sJ}(2317)) \leq 4.6$ MeV/c^2 and $\Gamma(D_{sJ}(2457)) \leq 5.5$ MeV/c^2 (90% C.L.), respectively. The observed width for the $D_{sJ}(2457)^+ \to D_s^+\pi^+\pi^-$ is 2.8 ± 0.9 MeV/c^2 and it is consistent with the detector resolution of 3.6 ± 0.7 MeV/c^2.

3.16 Interpretation

In the $D_{sJ}(2317)$ case, we observed this resonance in the final states of pseudoscalar pair. That means the orbital angular momentum equal to the spin of $D_{sJ}(2317)$ state (L = J). Then the parity which described as P = $(-1)^{L+2}$ to be $(-1)^J$ and it means once we know the spin of new resonance, we can identify the parity. Therefore, most likely S-wave case requires $J^P = 0^+$, P-wave case requires $J^P = 1^-$ and the spin-parity to be the series of $J^P = 0^+$, 1^-, 2^+, 3^- ... in general case. We could not observe this state in $D_s\gamma$ final state which is radiative decay paired with pseudoscalar. That means the states favors spin zero because spin one case can decay into this final state. BELLE observed this state in the decay chain $B \rightarrow \overline{D}D_{sJ}(2317)$ [35]. That means this state can not be higher excited state for the most likely S-wave or P-wave case in the $\overline{D}D_{sJ}(2317)$ system because B and D mesons have spin zero. All results related with this state supports J^P is 0^+ for $D_{sJ}(2317)$.

In the $D_{sJ}(2457)$ case, we observed this second resonance in the final states of vector meson and pseudoscalar pair. That allows $J^P = 1^+$ for most likely S-wave case and $J^P = 0^-$ or 2^- for P-wave case from spin-parity conservation. We could not observe this second state in the final states of $D_s\pi^0$ pseudoscalar pair. This favors the spin-parity to be the series of $J^P = 0^-$, 1^+, 2^-, 3^+ ... because the series which can decay into this state as described before are disfavored. We could observe this second state in $D_s\gamma$ final state which is radiative decay paired with pseudoscalar. This observation ruled out $J^P = 0^\pm$ states for this second resonance because photon polarization can not be cancelled out by both orbital angular momentum due to perpendicular and angular momentum of the paired pseudoscalar. Thus, this second resonance need to be excited state. We observed this second resonance in the final state of $D_s\pi^+\pi^-$ those are three pseudoscalars. In this case with the assumption of spin zero for the initial state, total orbital angular momentum in the final state is required to be zero from angular momentum conservation and the parity to be odd as $(-1)^{L+3}$ = -1. Therefore, parity even state for the spin zero in the initial state is ruled out. BELLE observed this second state in the decay chain of $B \rightarrow \overline{D}D_{sJ}(2457)$ and $D_{sJ}(2457) \rightarrow D_s\gamma$ and the $D_{sJ}(2457)$ helicity distribution are consistent with J = 1 assumption and inconsistent with J =2 assumption [35]. The observation of this second state in B decay with paired by pseudoscalar in final state means that the state can not be higher excited state for the most likely S-wave or P-wave same as $D_{sJ}(2317)$ case. All results related with this second state supports J^P is 1^+ for $D_{sJ}(2457)$.

These can be considered as the doublet of L =1, light quark angular momentum j_q = 1/2 as shown in 1.1. Although these quantum numbers are consistent with the expected broad resonances in potential model but these masses are lower than potential model

prediction [24] as shown in Figure 1.1.
In the L=0 and l_q=1/2 system, mass splitting between $c\bar{s}$ and $u\bar{d}$ are around 100MeV as $M(D_s)$ - $M(D^0)$ = 113.2 $\pm$ 2.0 MeV for 0^- and $M(D_s^*)$ - $M(D^{*0})$ = 110.8 $\pm$ 3.9 MeV for 1^-. Otherwise, in the L=1 and j_q =1/2 system, the mass splitting are $M(D_s(2317))$ - $M(D_0^+)$ = 9 $\pm$ 36 MeV for 0^+ and $M(D_s(2457))$ - $M(D_1^{'})$ = 30 $\pm$ 36 MeV for 1^+. There are inconsistent between (0^-, 1^-) doublet case and (0^+, 1^+) doublet case in j_q =1/2. There are some possible interpretation with chiral symmetry in heavy-light meson system [38].

3.17 Summary

We observed narrow state from $D_s^+\pi^0$ and $D_s^{*+}\pi^0$ decay chain and the observed widths are well agree with detector resolution. The mass are determined as M(D_{sJ}(2317)) to be 2317.2$\pm$0.5($stat$)$\pm$0.9($syst$) and M(D_{sJ}(2457)) to be 2456.5$\pm$1.3($stat$)$\pm$1.3($syst$). We set the upper limit for two natural width as $\Gamma(D_{sJ}(2317)) < 4.6$ MeV/c^2 and $\Gamma(D_{sJ}(2547))$ $<$ 5.5 MeV/c^2 (90% C.L.). We observed the new decay chain $D_s(2457) \rightarrow D_s\pi^+\pi^-$ and obtained first evidence for $D_s(2536) \rightarrow D_s\pi^+\pi^-$. We measured the decay chain $D_s(2457) \rightarrow D_s\gamma$ and set other decay mode's upper limits. Every results is consistent with $D_{sJ}(2317)$ has 0^+ state and $D_{sJ}(2457)$ has 1^+ state.

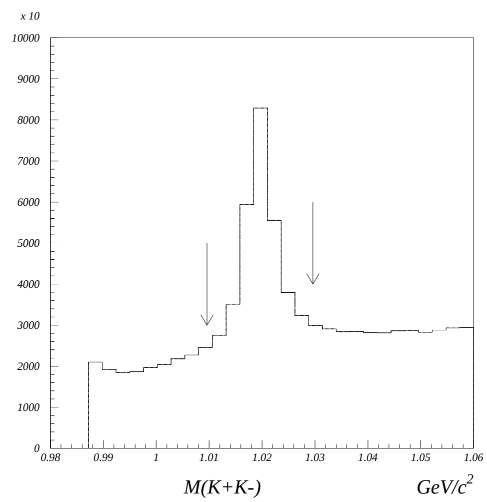

Figure 3.1: The K^+K^- invariant mass distribution in data. The signal region for ϕ is indicated by the arrows.

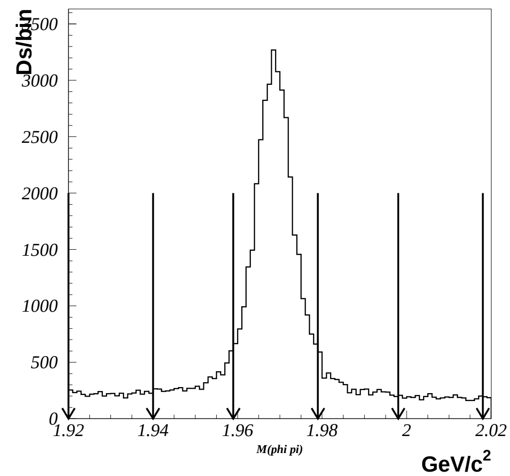

Figure 3.2: The $\phi\pi^+$ invariant mass distribution in data. The D_s^+ signal region and the sideband region are indicated by the arrows.

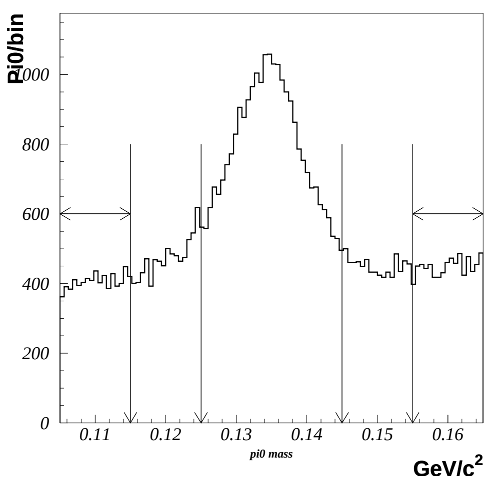

Figure 3.3: The $\gamma\gamma$ invariant mass distribution in data. The signal region for π^0 and sideband region are indicated by the arrows.

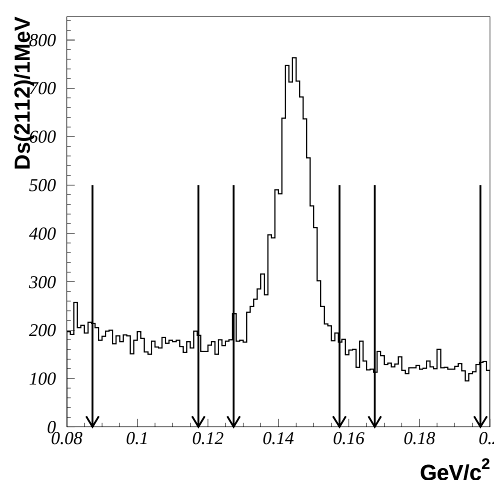

Figure 3.4: The mass difference $M(D_s^+\gamma) - M_{D_s^+}$ distribution in data.

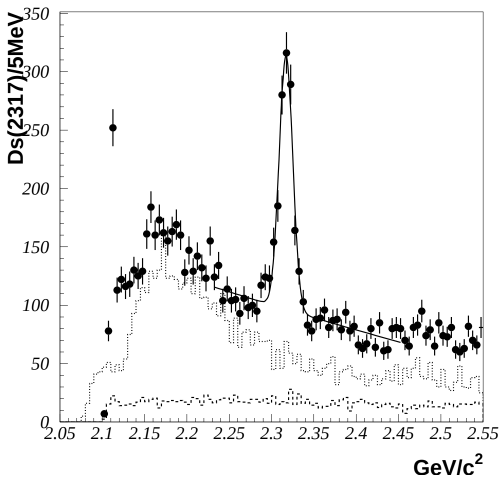

Figure 3.5: The $D_s^+\pi^0$ invariant mass distribution.

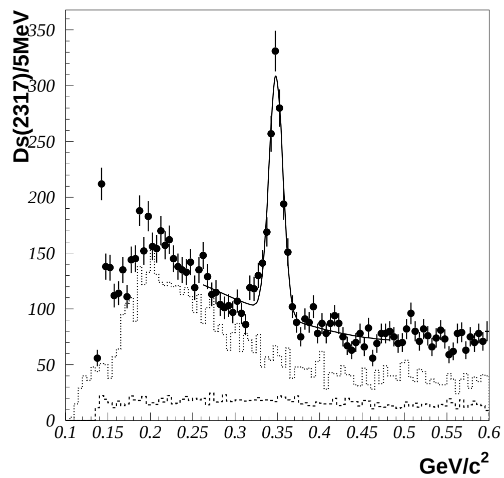

Figure 3.6: The mass difference $M(D_s^+\pi^0) - M_{D_s^+}$ distribution.

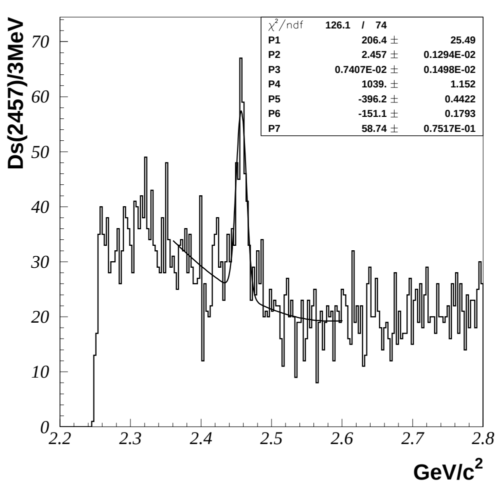

Figure 3.7: The $D_s^{*+}\pi^0$ invariant mass distribution.

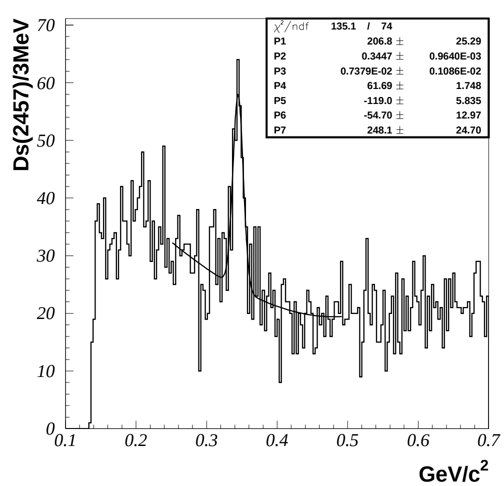

Figure 3.8: The mass difference $M(D_s^{*+}\pi^0) - M_{D_s^{*+}}$ distribution.

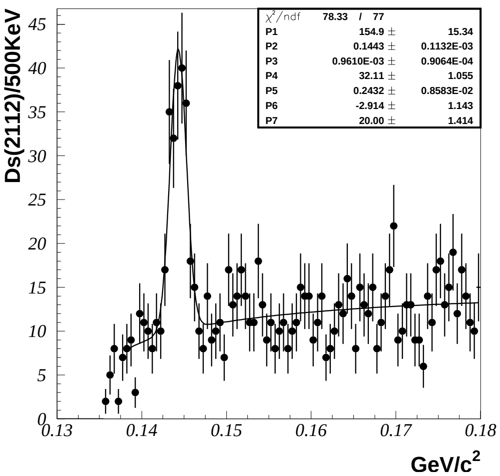

Figure 3.9: The data $M(D_s^+\pi^0) - M_{D_s^+}$ distribution near the D_s^{*+} mass region.

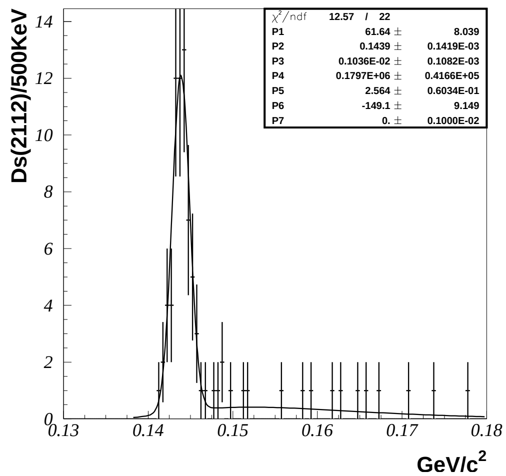

Figure 3.10: The MC $M(D_s^+\pi^0) - M_{D_s^+}$ distribution near the D_s^{*+} mass region.

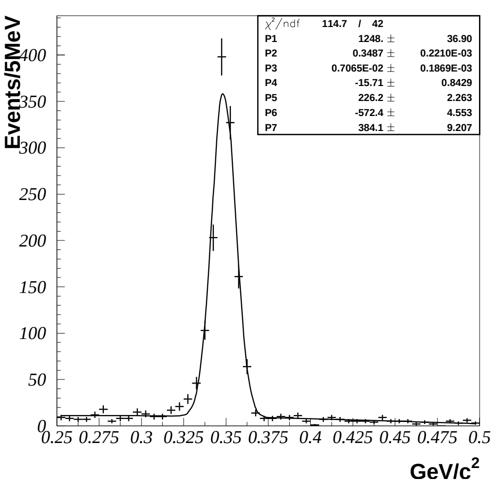

Figure 3.11: The signal $D_s(2317)$ MC $M(D_s^+\pi^0) - M_{D_s^+}$ distribution.

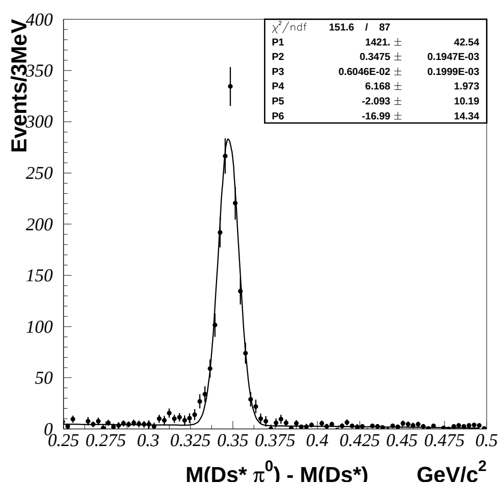

Figure 3.12: The signal $D_s(2457)$ MC $M(D_s^{*+}\pi^0) - M_{D_s^{*+}}$ distribution.

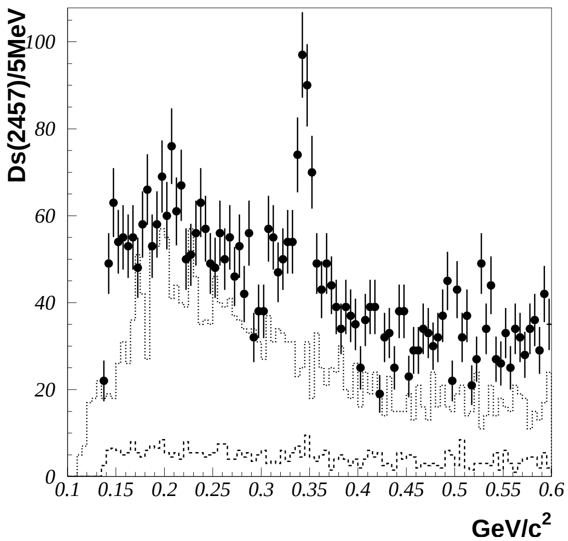

Figure 3.13: The $M(D_s^*\pi^0)-M_{D_s^{*+}}$ distribution. The dark dotted and light dotted histograms are background from D_s^+ sideband and π^0 sideband regions.

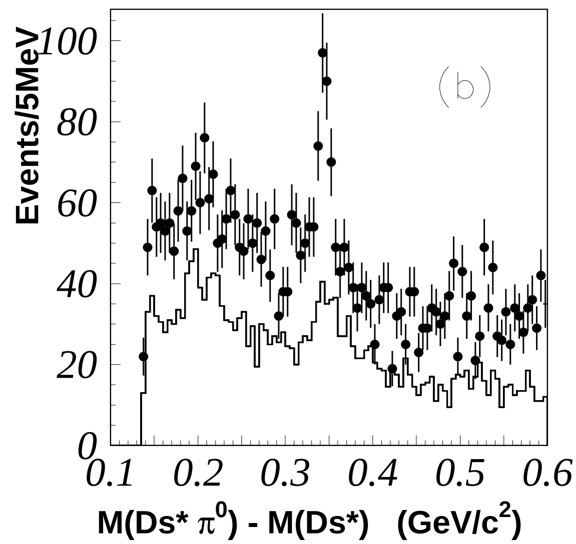

Figure 3.14: The $M(D_s^{*+}\pi^0) - M_{D_s^{*+}}$ distribution from the D_s^* signal and sideband regions.

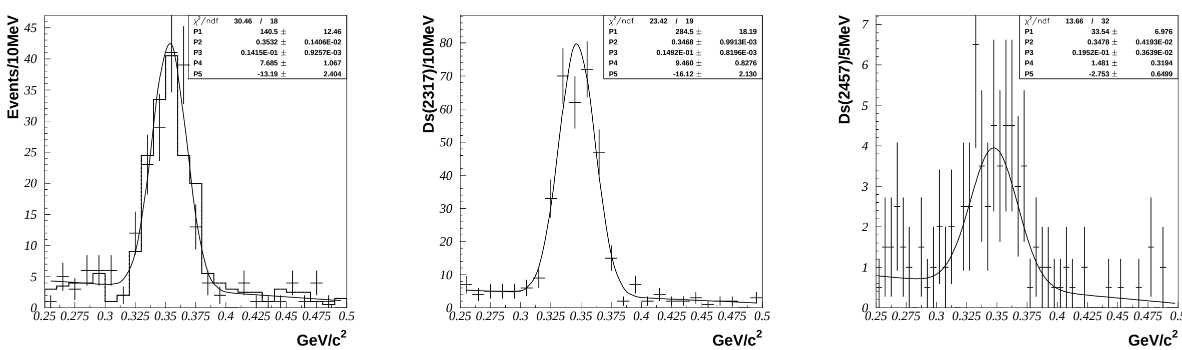

Figure 3.15: The Monte Carlo mass difference distributions of the reflection backgrounds. (a) cross point shows $M(D_s^{*+}\pi^0)-M_{D_s^{*+}}$ distribution from the $D_{sJ}(2317)$ signal MC events (feed-up), and histogram shows $M(D_s^{*+}\pi^0) - M_{D_s^{*+}}$ distribution by using D_s^{*+} sideband from the same $D_{sJ}(2317)$ signal MC events, (b) $M(D_s^+\pi^0) - M_{D_s^+}$ distribution from the $D_{sJ}(2457)$ signal MC events (feed-down), (c) $M(D_s^{*+}\pi^0) - M_{D_s^{*+}}$ distribution from the D_s^{*+} sideband in the $D_{sJ}(2457)$ signal MC (broken combination).

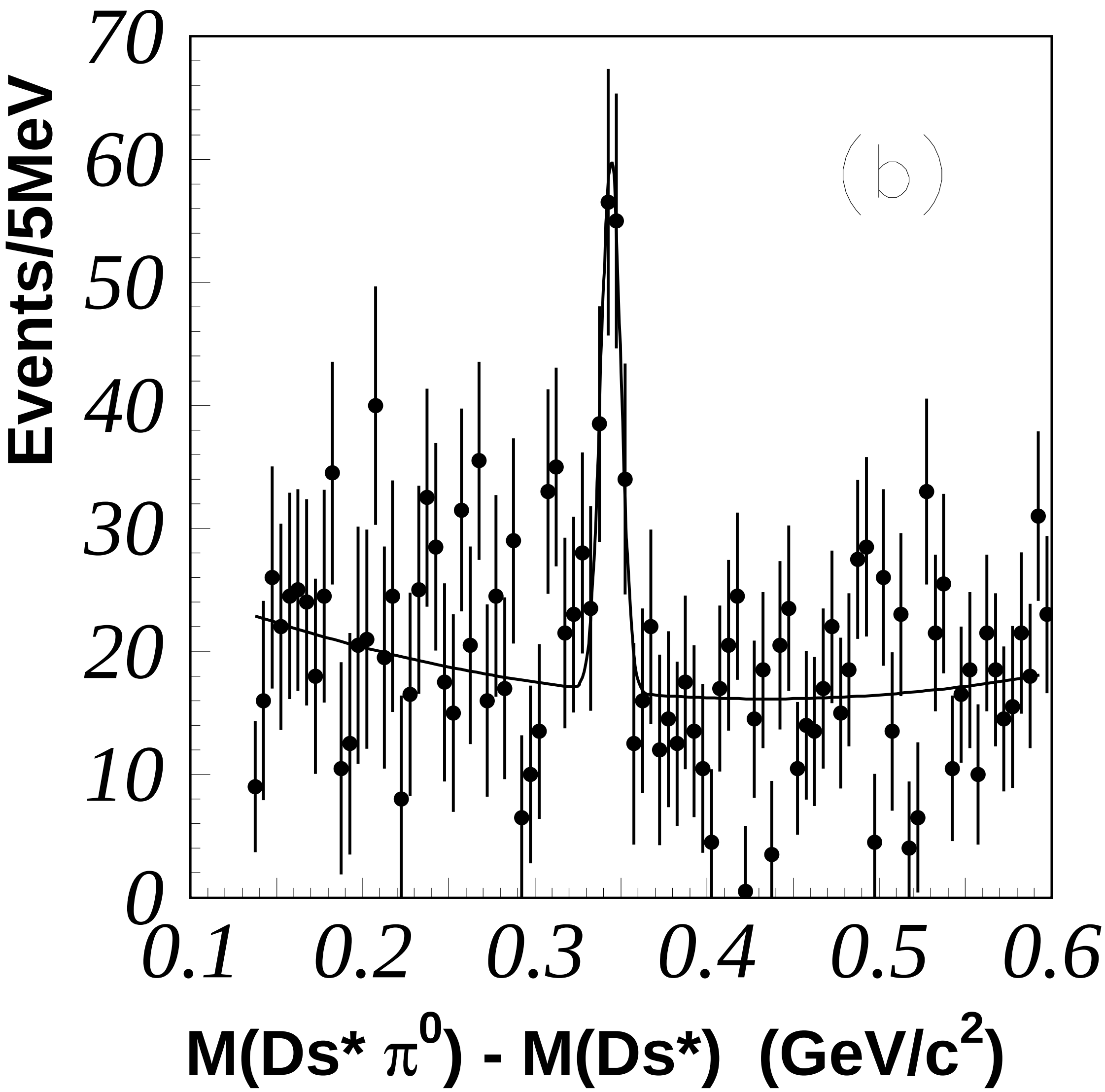

Figure 3.16: The $M(D_s^*\pi^0) - M_{D_s^{*+}}$ distribution after the D_s^* sideband distribution was subtracted from the D_s^* signal distribution bin by bin.

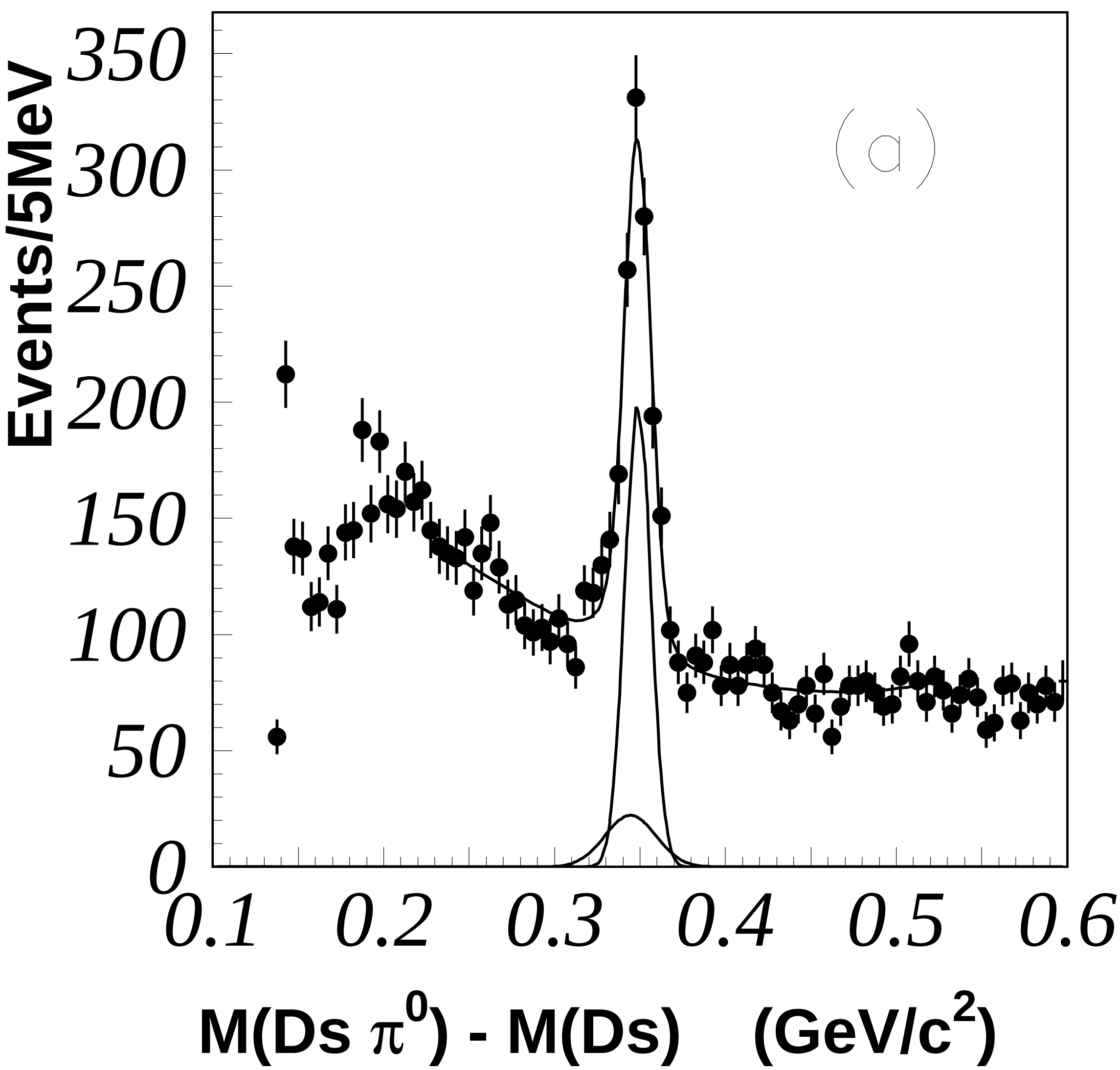

Figure 3.17: The $M(D_s\pi^0) - M_{D_s^+}$ fitting curve by the D_s^* sideband subtraction method; Narrow Gaussian shows true $D_{sJ}(2317)$ signal component and wider shows feed-down component.

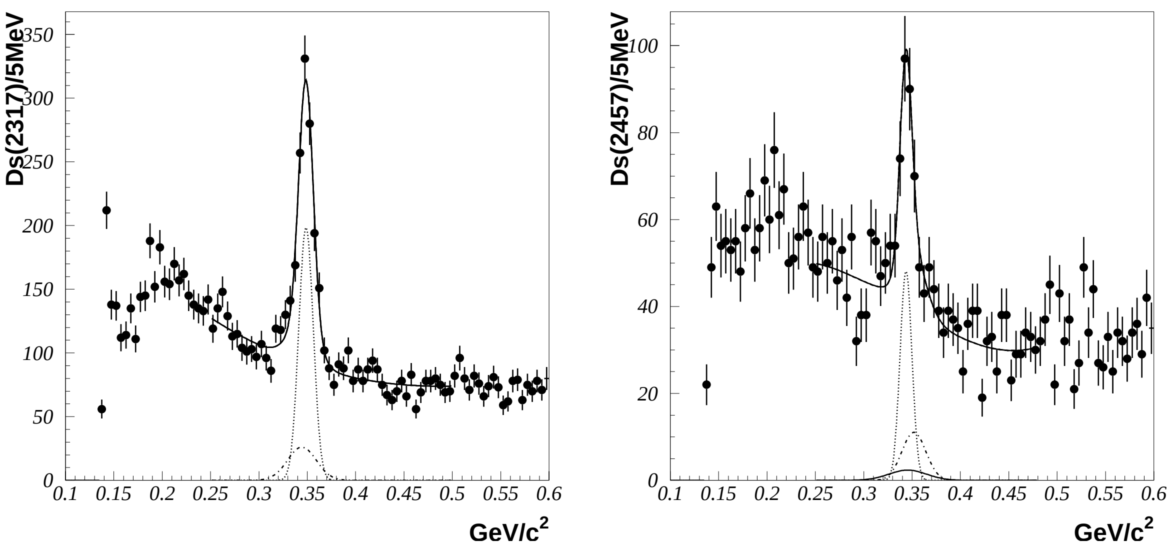

Figure 3.18: Re-fit of mass difference distributions after adding the reflection backgrounds. (a) $M(D_s^+\pi^0) - M_{D_s^+}$ distribution; A narrow peak is true $D_{sJ}(2317)$ signal component. A wider peak is the feed-down component from $D_{sJ}(2457)$. (b) $M(D_s^{*+}\pi^0) - M_{D_s^{*+}}$ distribution for the signal D_s^{*+}; A narrow peak is true $D_{sJ}(2457)$ signal component. Wider peaks correspond to the feed-up (larger one) component from $D_{sJ}(2317)$ and the broken combination (smaller one) component respectively.

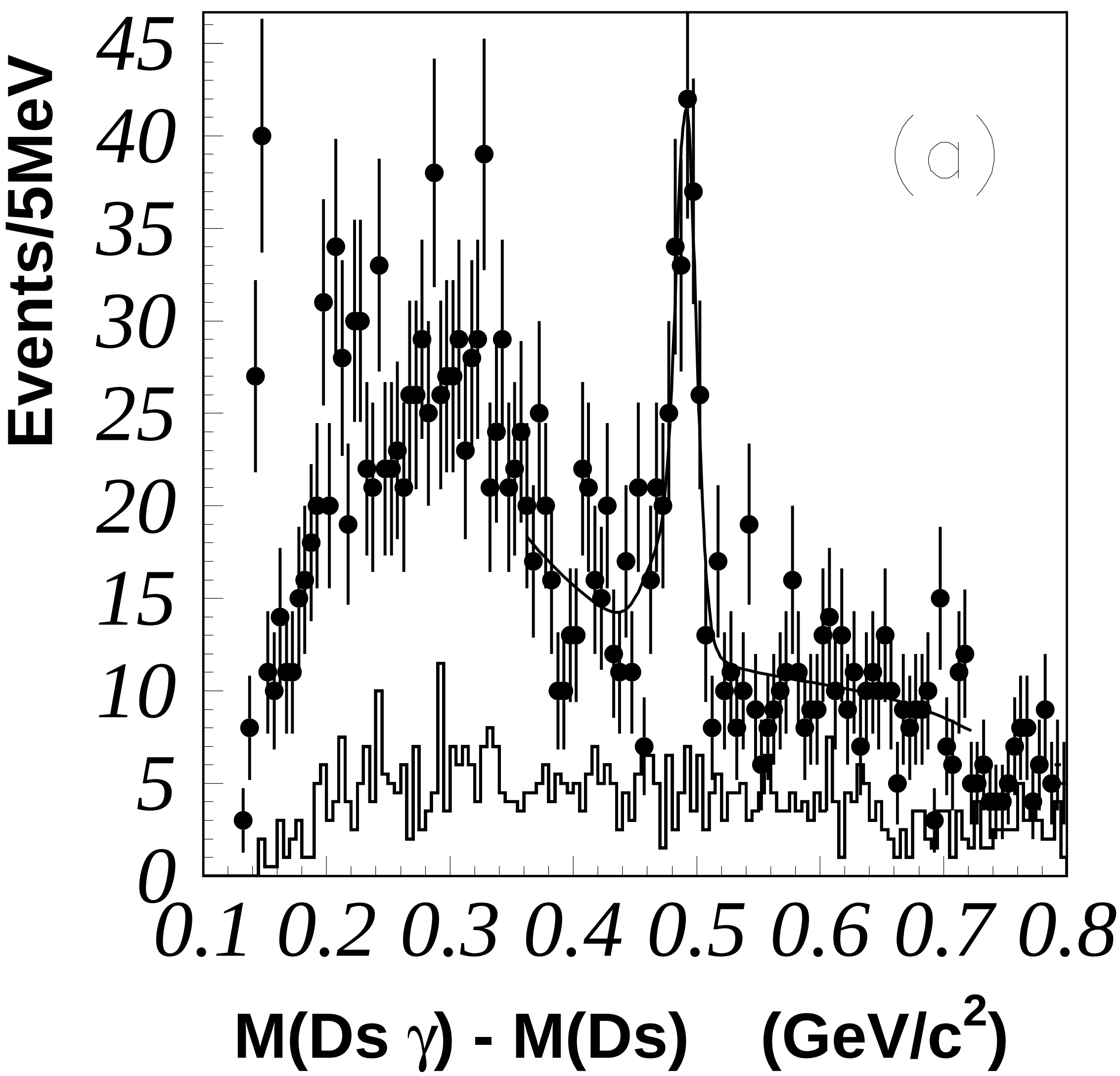

Figure 3.19: The mass difference distribution for $D_s\gamma$ - D_s in data. Histogram is D_s sideband.

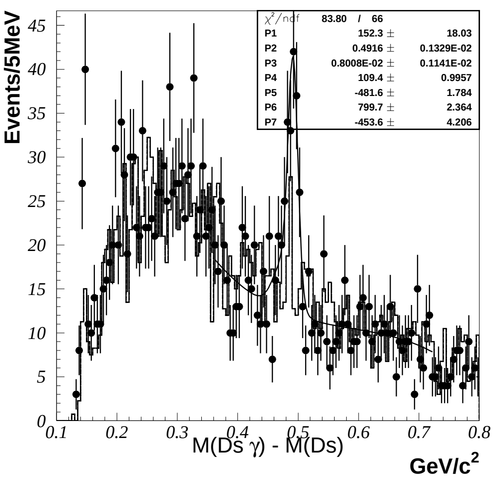

Figure 3.20: The mass difference distribution for $D_s\gamma$ - D_s in data. Histogram is generic charm MC.

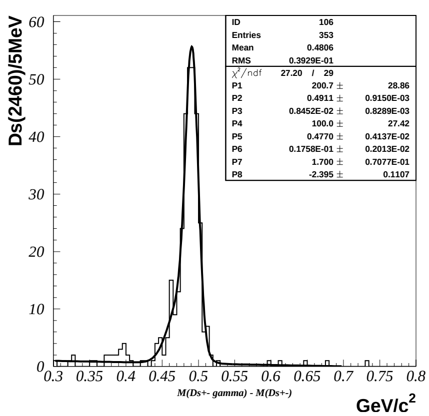

Figure 3.21: The signal $D_s(2457)$ MC mass distribution for $D_s(2457) \to D_s\gamma$.

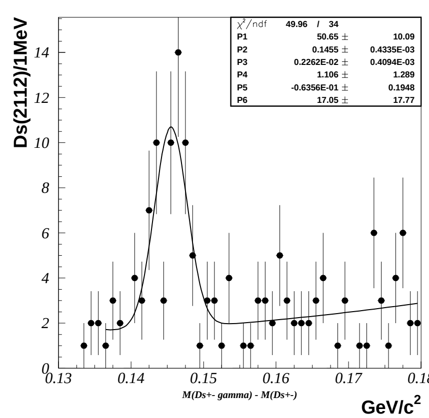

Figure 3.22: The mass distribution for $D_s\gamma$ around $D_s(2112)$ region in data. (Calibration mode)

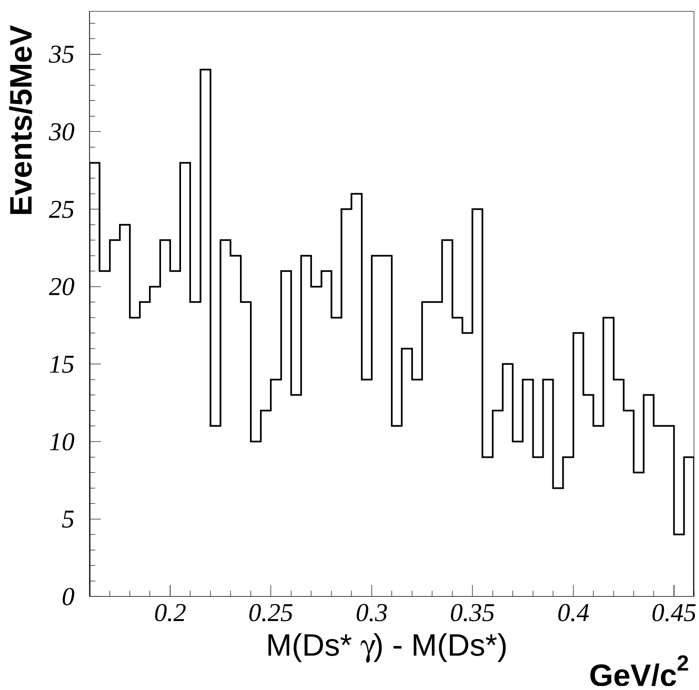

Figure 3.23: The mass difference distribution $D_s^*\gamma$ - D_s^*.

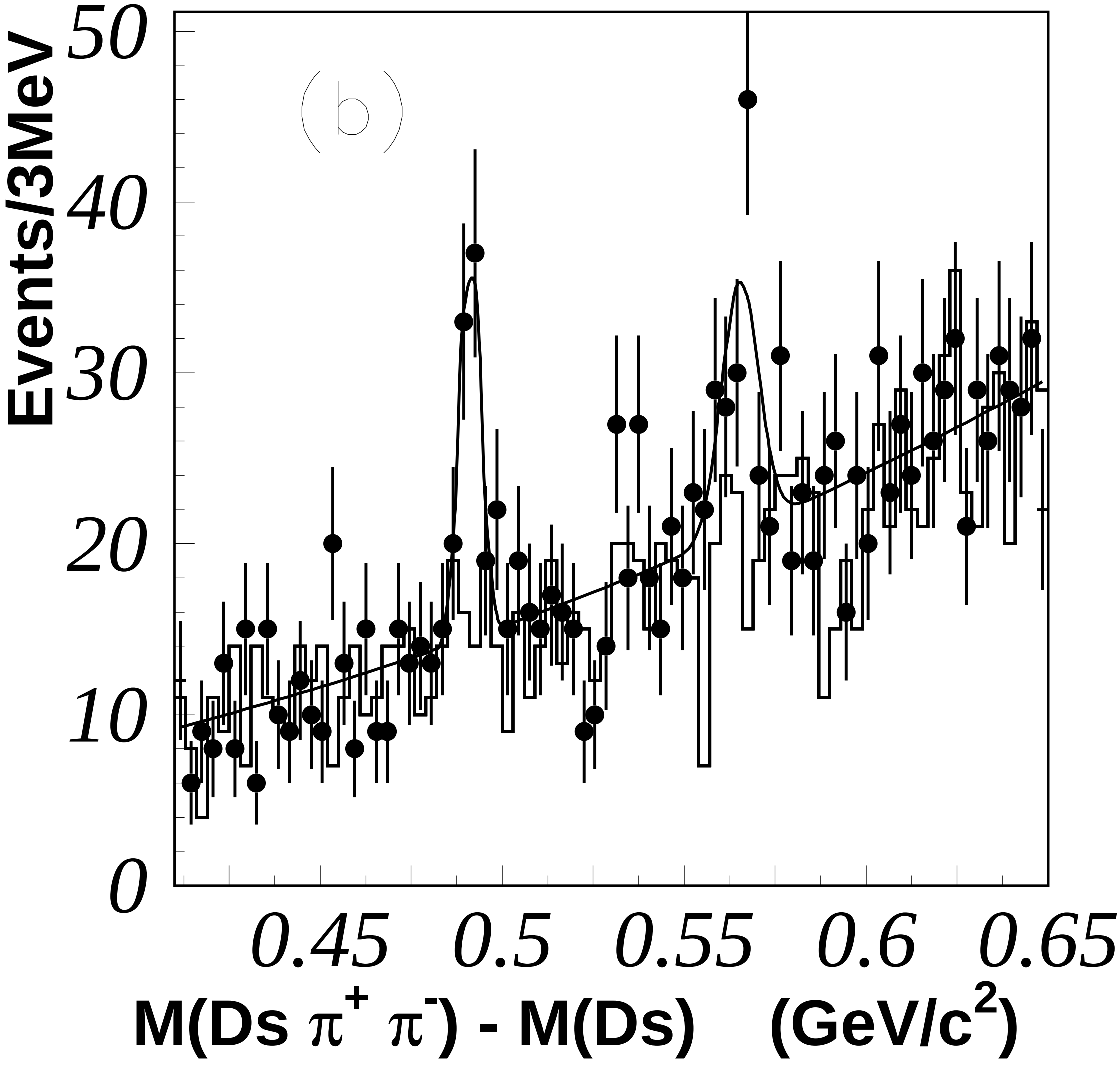

Figure 3.24: The mass difference distribution for $D_s\pi^+\pi^-$. Histogram is D_s sideband.

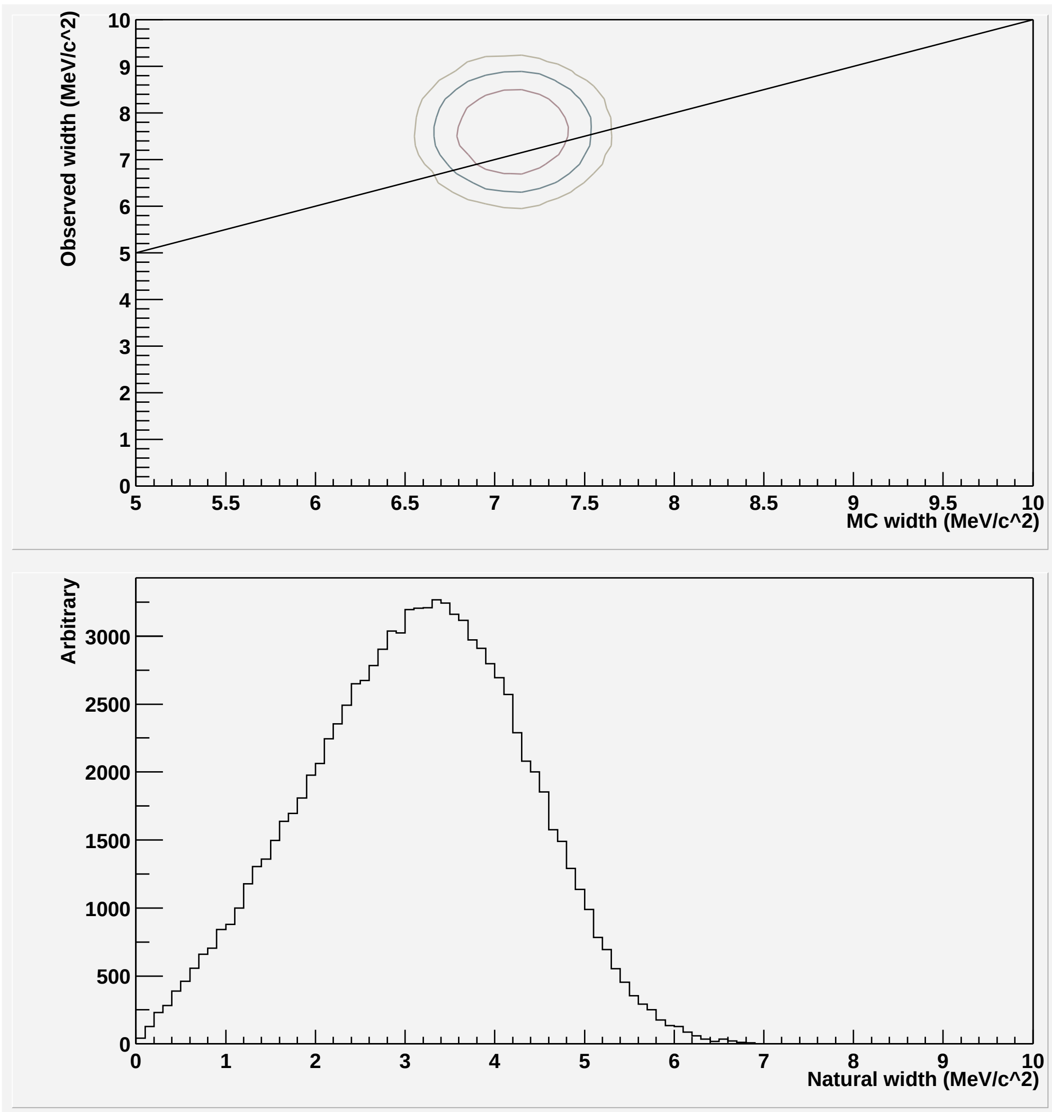

Figure 3.25: Set of upper limit for natural widths of $D_{sJ}(2317)$

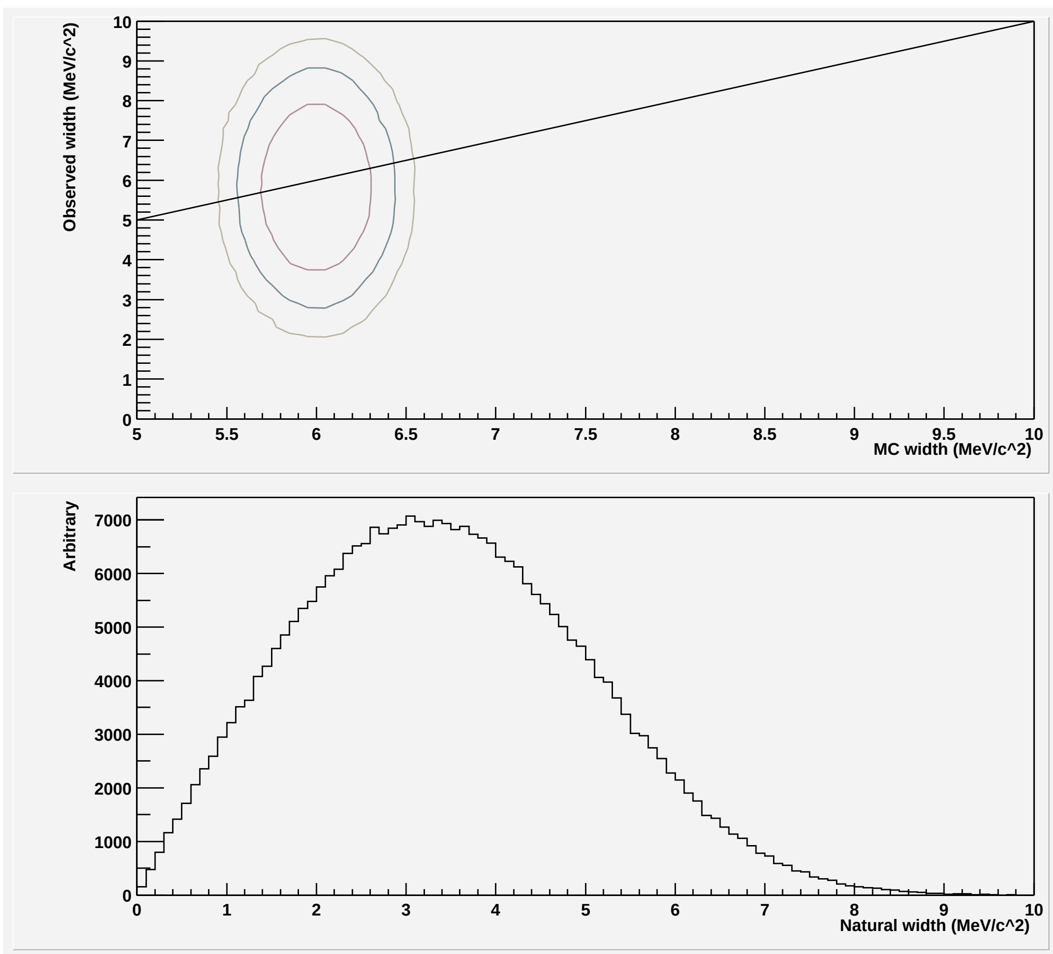

Figure 3.26: Set of upper limit for natural widths of $D_{sJ}(2457)$

Chapter 4

Study of $|V_{ub}|$ with Using D_s Endpoint (Preliminary)

Abstract

We report the study of $b \to u\ D_s^-$ decay using $b \to c\ D_s^-$ endpoint at BELLE experiment. We obtain the CKM matrix elements of $|V_{ub}| = (3.79 \pm 1.67\ (\text{stat}) \pm 0.72\ (\text{syst}) \pm 0.72\ (\text{theo})) \times 10^{-3}$ as preliminary result. This analysis is based on $(152.0 \pm 0.7) \times 10^6\ B\overline{B}$ pairs. collected with the BELLE detector and the KEKB accelerator. (Very Preliminary, BELLE NOTE#690, in progress.)

4.1 Introduction

The matrix element $|V_{ub}|$ in CKM matrix has important roll to test the CP violation in unitarity triangle of CKM mechanism. So far, only lepton endpoint is mainly used for the $|V_{ub}|$ measurement. We use hadronic $b \to u\ D_s^-$ decay and try to determine $|V_{ub}|$ using D_s endpoint. The Fynnman diagram of signal event which contribute this analysis is shown in Figure 4.1.

In this analysis, theory uncertainty is expected to be larger than lepton case due to factorization uncertainty but signal fraction over the endpoint is larger as 38% compared with lepton case of around 10%. We calibrate signal yields with $b \to c\ D_s^-$ yields and then many systematics are cancelled out but the hadronic factorization effects for the estimation of signal fraction over the endpoint will be remained. However, if we can obtain the signal spectrum over the endpoint with high statistics, then it may be possible to reduce the uncertainty from the shape of spectrum. Since the fraction of signal which over

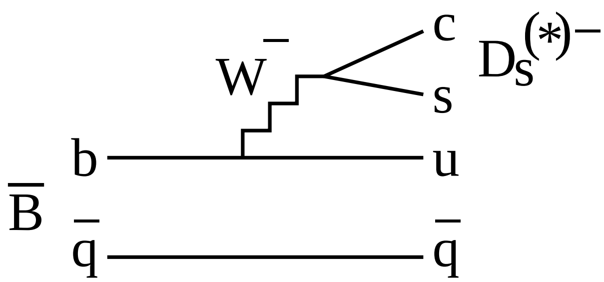

Figure 4.1: $b \to u\ D_s^-$ tree diagram

the kinematic endpoint is larger than lepton, this mode will contribute significantly for the $|V_{ub}|$ determination in future high statistic B factory. This method have continuum background as most dominant background source. It is important to suppress continuum background and we use lepton tagging for the suppression. After the continuum suppression, D_sX_s backgrounds is significant because X_s are light mesons and the D_s can survive the kinematic cut in this inclusive analysis. Lepton tagging contribute also suppression of the D_sX_s backgrounds because the sign of D_s in this background is opposite with signal event as discussed later. This study is the first time of $|V_{ub}|$ using D_s endpoint and the systematic uncertainty sources are quite different with lepton analysis.

4.2 Data Set

We used hadronic events produced in e^+e^- annihilation at the KEKB accelerator and collected with BELLE detector. The data set has an integrated luminosity of 140 fb^{-1} taken at the $\Upsilon(4S)$ resonance (referred as on-resonance data) and around 14 fb^{-1} at a center of mass energy that is 60 MeV below the peak (referred as off-resonance data or continuum data) for continuum background study. The on-resonance data correspond to $(152.0 \pm 0.7)\ \times 10^6\ B\overline{B}$ pairs. We apply cut for event shape variable R_2 as to be less than 0.4 in order to select spherical $B\overline{B}$ events and to suppress jet-like continuum backgrounds events. This variable is like an average of $cos^2\theta$ for all combination of particles in the event and it have close to one for jet-like events and have close to zero for spherical events as shown in Figure 4.2 and Figure 4.3.

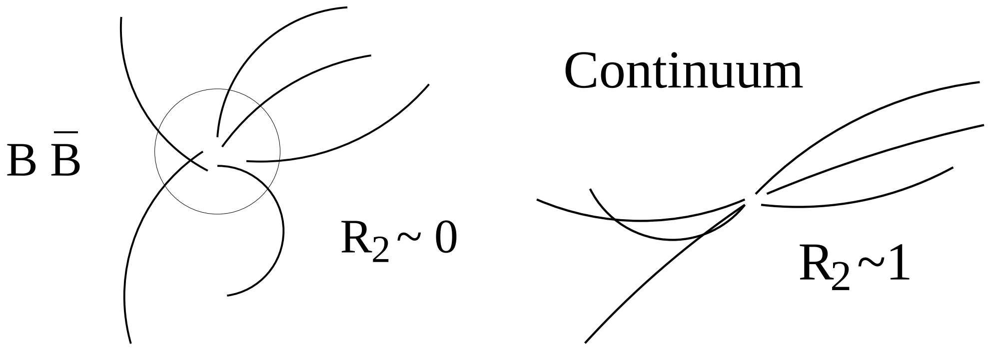

Figure 4.2: Event topology

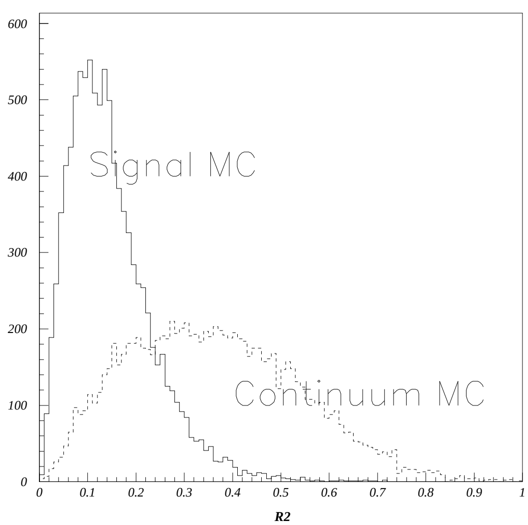

Figure 4.3: R_2 distribution

4.3 Reconstruction of ϕ and D_s

We use $D_s^+ \to \phi\pi^+$ and $\phi \to K^+K^-$ decay channels for D_s^+ reconstruction mode because it has the best combination of detection efficiency, branching ratio, and background suppression. In order to identify kaons or pions, we apply a K/π mode dependent require-

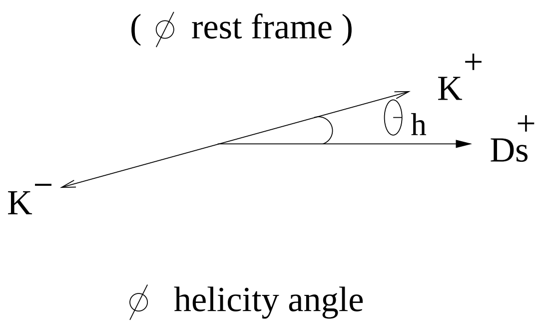

Figure 4.4: ϕ helicity definition

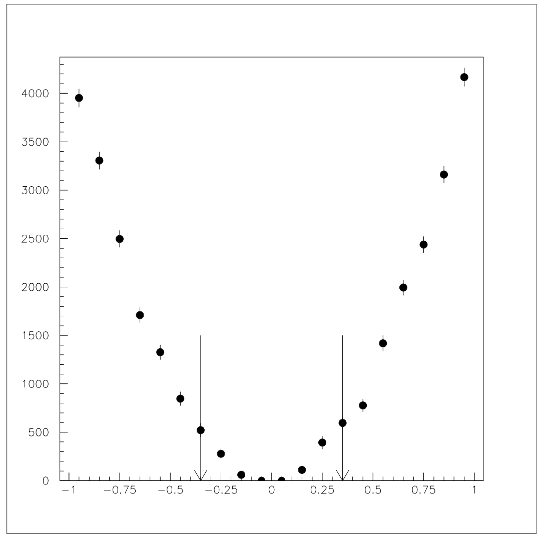

Figure 4.5: ϕ helicity distribution in data and cut value shown by arrow

ment on the ratio $L_K/(L_K + L_\pi)$ or $L_\pi/(L_K + L_\pi)$. We form K^+K^- invariant mass by requiring one track has $L_K/(L_K + L_\pi) > 0.5$ and another track has $L_K/(L_K + L_\pi) > 0.2$. Figure 4.11 shows the K^+K^- invariant mass distribution. We apply impact-parameter cuts of d_r and d_z which are defined as the length between interaction point and the closest point of the charged track in r and z direction respectively, we use cut values to be $|d_r|$ less than 0.5 cm and $|d_z|$ less than 2 cm. The ϕ candidates must satisfy $M_{K^+K^-}$ to be within 10 MeV/c^2 ($\sim 2.5\Gamma$) of the nominal ϕ mass. We use the ϕ helicity angle θ_ϕ which is defined as the angle between the direction of the K^+ and the $D_s^\pm$ in the ϕ rest frame as shown in Figure 4.4. The signal follows a $cos^2\theta_H$ distribution as shown in Figure 4.5 while the background is flat in $cos\theta_H$ distribution. We require $|cos\theta_H|$ to be greater than 0.35 for signal selection. We reconstruct D_s^+ candidate in $D_s^+ \to \phi\pi^+$ decay by combining pion and ϕ candidates. We require $L_\pi/(L_K + L_\pi) > 0.1$ for the pion candidates. The invariant mass distribution for $\phi\pi^+$ is shown in Figure 4.12. We optimized cut values for particle identifications, helicity angle cut and R_2 cut with making F.O.M. variable maximum where the variable was defined as MC signal yields divided by uncertainty of MC continuum background yields. The distributions of the variables in each cut dependence are shown in Figure 4.3, Figure 4.7, Figure 4.8, Figure 4.9 and Figure 4.10.

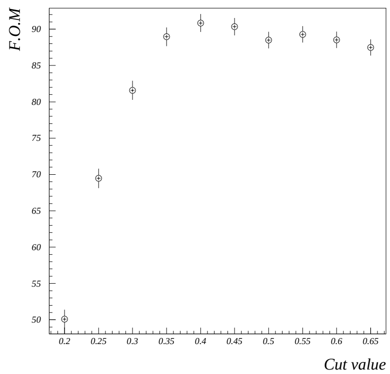

Figure 4.6: F.O.M. for R_2

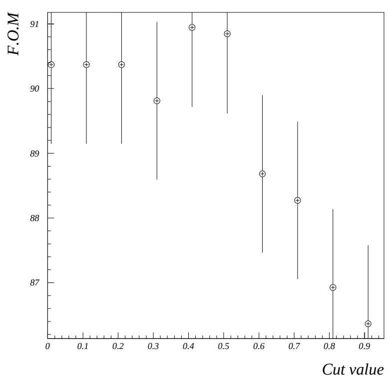

Figure 4.7: F.O.M. for one KID

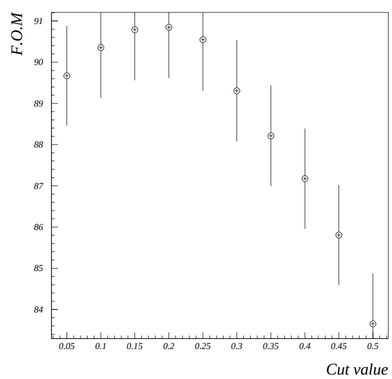

Figure 4.8: F.O.M. for another KID

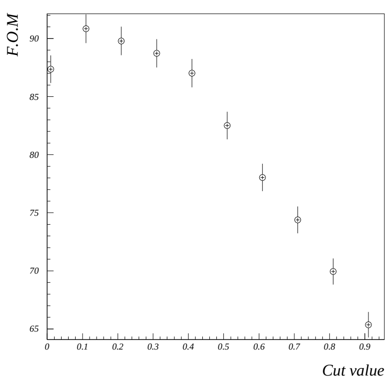

Figure 4.9: F.O.M. for πID

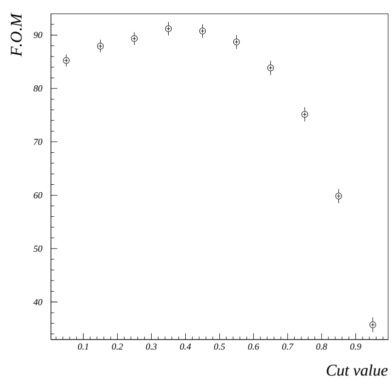

Figure 4.10: F.O.M. for helicity angle

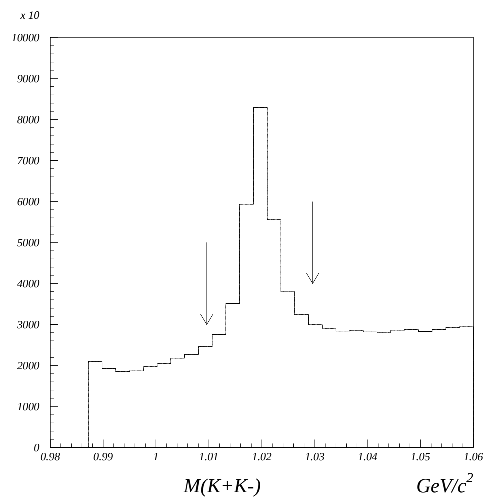

Figure 4.11: The K^+K^- invariant mass distribution in data. The signal region for ϕ is indicated by the arrows.

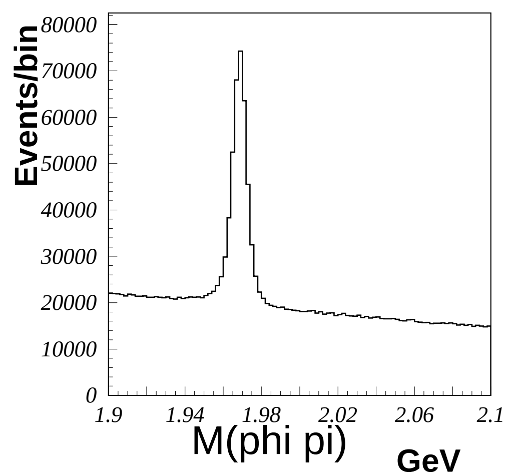

Figure 4.12: The $\phi\pi^+$ invariant mass distribution in data.

4.4 Background estimation

4.4.1 $B \to D_s X_c$ Background

The fraction for $B \to D_s X_c$ background events is $\sim O(10^2)$ order of the signal fraction for $B \to D_s X_u$ events. We use the $b \to c$ D_s^- kinematic endpoint to distinguish this background events from signal events. Then the maximum momentum of D_s^+ in $B \to D_s\ X_c$ decay is calculated with assuming $B \to D\ D_s$ mode and obtained as 1.99 GeV/c in B meson rest frame with a correction by B meson velocity $\beta_B = 0.064$. We estimate the experimental resolution for $D_s^\pm$ momentum around this region using Monte Carlo events. We obtained our momentum resolution as 23 MeV/c from MC as Figure 4.13.

The signal fraction of momentum cut dependence from theory [8] are listed on Table 4.1. We apply a momentum cut as greater than 2.1 GeV/c and assign this background systematic as 3.9% with using MC background yields and the branching fraction ratio $Br(b \to uD_s)/Br(b \to cD_s)$ from the theoretical prediction [8]. In future it is better to study this systematic uncertainty with using data of control sample.

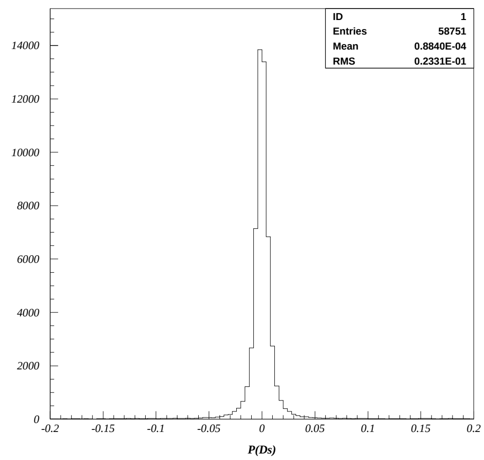

Figure 4.13: The D_s momentum difference between generated momentum and reconstructed momentum in Monte Carlo. (Using the scaled momentum which corresponds that x = 1 is around 5 GeV/c.)

4.4.2 Continuum Background

This is a dominant background source in this inclusive study. The typical diagram can be described as Figure 4.14.

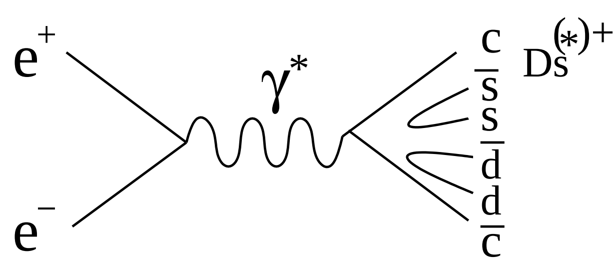

Figure 4.14: Typical $e^+e^- \rightarrow c\bar{c}$ continuum events diagram which produce D_s.

This background has jet-like event topology and we use the event shape variable R_2 that is using 2nd moment of Fox Walfram variable with scaling by 0th moment [16] and it shows that jet-like events have the variable as close to be 1 and spherical events have

$P^*_{D_s}$ cut	≥2.0 GeV/c	≥2.05 GeV/c	≥2.1 GeV/c
Signal D_s fraction (theory)	82%	74%	63%
Signal D_s^* fraction (theory)	44%	34%	25%
Total $\overline{b} \to D_s^{(*)}\overline{u}$ fraction (theory)	57%	48%	38%
$\#(B \to D_s\ X_c)/\#(B \to D_s\ X_u)$	(128 ± 13)%	(43 ± 8)%	(1.6 ± 3.9)%

Table 4.1: Theory prediction of signal fraction [8] and MC study of background fraction with momentum dependence.

the variable as close to be 0. We apply this variable is less than 0.4 from Monte Carlo F.O.M. study. We use an off-resonance data that is taken 60MeV below the on-resonance data for this continuum background subtraction. We use lepton tagging method for the purpose of further suppression of this background as described in next paragraph.

Lepton tagging We use lepton tagging method in order to suppress continuum backgrounds. This method is also strong method for $B \to D_s X_s$ background suppression due to the requirement of opposite charged sign as described in next section. We require that the lepton have opposite charged sign with $D_s^{\pm}$ because the tagged primary $D_s^{\pm}$ in signal side B meson and high momentum primary lepton in other B meson have opposite charged sign in $B\overline{B}$ pair production. This method is tagging for other B meson in $B\overline{B}$ system and it means signal $B \to D_s\ X_u$ model independent. The requirement of opposite charged sign can reduce many uncertainties which come from other backgrounds that have wrong sign $D_s^{\mp}$. We require lepton ID is greater than 0.99 and the cut value are shown in the Figure 4.15 and Figure 4.16 with separating both electron ID and muon ID.

We require the angle cuts between $D_s^{\pm}$ and lepton as -0.6 $\leq \cos\theta^*_{l-D_s} \leq$ 0.9 for the continuum suppression because the backgrounds have peak in opposite direction with signal D_s in continuum jet-like events. We require the momentum of lepton in $\Upsilon(4S)$ c.m. frame as greater than 1.4 GeV/c to select primary high momentum lepton. The momentum cut and angle cut values are determined by F.O.M. analyses. Then the F.O.M. variable are defined as S/σ_{qq} where S is signal MC yields and σ_{qq} is an error of yields in $c\overline{c}$ continuum MC because we have only 1/10 of off-resonance data compared with on-resonance data and then the error of continuum background is dominant when we use off-resonance data for continuum background subtraction from data. The Figure 4.17, Figure 4.18 and Figure 4.19 are results of F.O.M. analyses.

The momentum distribution of lepton are shown in Figure 4.20 for both signal Monte Carlo and off-resonance data. The angle between $D_s^{\pm}$ and $l^{\mp}$ are shown in Figure 4.21 for both Signal Monte Carlo and continuum Monte Carlo. We can suppress continuum back-

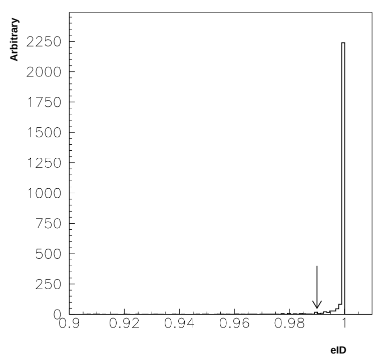

Figure 4.15: Electron ID distribution in data and cut value shown by arrow

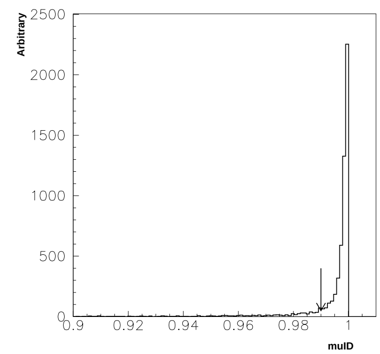

Figure 4.16: Muon ID distribution in data and cut value shown by arrow

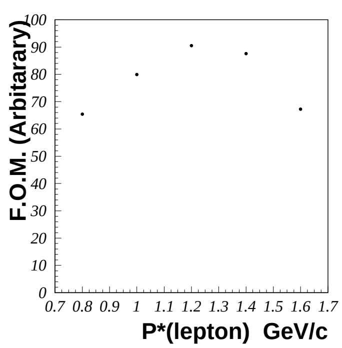

Figure 4.17: F.O.M. distribution for momentum cut

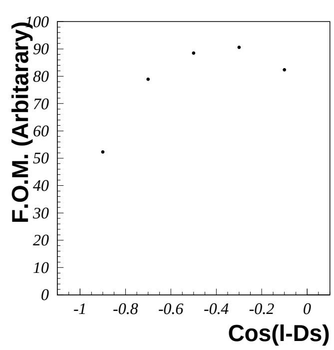

Figure 4.18: F.O.M. distribution for lower angle cut

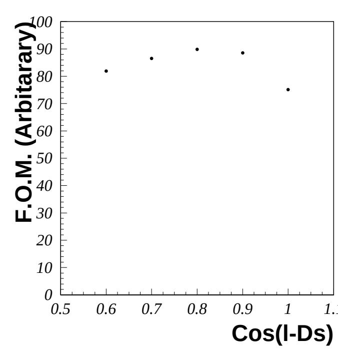

Figure 4.19: F.O.M. distribution for higher angle cut

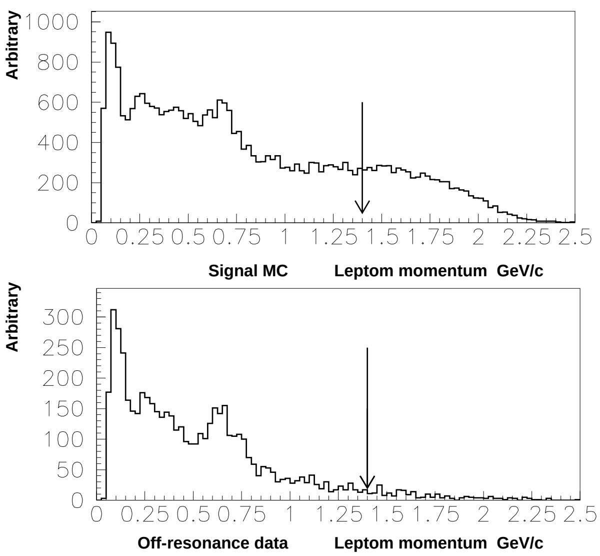

Figure 4.20: Momentum distribution for tagging lepton with cut value shown by arrows: Upper plot is for signal MC and lower plots is for off-resonance data.

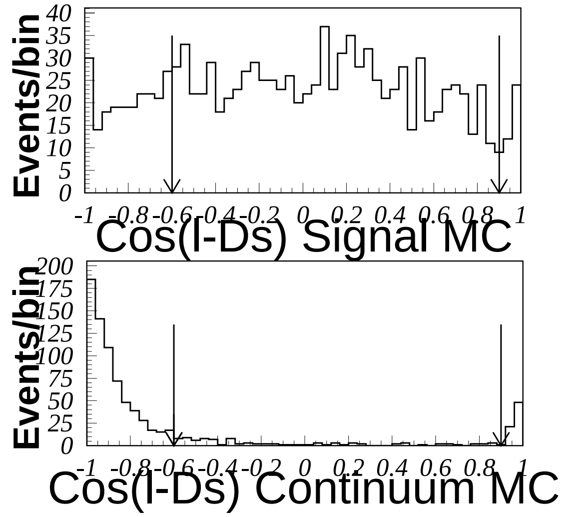

Figure 4.21: Angle between $D_s^{\pm}$ and $l^{\mp}$ with cut values shown by arrows: Upper plot is for signal MC and lower plots is for off-resonance MC.

ground strongly by this variable. The signal efficiency using the events of $B^0 \to D_s^+\ a_1^-$ Monte Carlo is $(5.1 \pm 0.3)\%$, otherwise continuum backgrounds MC events suppressed by the efficiency of $(0.13 \pm 0.02)\%$. We can obtain the advantage for signal significance.

4.4.3 $B \to D_s X_s$ Background

This $B \to D_s X_s$ events survive in the signal region over the $b \to c\ D_s^-$ kinematic endpoint. The only measurement in $B \to D_s X_s$ is BELLE's $Br(B^0 \to D_s^- K^+) = (2.93 \pm 0.55 \pm 0.79) \times 10^{-5}$ [39]. This $B \to D_s X_s$ background source are expected as W-exchange, annihilation or Final State Interaction (FSI), while the signal $B^0 \to D_s^+ \pi^-$ is tree diagram and color favored of spectator process in Cabibbo suppressed decay. Systematic uncertainty studies for each diagram are described in next paragraphs respectively.

***W* exchange** This W-exchange diagram can be described with two case as Cabbibo enhanced shown in Figure 4.22 and Cabbibo suppressed shown in Figure 4.23. Both case occur only in neutral B decay, requirement of $s\bar{s}$ pair production and color suppressed.

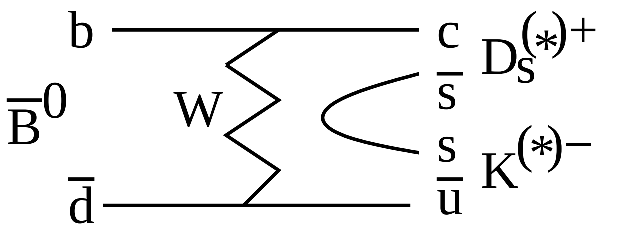

Figure 4.22: Cabbibo enhanced W-exchange diagram in $B \to D_s X_s$ decay.

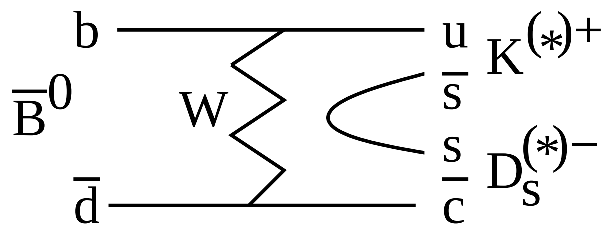

Figure 4.23: Cabbibo suppressed W-exchange diagram in $B \to D_s X_s$ decay.

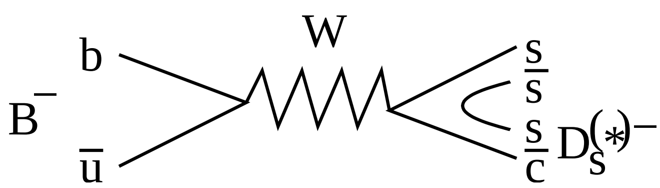

Figure 4.24: Annihilation

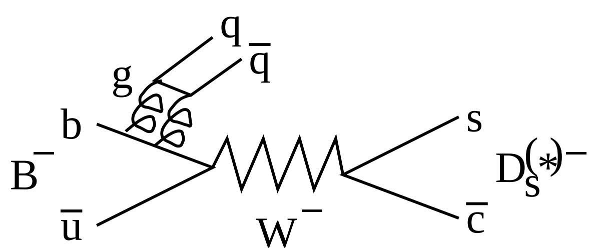

Figure 4.25: Annihilation via two gluons

Cabbibo enhanced In the Cabbibo enhanced case, the sign of $D_s^{\pm}$ is opposite with true signal sign and the efficiency using $B^0 \to D_s^- K^+$ MC is 0.45%. This is almost 1/10 of signal efficiency of 5.1% using $B^0 \to D_s^+ a_1^-$ MC. After using mixing parameter of $\chi_d =$ 0.18 correction, the effective efficiency is estimated as (1 - 0.18) $\times$ 1/10 + 0.18 = 26% of signal efficiency. In total, they are 0.5 (neutral B) $\times$ 0.3 ($s\overline{s}$ pair production) [8] $\times$ 1/3 (color suppressed) $\times$ 26% = 1.3% and negligible.

Cabbibo suppressed In the Cabbibo suppressed case, the sign of $D_s^{\pm}$ is same with true signal sign but theory prediction is less than $O(10^{-4})$ of spectator process [8]. It is safely negligible for the uncertainty from this backgrounds.

Annihilation This annihilation diagram shown in Figure 4.24 occurs with requirement of $s\overline{s}$ pair production and color suppressed. Theory prediction is of the order or smaller than $\sim 3 \times O(10^{-2})$ of spectator process [8]. We assign 3% systematics for this background uncertainty conservatively.

Annihilation via 2 gluons Annihilation via 2 gluons shown in Figure 4.25 occurs in Coupling with 2 gluons and negligible.

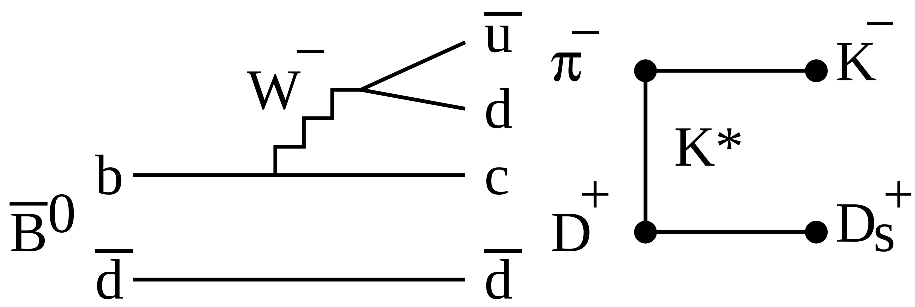

Figure 4.26: Example of Final State Interaction

Final State Interaction There is a possibility of background from D_s X_s events through Final State Interaction (FSI). For example, $K^{(*)}$ exchange between D and π in supper allowed decay chain $\overline{B} \to D^+\pi^-$ described as Figure 4.26. Other possibility of Final State Interaction which contains D_s are that occurs through the $d\overline{d}$ annihilation into $s\overline{s}$ in the same $\overline{B} \to D^+\pi^-$ supper allowed mode.

The sign of $D_s^{\pm}$ is wrong sign through this FSI because the D_s have the same sign with the lower vertex's wrong sign charm. From BELLE measurement for $Br(B^0 \to D_s^- K^+) = (2.93 \pm 0.55 \pm 0.79) \times 10^{-5}$ and theory prediction [8] for the inclusive branching fraction of signal events as $Br(B^0 \to D_s^+ X_u) \sim 6.8 \times 10^{-4}$, the branching fraction ratio $Br(B^0 \to D_s^- K^+)/Br(B^0 \to D_s^+ X_u)$ can be calculated as $\sim$ (4.3 $\pm$ 1.4)%. Then wrong sign D_s^+ efficiency is estimated as $\sim 1/10$ compared with true sign from MC study. With using mixing factor $\chi_d = 0.18$, effective wrong sign efficiency is estimated as (1 -0.18) $\times$ 1/10 + 0.18 = 26%. After including mixing wrong tag correction, fraction of this mode in signal events is calculated as (4.3 + 1.4)% $\times$ 0.26 = 1.5%, that is using one sigma conservative value for background yield. This need be multiplied by the factor of $Br(B^0 \to D_s^{\pm} X_s)/Br(B^0 \to D_s^- K^+)$ because there are many other mode in X_s such as K^0, K^{*0}, $K^{*\pm}$, K_1, K_1^*, K_2, ... those are not yet measured. We temporally multiple by factor 10 for this effects because so far only $B^0 \to D_s^- K^+$ mode is measured in total $B^0 \to D_s^{\pm} X_s$. Here note is that higher spin kaon are suppressed through the events such as most likely S-wave or P-wave in this B decay because B and D_s has spin zero and angular momentum conservation requires that spin of kaon are less than one in these S-wave or P-wave case. Then total systematic uncertainty is 15% (Very preliminary).

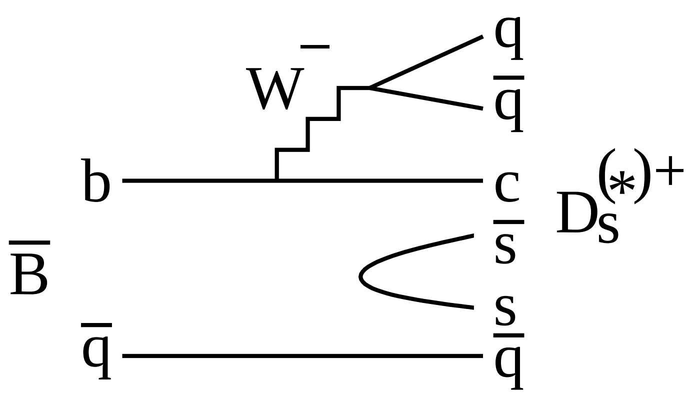

Figure 4.27: Lower vertex

4.4.4 $s\overline{s}$ hopping

The D_s produced with $s\overline{s}$ hopping in lower vertex as shown in Figure 4.27 has wrong sign D_s and the efficiency is $\sim 10\%$ compared with signal efficiency. Since we measure $|V_{ub}|/|V_{cb}|$ with calibrating $\overline{b} \to \overline{u}\ D_s^+$ yields by $\overline{b} \to \overline{c}\ D_s^+$ yields in order to take ratio of spectator process, we need estimate this background effects in both $\overline{b} \to \overline{u}\ D_s^+$ yields and $\overline{b} \to \overline{c}\ D_s^+$ yields. In signal $\overline{b} \to \overline{u}\ D_s^+$ yields case, $s\overline{s}$ hopping background fraction is $\sim 2 \times O(10)$ of signal [8]. Then, this process occurs through multi-body decay and that mean this D_s^+ momentum is soft as that only 0.5% of $\overline{b} \to \overline{c}\ D_s^+$ can survive above 2.0 GeV/c in momentum. Then the systematic is calculated as $20 \times 0.5\% \times 26\% = 2.6\%$. This is including wrong tag fraction of lepton tagging. In the $\overline{b} \to \overline{c}\ D_s^+$ calibration case, CLEO shows that lower vertex fraction is $(0.17 \pm 0.08)\%$ compared with tree diagram. After wrong tag correction, it changes as $(4.4 \pm 2.1)\%$. We use conservatively 6.5% for this systematics uncertainty without correction for yields.

4.5 Momentum spectrum

We estimated the kinematic endpoint of D_s momentum in $b \to c\ D_s$ transition with using $B^0 \to D_s^+ D^-$ decay and then we correct with B meson velocity $\beta_B = 0.064$. We obtained the D_s momentum to be 1.99 GeV/c in the B meson rest frame as the kinematic limit. The endpoint of $b \to u\ D_s$ transition is estimated as 2.46 GeV/c in the B meson rest frame with using $B^0 \to D_s^+ \pi^-$ decay chain. We define the signal region as greater than 2.1 GeV/c and less than 2.5 GeV/c. The momentum spectrum based on 140 fb^{-1}

	On-resonance	Off-resonance
D_s Yields	43.5 ± 9.8	0.45 ± 1.27
After scaling	-	5.4 ± 15.1

Table 4.2: D_s yields both for on-resonance data and off-resonance data

on-resonance data is showed as Figure 4.28.

4.6 Signal yields extraction

We obtained signal yields after continuum subtraction as 38.2 ± 18.0 (stat.) events with subtracting off-resonance yields from on-resonance yields after scaling for off-resonance yields as shown in Table 4.2. Then we used on-resonance/off-resonance scale factor as 11.9 ± 0.2 which is the ratio of D_s yields without lepton tagging. in momentum region of greater than 2.5 GeV/c where only continuum is produced region.

4.7 Extraction of $|V_{ub}|/|V_{cb}|$

The fraction $\Gamma(\overline{b} \to \overline{q}\ D_s^+) = \Gamma(\overline{b} \to \overline{c}\ D_s^+) + \Gamma(\overline{b} \to \overline{u}\ D_s^+)$ and the fraction $\Gamma(\overline{b} \to \overline{q}\ D_s^{*+}) = \Gamma(\overline{b} \to \overline{c}\ D_s^{*+}) + \Gamma(\overline{b} \to \overline{u}\ D_s^{*+})$ can be written respectively [8] as

$$\Gamma^{(0)}(\overline{b} \to D_s^+ \overline{q}) =$$

$$\frac{G_F^2}{8\pi}|V_{qb}^* V_{cs}|^2 f_{D_s}^2 \frac{(m_b^2 - m_q^2)^2}{m_b^2}(1 - \frac{m_{D_s}^2(m_b^2 + m_q^2)}{(m_b^2 - m_q^2)^2})\frac{\sqrt{\{m_b^2 - (m_{D_s} + m_q)^2\}\{m_b^2 - (m_{D_s} - m_q)^2\}}}{2m_b} a_1^2$$

$$\Gamma^{(0)}(\overline{b} \to D_s^{*+} \overline{q}) =$$

$$\frac{G_F^2}{8\pi}|V_{qb}^* V_{cs}|^2 f_{D_s^*}^2 \frac{(m_b^2 - m_q^2)^2}{m_b^2}(1 + \frac{m_{D_s^*}^2(m_b^2 + m_q^2 - 2m_{D_s^*}^2)}{(m_b^2 - m_q^2)^2})\frac{\sqrt{\{m_b^2 - (m_{D_s^*} + m_q)^2\}\{m_b^2 - (m_{D_s^*} - m_q)^2\}}}{2m_b} a_1^2$$

With using each total fraction of $\Gamma(B^0 \to D_s^+ X_u)$ and $\Gamma(B^0 \to D_s^+ X_c)$, we can write the branching fraction ratio as

$$\frac{\Gamma(B^0 \to D_s^+ X_u)}{\Gamma(B^0 \to D_s^+ X_c)} = (|V_{ub}/V_{cb}|)^2 \times f_{PS}$$

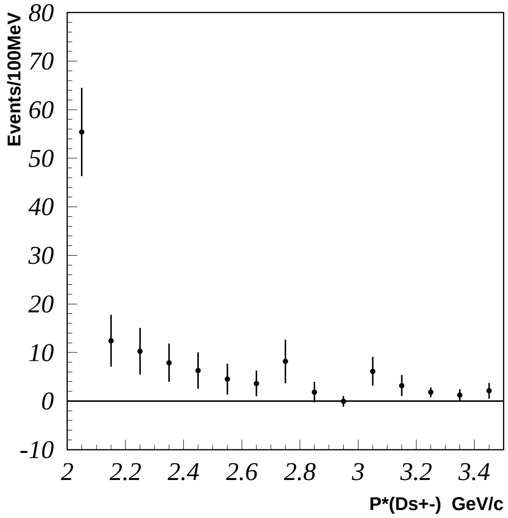

Figure 4.28: Momentum spectrum before off-resonance background subtraction (Very preliminary)

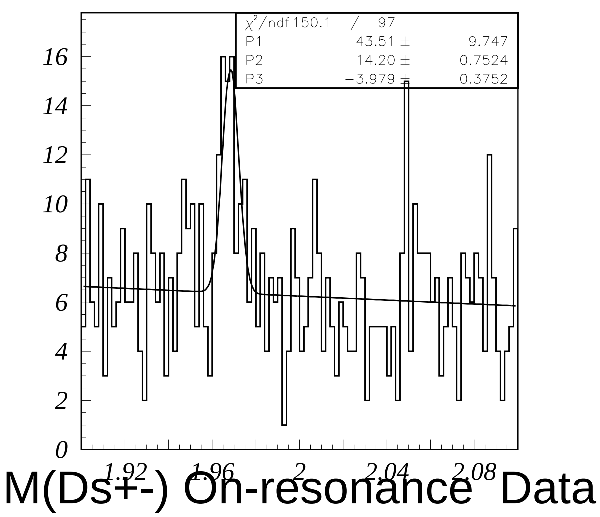

Figure 4.29: $M_{\phi\pi}$ distribution in signal region for on-resonance data (Very preliminary)

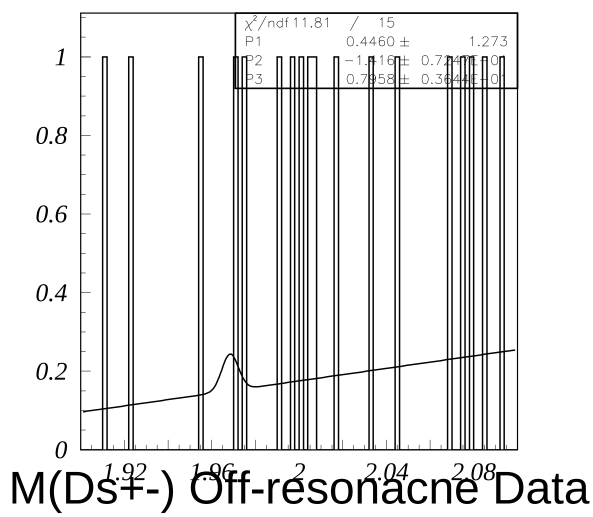

Figure 4.30: $M_{\phi\pi}$ distribution in signal region for off-resonance data (Very preliminary)

$(D_s^+ \to \phi\ \pi^+)$	Eff.(recon.)	Eff.(tagging)
$B \to D_s^+\ X_c$	$(25.8 \pm 0.1)\%$	$(5.4 \pm 0.1)\%$
$B^0 \to D_s^+\ a_1^-$	$(30.4 \pm 0.3)\%$	$(5.3 \pm 0.2)\%$
$B^0 \to D_s^+\ \pi^-$	$(28.7 \pm 0.3)\%$	$(5.4 \pm 0.2)\%$
$B^+ \to D_s^+\ a_1^0$	$(31.0 \pm 0.8)\%$	$(5.8 \pm 0.6)\%$

Table 4.3: Efficiencies for each modes

where f_{PS} is phase space ratio of $\Gamma(B^0 \to D_s^+ X_u)$ to $\Gamma(B^0 \to D_s^+ X_c)$. From theoretical prediction [8] as $\Gamma(B^0 \to D_s^+ X_c) \sim 8.0\%$ and $\Gamma(B^0 \to D_s^+ X_u) \sim 6.8 \times 10^{-4}$ where radiative correction effects is taken into account, we obtain the f_{PS} is 1.33. Then newly found D_{sJ} effects are not taken into accounts. In the 2.1 GeV/c momentum cut, the fraction of over-endpoint described as f_{end} is predicted to be 0.38 with using 300MeV/c for Fermi motion P_F and 10MeV/c^2 for spectator quark mass [8]. We can extract $|V_{ub}/V_{cb}|$ from following equation,

$$\frac{N_{b \to u D_s(2.1GeV/c \leq\ P^*\ < 2.5GeV/c)}}{N_{b \to c D_s(all\ P^*)}} \times \frac{\epsilon_{b \to c}}{\epsilon_{b \to u}} = |\frac{V_{ub}}{V_{cb}}|^2 \times f_{PS} \times f_{end}$$

where $N_{b \to q D_s}$ are event yields for each $b \to q$ case in respective momentum region described in the equation. The variables of $\epsilon_{b \to c}$ and $\epsilon_{b \to u}$ in the equation means efficiencies that are reconstruction efficiency times tagging efficiency for each $b \to q$ case respectively. Here note is that efficiency of reconstruction for inclusive events has only difference of momentum dependence. In the tagging efficiency case, due to that tagging are applied for other B, the efficiency is signal model independent and also it can be cancelled out between signal mode efficiency and calibration mode efficiency. Table 4.3 is MC study for some signal modes and background mode.

We calculated the signal model uncertainty as 5.6% from difference between $B^0 \to D_s^+\ a_1^-$ efficiency and $B^0 \to D_s^+\ \pi^-$ efficiency. Then the $B^0 \to D_s^+\ a_1^-$ is more spherical due to large multiplicity and $B^0 \to D_s^+\ \pi^-$ is less spherical compared with other modes in inclusive $B \to D_s$ decay. The efficiency difference mainly origin from event topology R_2 cut. From the $D_s^+ \to \phi\ \pi^+$ signal yields of 38.2 ± 18.0 (stat.) events, we obtained very preliminary $|V_{ub}|/|V_{cb}|$ value as

$$|\frac{V_{ub}}{V_{cb}}|^2 = 0.00758 \pm 0.0036\ (stat.)$$

$$|\frac{V_{ub}}{V_{cb}}| = 0.0871 \pm 0.041\ (stat.)$$

W-exchange	Negligible
Annihilation	3%
Lower vertex in $B \to D_s\ X_u$ yields	2.6%
Lower vertex in $B \to D_s\ X_c$ yields	6.5%
Signal model dependence	5.6%
$b \to c$ spillover	3.9%
P.D.G. $\|V_{cb}\|$	4.9%
FSI's X_s background	15%
Total systematics	19%

Table 4.4: Summary of systematics for $|V_{ub}|$ extraction

and then $|V_{ub}| = (3.59 \pm 1.69_{stat} \pm 0.72_{syst} \pm 0.72_{theo}) \times 10^{-3}$ (Very preliminary) where we used PDG value $|V_{cb}| = (41.2 \pm 2.0) \times 10^{-3}$.

4.8 Theoretical uncertainty

With the cut of momentum is grater than 2.05 GeV/c, theoretical prediction [8] for the uncertainty

$$\frac{\sigma(|V_{ub}|)}{|V_{ub}|} = 0.17$$

With the change of momentum cut value as 2.05 GeV/c to 2.10 GeV/c, the yields prediction decrease $\sim 20\%$ and we add this effects for theoretical uncertainty with increasing ~ 1.1 times. Therefore we use theoretical uncertainty as 19% (Very preliminary).

4.9 Systematics summary

Taking ratio of $(b \to u\ D_s^-)/(b \to c\ D_s^-)$ can cancel out major uncertainties such as $\mathrm{Br}(D_s^{\pm} \longrightarrow \phi\pi^{\pm}) = 25\%$ and hadronic factorization. The total systematics are summarized in next Table 4.4 (Very Preliminary). Some systematics source will be updated in near future for aiming journal publication.

4.10 Summary

We studied the decay chain $b \to u\ D_s$ and tested extraction of $|V_{ub}|$ in the hadronic decay. We obtain $|V_{ub}| = (3.79 \pm 1.67\ (\text{stat}) \pm 0.72\ (\text{syst}) \pm 0.72\ (\text{theo})) \times 10^{-3}$ as preliminary results. This provides $|V_{ub}|$ with different systematic source. This result will be updated with using more than $300 fb^{-1}$ data for the claiming the evidence. (Very preliminary)

Chapter 5

Conclusion

Measurement of the D_{sJ} resonance properties

We observed narrow state from $D_s^+\pi^0$ and $D_s^{*+}\pi^0$ decay chain and the observed widths are well agree with detector resolution. The mass are determined as M($D_{sJ}(2317)$) to be $2317.2\pm0.5(stat)\pm0.9(syst)$ and M($D_{sJ}(2457)$) to be $2456.5\pm1.3(stat)\pm1.3(syst)$. We set the upper limit for two natural width as $\Gamma(D_{sJ}(2317)) < 4.6$ MeV/c^2 and $\Gamma(D_{sJ}(2547)) <$ 5.5 MeV/c^2 (90% C.L.). We has the first observation of the new decay chain $D_s(2457) \rightarrow D_s\pi^+\pi^-$ and obtained first evidence for $D_s(2536) \rightarrow D_s\pi^+\pi^-$. We measured the decay chain $D_s(2457) \rightarrow D_s\gamma$ and set other decay mode's upper limits. Every results is consistent with $D_{sJ}(2317)$ has 0^+ state and $D_{sJ}(2457)$ has 1^+ state. These can be considered the doublet of L =1, light quark angular momentum $j_q = 1/2$. These masses are lower than potential model prediction [24].

Study of $|V_{ub}|$ with D_s Endpoint (Very preliminary)

We studied the decay chain $b \rightarrow u\ D_s$ and tested the $|V_{ub}|$ extraction in the hadronic decay. We obtained $|V_{ub}| = (3.79 \pm 1.67\ \text{(stat)} \pm 0.72\ \text{(syst)} \pm 0.72\ \text{(theo)}) \times 10^{-3}$ as preliminary results. This provides $|V_{ub}|$ with different systematic. This result will be updated with using more than $300 fb^{-1}$ data for the claiming the evidence and with more precise systematic uncertainty studies especially for $D_s\ X_s$ background in near future. This result is consistent with other study using lepton endpoint. (Very preliminary in progress)

Appendix A

Study of $B \to D_s^{(*)\pm}$ Inclusive Decay (Belle Note#557)

Abstract

We measured the branching fraction of the inclusive $B \to D_s^{\pm} X$ decay and the inclusive $B \to D_s^{*\pm} X$ decay as $Br(B \to D_s^{\pm} X) = (11.7 \pm 0.1 \pm 1.0 \pm 2.9)\%$, and the branching fraction of the inclusive $Br(B \to D_s^{*\pm} X) = (7.07 \pm 0.19 \pm 0.71 \pm 1.77)\%$, where the first error is statistical, the second error is systematics and the third error is a uncertainty from $D_s^{\pm} \to \phi\pi^{\pm}$ branching fraction. We used 78.1 fb^{-1} $\Upsilon(4S)$ on-resonance data and 8.8 fb^{-1} $\Upsilon(4S)$ off-resonance data which is accumulated with the BELLE detector and the KEKB accelerator. (Preliminary, belle note#557)

A.1 Introduction

The large sample of B meson enables us a precise measurement of Kobayashi Maskawa [1] matrix elements. The external spectator B meson decay diagram leads to a $D_s^{(*)\pm}$ in the final state where the W^+ materializes as a $c\overline{s}$. This mode make it possible to measure the $D_s^{(*)\pm}$ from $b \to u\ D_s^{(*)-}$ transition with using kinematic limit for the $D_s^{(*)\pm}$ background from $b \to c\ D_s^{(*)-}$ transition. In this paper, we report the measurements of branching fractions for $B \to D_s^{\pm} X$ decay and $B \to D_s^{*\pm} X$ decay and those momentum spectrum.

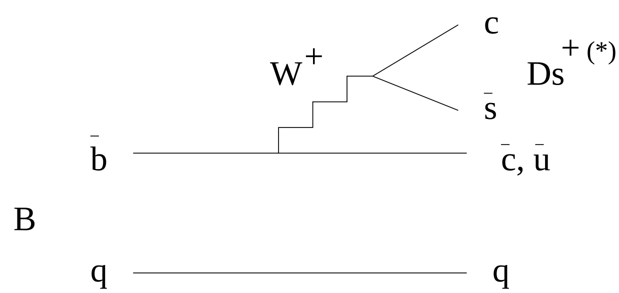

Figure A.1: Feynman diagram which contributes to this analysis

A.2 Data Set

We used the data selected from hadronic events produced in e^+e^- annihilation at the KEKB accelerator [34] and BELLE detector [33]. The data set consists of an integrated luminosity of 78.8 fb^{-1} collected at the $\Upsilon(4S)$ resonance (referred as on-resonance data) and 8.8 fb^{-1} at a center of mass energy just below the threshold for producing $B\overline{B}$ mesons (referred as off-resonance data or continuum data). The on-resonance data correspond to (85.0 $\pm$ 0.5) $\times 10^6$ $B\overline{B}$ pairs.

A.3 The Inclusive $B \to D_s^{\pm}$ Branching Fraction

The on-resonance data consist of $B\overline{B}$ events and continuum events. Therefore, in order to measure the $Br(B \to D_s^{\pm} X)$ and the $Br(B \to D_s^{*\pm} X)$, we need to subtract the continuum contribution from the total yield of $D_s^\pm$ mesons in the on-resonance data. We use off-resonance data for the estimation of continuum contribution.

We use the $D_s^\pm \rightarrow \phi\pi^\pm$ and $\phi \rightarrow K^+K^-$ decay channel for the inclusive $B \rightarrow D_s^\pm X$ decay because it has the best combination of detection efficiency, branching ratio, and background suppression. We required the K^+K^- invariant mass to be within 10MeV of the ϕ nominal mass and particle identification for the two kaons as having at least one KID is greater than 0.5 and another KID is greater than 0.2. We use the ϕ helicity angle θ_H which is the angle between the direction of the K^+ and the $D_s^\pm$ in the ϕ rest frame. The signal follows a $cos^2\theta_H$ distribution while the background is flat in $cos^2\theta_H$. We required $|cos\theta_H|$ is greater than 0.35 which eliminates 35% of the background events while retaining 95% of signal events. We require the pion identification is greater than 0.1 for the pion from the $D_s^\pm \rightarrow \phi\pi^\pm$ decay chain.

In order to compare the yield of $D_s^\pm$ from on-resonance to the yield of $D_s^\pm$ from off-resonance, we use the scaled $D_s^\pm$ momentum x, which is defined as $x \equiv P^*_{D_s^\pm}/P_{max}$ and $P_{max} = \sqrt{E_{beam}^2 - M_{D_s^\pm}^2}$, where $P^*_{D_s^\pm}$ is the momentum of the $D_s^\pm$ in the $\Upsilon(4S)$ rest frame, E_{beam} is 5.29 GeV for on-resonance data, and 5.26 GeV for off-resonance data. The endpoint of $D_s^\pm$ mesons produced from B decay is $x = 0.50$ with the correction for the B meson velocity ($\beta_B = 0.06$). We define the signal region as being $0 \leq x < 0.5$.

We extract the yield of $D_s^\pm$ as a function of momentum by fitting the $\phi\pi$ invariant mass plots for each bin of x. The bin size of 0.02 is an order of magnitude larger than the resolution of x. We use a double Gaussian as the signal shape and a linear function as the combinatorial background shape. We fixed the mean, widths and ratio of the two areas of the double Gaussian with the values from fitting with $M_{\phi\pi}$ distribution correspond to the all $D_s^\pm$ momentum region. The $\phi\pi$ invariant mass distribution for the entire momentum region is shown in the Figure 2.

The $D_s^\pm$ momentum spectrum for both on-resonance data and off-resonance data is shown in Figure 3. The off-resonance data is normalized with the scale factor from the ratio of the $D_s^\pm$ number which has x as greater than 0.5 where is continuum region. In order to measure the momentum spectrum of $D_s^\pm$ mesons, we estimate the $D_s^\pm$ detection efficiency as a function of momentum from a Monte Carlo simulation in Figure 4. The $D_s^\pm$ momentum spectrum after the off-resonance spectrum is subtracted from the on-resonance spectrum and after corrections for detection efficiency is shown in Figure 5.

The total yield are 106,200 $\pm$ 880 $D_s^\pm$ mesons from B decay before efficiency correction which correspond to 352,500 $\pm$ 3,050 $D_s^\pm$ mesons from B decay after efficiency correction. The inclusive branching fraction is calculated to be

$$Br(B \to D_s^{\pm} X) = (11.7 \pm 0.10 \pm 1.0 \pm 2.9)\%$$

where the first error is statistical, the second is the systematic error, and the third is due to the uncertainty in the $D_s^{\pm} \to \phi\pi^{\pm}$ branching fraction. The largest error in this measurement is the 25% uncertainty in the $D_s^{\pm} \to \phi\pi^{\pm}$ branching fraction. This error is displayed separately to distinguish it from the other 8.9 % systematic error associated with detector effects and the analysis method. The list of systematic error is summarized in the Table 1.

A.4 The Inclusive $B \to D_s^{*\pm}$ Branching Fraction

We use the $D_s^{*\pm} \to D_s^{\pm}\gamma$ decay chain to reconstruct $D_s^{*\pm}$. The criteria for reconstruction of the $D_s^{\pm}$ is the same as the analysis for $Br(B \to D_s^{\pm} X)$. We required the $\phi\pi^{\pm}$ invariant mass to be within 10 MeV of the $D_s^{\pm}$ nominal mass. We use the photon whose energy is greater than 140 MeV in the laboratory frame. The procedure to measure the momentum spectrum of $D_s^{*\pm}$ is almost the same as that for $D_s^{\pm}$. We use the same normalization factor for on-resonance data and off-resonance data as we did in the analysis for $Br(B \to D_s^{\pm} X)$. We use also the same scaled $D_s^{*\pm}$ momentum, which is defined as $x \equiv P^*_{D_s^{*\pm}}/P_{max}$ where $P_{max} = \sqrt{E_{beam}^2 - M_{D_s^{*\pm}}^2}$, where $P^*_{D_s^{*\pm}}$ is the momentum of $D_s^{*\pm}$ in the $\Upsilon(4S)$ rest frame, E_{beam} is 5.29 GeV for on-resonance data, and 5.26 GeV for off-resonance data. The endpoint of the $D_s^{*\pm}$ mesons produced from B decay is x = 0.49 with the correction for the B meson velocity ($\beta_B = 0.06$). We define the signal region as using $0 \leq x < 0.48$ for the $D_s^{*\pm}$ meson from B meson.

We extract the yield of $D_s^{*\pm}$ as a function of momentum by fitting the distribution that is difference between $D_s^{\pm}\gamma$ invariant mass and $\phi\pi^{\pm}$ invariant mass plots for each bin of x. The bin size of 0.04 is an order of magnitude larger than the resolution of x. We use a double Gaussian for the signal shape and a threshold function for the combinatorial background shape which is described as below.

$$f(x) = P_1(x - P_2)^{P_3} exp\{P_4(x - P_2)\}, \text{ where } P_1,\ P_2,\ P_3 \text{ and } P_4 \text{ are free parameter.}$$

We fixed the mean, widths and the ratio of two areas of the double Gaussian with the values from fitting to the mass difference between the $D_s^{\pm}\gamma$ invariant mass and the $\phi\pi^{\pm}$ invariant mass for the entire $D_s^{*\pm}$ momentum region. The mass difference between the $D_s^{\pm}\gamma$ invariant mass and the $\phi\pi^{\pm}$ invariant mass distribution for the entire momentum region is shown in the Figure 6.

The $D_s^{*\pm}$ momentum spectrum for both on-resonance data and off-resonance data is shown in Figure 7. The off-resonance data is normalized with the scale factor from the ratio of the $D_s^{\pm}$ number which has x as greater than 0.5 where is continuum region. In order to measure the momentum spectrum of the $D_s^{*\pm}$ meson, we estimate the $D_s^{*\pm}$ detection efficiency as a function of momentum from a Monte Carlo simulation in Figure 8. The $D_s^{*\pm}$ momentum spectrum after the spectrum of off-resonance is subtracted from the spectrum of on-resonance and after correction with detection efficiency is shown in Figure 9.

The total yield is 21,990 $\pm$ 580 $D_s^{*\pm}$ mesons from B decay before efficiency corrected which correspond to 200,300 $\pm$ 5,500 $D_s^{*\pm}$ mesons from B decay after efficiency corrected. The inclusive branching fraction is calculated to be

$$Br(B \rightarrow D_s^{*\pm} X) = (7.07 \pm 0.19 \pm 0.71 \pm 1.77)\%$$

where the first error is statistical, the second is the systematic error, and the third is due to the uncertainty in the $D_s^{\pm} \rightarrow \phi\pi^{\pm}$ branching fraction. The largest error in this measurement is the 25% uncertainty in the $D_s^{\pm} \rightarrow \phi\pi^{\pm}$ branching fraction. This error is also displayed separately to distinguish it from the other 10 % systematic error associated with detector effects and the analysis method. The list of systematic error is summarized in the Table 1.

Systematics	D_s	D_s^*
Br($D_s^\pm \to \phi\ \pi^\pm$)	25%	25%
Br($\phi \to K^+\ K^-$)	1.4%	1.4%
Number of $B\overline{B}$	1%	1%
3 tracking	6.0%	6.0%
PID	6.0%	6.0%
bining	1.0%	3.6%
Fitting shape (Signal)	1.9%	0.8%
Fitting shape (B.G.)	0.3%	1.3%
Low momentum photon efficiency	-	3.3%
Br($D_s^* \to D_s\gamma$)	-	2.7%
Total other than Br($D_s^\pm \to \phi\ \pi^\pm$)	8.9%	10%

Table A.1: Summary of systematic uncertainties

A.5 Summary

We measured the branching fraction of the inclusive $B \to D_s^\pm X$ decay and the inclusive $B \to D_s^{*\pm} X$ decay as $Br(B \to D_s^\pm X) = (11.7 \pm 0.1 \pm 1.0 \pm 2.9)\%$, and the branching fraction of the inclusive $Br(B \to D_s^{*\pm} X) = (7.07 \pm 0.19 \pm 0.71 \pm 1.77)\%$. using 78.1 fb^{-1} $\Upsilon(4S)$ on-resonance data and 8.8 fb^{-1} $\Upsilon(4S)$ off-resonance data which is accumulated with the BELLE detector and the KEKB accelerator. (Preliminary, belle note#557)

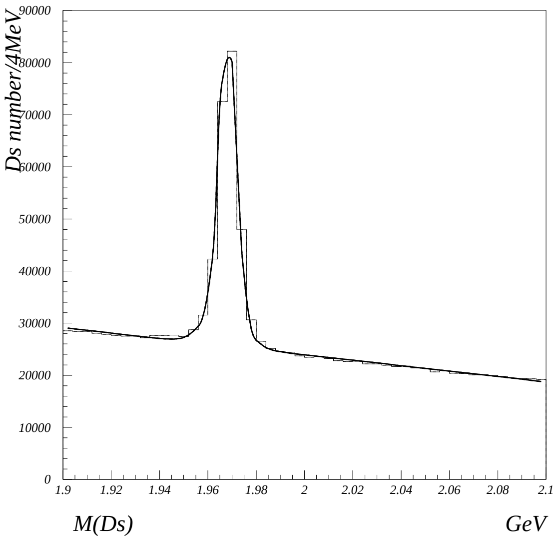

Figure A.2: The $M_{\phi\pi}$ invariant mass distribution for $78.8fb^{-1}$ of on-resonance data

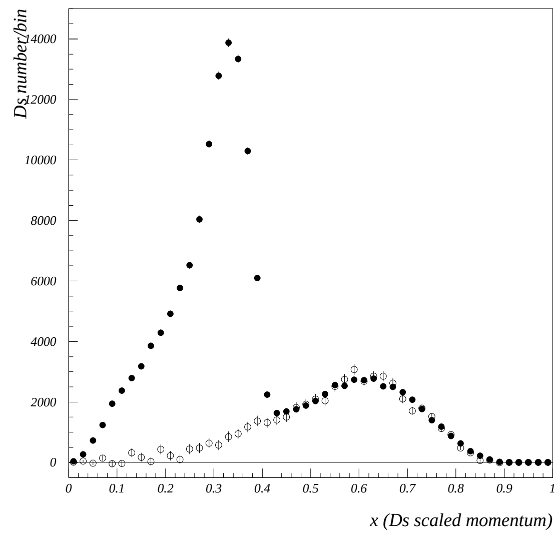

Figure A.3: The $D_s^{\pm}$ momentum spectrum for $78.8fb^{-1}$ of on-resonance data (filled circle) and for $8.8fb^{-1}$ of off-resonance data (open circle) that is normalized to the on-resonance data

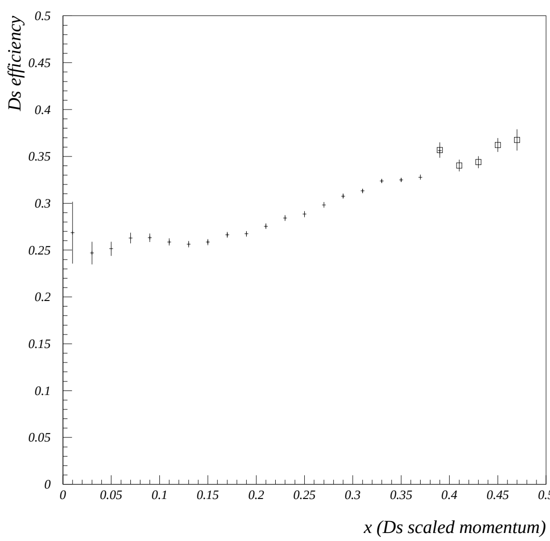

Figure A.4: The $D_s^{\pm}$ efficiency v.s. scaled momentum for the $b \rightarrow c\ D_s^-$ Monte Carlo (dot) and for the $b \rightarrow u\ D_s^-$ Monte Carlo (open square)

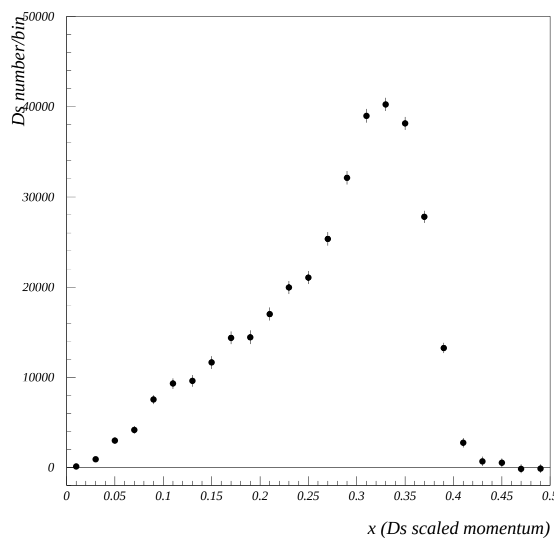

Figure A.5: The $D_s^{\pm}$ momentum spectrum after subtraction of off-resonance data and after efficiency corrections with the bin by bin efficiency

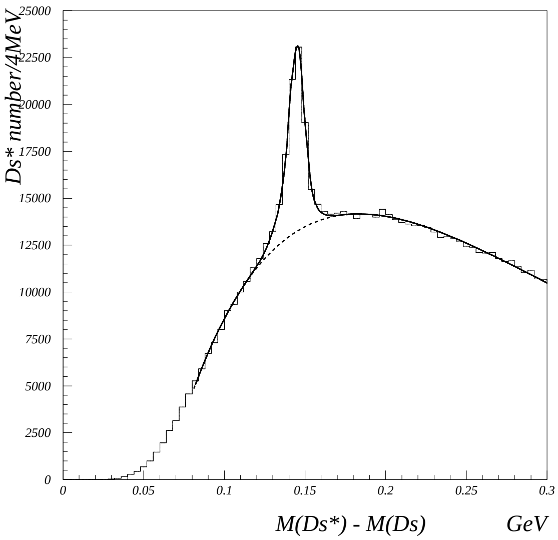

Figure A.6: The mass difference between the $D_s^{\pm}\gamma$ invariant mass and the $\phi\pi^{\pm}$ invariant mass for $78.8fb^{-1}$ of on-resonance data

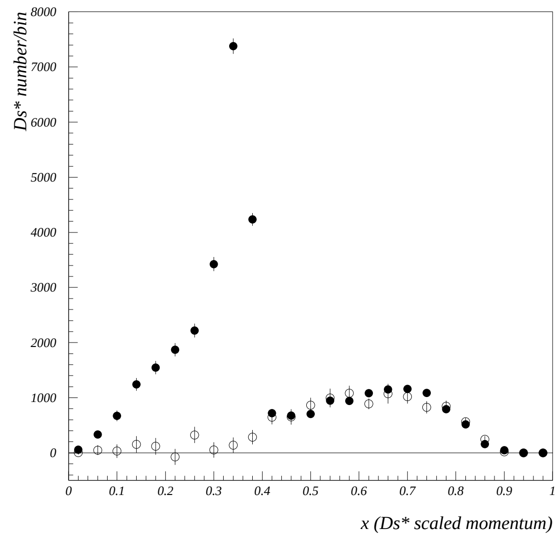

Figure A.7: The $D_s^{*\pm}$ momentum spectrum for $78.8fb^{-1}$ of on-resonance data (filled circle) and for $8.8fb^{-1}$ of off-resonance data (open circle) that is normalized to the on-resonance data

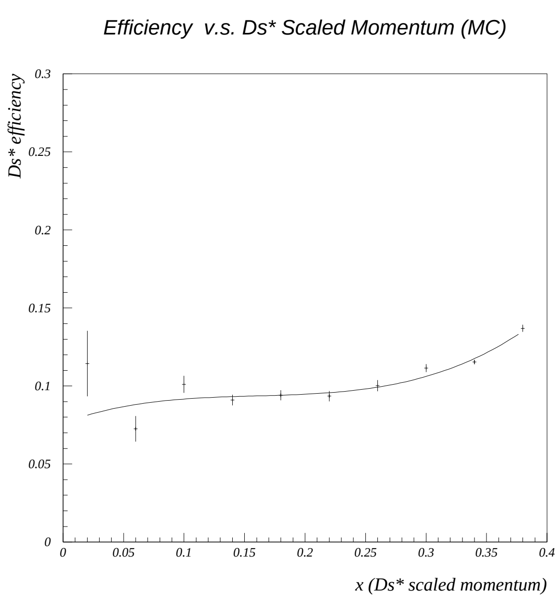

Figure A.8: The $D_s^{*\pm}$ efficiency v.s. scaled momentum for the $b \rightarrow c\ D_s^{*-}$ Monte Carlo

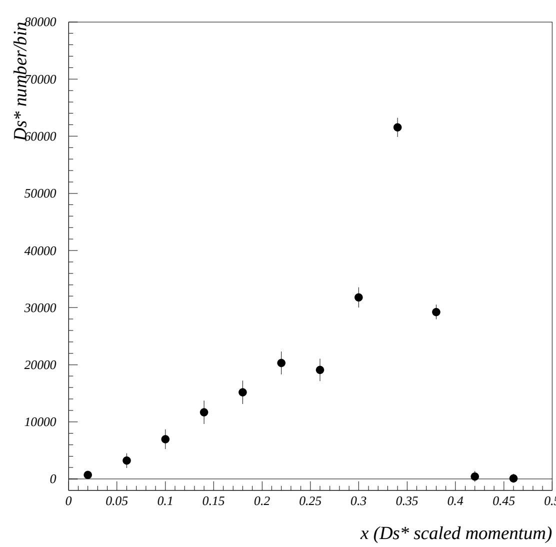

Figure A.9: The $D_s^{*\pm}$ momentum spectrum after subtraction of off-resonance data and after efficiency corrections with the efficiency curve

Appendix B

Inclusive D_s momentum spectrum

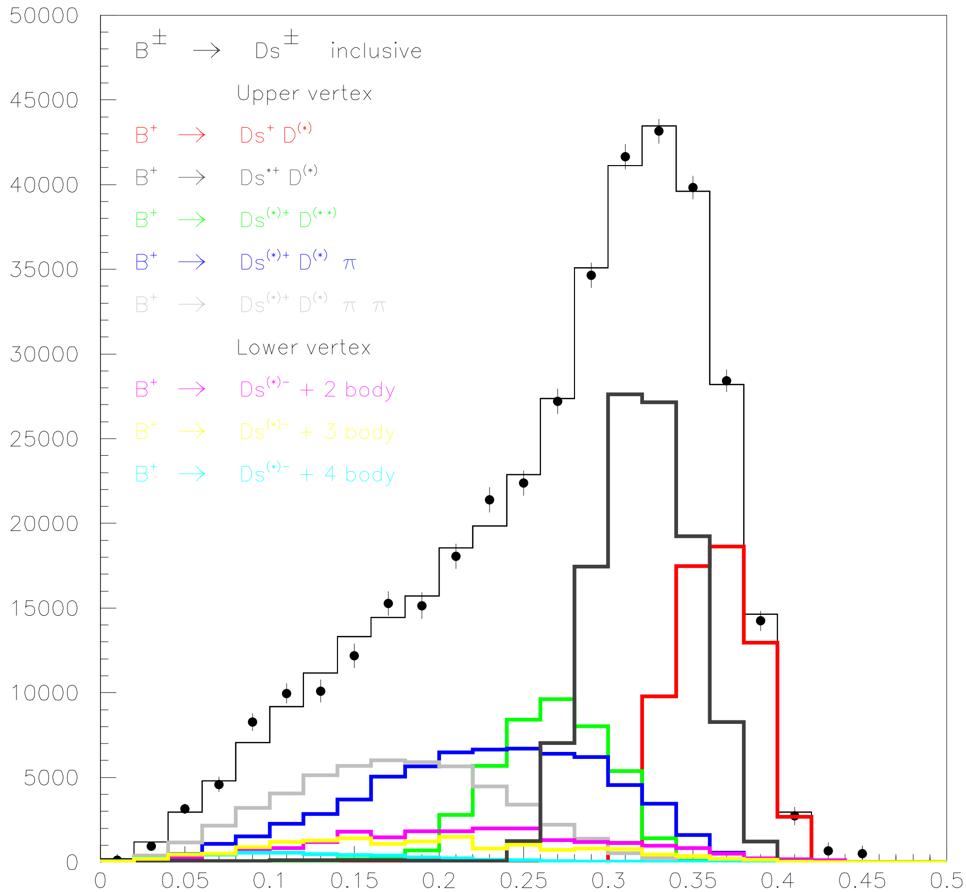

Horizontal axis mean D_s scaled momentum and it have 0.5 for momentum $\sim$ 2.5 GeV/c.

Figure B.1: Dots means inclusive D_s momentum spectrum in B decay with using data after efficiency correction and colored histograms are each decays component in test.

Appendix C

Kinematics of $b \to q\ D_s$ decay

In the decay of $b \to q\ D_s$, the invariant amplitude $\mathcal{M}$ becomes

$$\mathcal{M} = (\overline{u'}\sqrt{2}G\gamma^{\mu}P_L u) f q_{\mu} \tag{C.1}$$
$$\tag{C.2}$$

where u is the four-component spinor of b-quark, $\overline{u'}$ is the four-component spinor of u-quark or c-quark, f is the decay constant of D_s, and q_{μ} is the four momentum of D_s.

$$= \sqrt{2}Gf\overline{u'}\not{q}\, P_L u \tag{C.3}$$
$$= \sqrt{2}Gf\overline{u'}(\not{P} - \not{P}')P_L u \tag{C.4}$$

where P is the four momentum of b-quark, and P' is the four momentum of u-quark or c-quark.

$$= \sqrt{2}Gf(\overline{u'}\not{P}\, P_L u - \overline{u'}\not{P}' P_L u) \tag{C.5}$$
$$= \sqrt{2}Gf(\overline{u'}P_R\not{P}\, u - \overline{u'}\not{P}' P_L u) \tag{C.6}$$
$$= \sqrt{2}Gf(\overline{u'}P_R\, m\, u - m'\ \overline{u'}P_L u) \tag{C.7}$$
$$= \sqrt{2}Gf\overline{u'}V u \tag{C.8}$$

where m is the mass of b-quark, and m' is the mass of u-quark or c-quark. And, replaced $(m\,P_R - m'P_L)$ with V, then $\overline{V}$ becomes $(m\,P_L - m'P_R)$, therefore spin sum becomes

$$\sum_{spin} |\mathcal{M}|^2 = 2G^2 f^2 \sum_{spin} |\overline{u'}V u|^2 \tag{C.9}$$

$$
\begin{aligned}
&= 2G^2 f^2 \sum_{spin} \overline{u'} V u \overline{u} \overline{V} u' && \text{(C.10)}\\
&= 2G^2 f^2\, Tr\{(\not{P}' + m')V(\not{P} + m)\overline{V}\} && \text{(C.11)}\\
&= 2G^2 f^2\, (Tr \not{P}' V \not{P}\, \overline{V} + m\, m'\, Tr\, V\overline{V}) && \text{(C.12)}
\end{aligned}
$$

then, $\not{P}' V \not{P}\, \overline{V}$ and $V\overline{V}$ are

$$
\begin{aligned}
\not{P}' V \not{P}\, \overline{V} &= \not{P}'(m\, P_R - m' P_L)\, \not{P}\, (m\, P_L - m' P_R) && \text{(C.13)}\\
&= \not{P}' \not{P}\, (m\, P_L - m' P_R)\, (m\, P_L - m' P_R) && \text{(C.14)}\\
&= \not{P}' \not{P}\, (m^2 P_L + m'^2 P_R) && \text{(C.15)}\\
&= \frac{\not{P}' \not{P}}{2} \{(m^2 + m'^2) - (m^2 - m'^2)\gamma_5\} && \text{(C.16)}
\end{aligned}
$$

and

$$
\begin{aligned}
V\overline{V} &= (m\, P_R - m' P_L)\, (m\, P_L - m' P_R) && \text{(C.17)}\\
&= -m\, m'(P_L + P_R) && \text{(C.18)}\\
&= -m\, m' && \text{(C.19)}
\end{aligned}
$$

therefore, equations of (A.16), (A.19) and (A.12) introduce

$$
\begin{aligned}
\sum_{spin} |\mathcal{M}|^2 &= 2G^2 f^2 \{(m^2 + m'^2)\frac{Tr \not{P}' \not{P}}{2} - (m^2 - m'^2) Tr \not{P}' \not{P}\, \gamma_5 - m^2\, m'^2 Tr 1\} && \text{(C.20)}\\
&= 2G^2 f^2 \{(m^2 + m'^2)(2\not{P}' \cdot \not{P}\,) - 4m^2\, m'^2\} && \text{(C.21)}\\
&= 4G^2 f^2 \{(m^2 + m'^2)\, m\, E' - 2m^2\, m'^2\} && \text{(C.22)}\\
& && \text{(C.23)}
\end{aligned}
$$

because $P = (m, 0)$ and $P' \equiv (E', \overrightarrow{P'})$ in the b-quark frame means $\not{P}' \cdot \not{P}\, = mE'$, so the two body decay lead,

$$
\begin{aligned}
\Gamma &= \frac{|\vec{P'}|}{8\pi\, m^2} \sum_{spin} |\mathcal{M}|^2 && \text{(C.24)}\\
&= \frac{G^2 f^2}{2\pi}\, |\vec{P'}|\, m^2 \{(1 + \frac{m'^2}{m^2})\frac{E'}{m} - 2\frac{m'^2}{m^2}\} && \text{(C.25)}
\end{aligned}
$$

then, E' and $|\overrightarrow{P'}|$ can be described with M_{D_s} (which is the mass of D_s), x $\equiv M_{D_s}/m$, and y $\equiv m'/m$ as follows

$$
\begin{aligned}
E' &= \frac{m^2 + m'^2 - M_{Ds}^2}{2m} && \text{(C.26)} \\
&= m\,(\frac{1 + y^2 - x^2}{2}) && \text{(C.27)}
\end{aligned}
$$

and

$$
\begin{aligned}
P'^2 &= E'^2 - m'^2 && \text{(C.28)} \\
&= (\frac{m^2 + m'^2 - M_{Ds}^2}{2m})^2 - m'^2 && \text{(C.29)} \\
&= m^2(\frac{1 + x^4 + y^4 - 2x^2 - 2x^2y^2 - 2y^2}{4}) && \text{(C.30)} \\
&= m^2[\frac{\{1 - (x+y)^2\}\{1 - (x-y)^2\}}{4}] && \text{(C.31)}
\end{aligned}
$$

therefore, equations of (A.27), (A.31) and (A.25) introduce

$$
\begin{aligned}
\Gamma &= \frac{G^2 f^2}{8\pi} m^3 \sqrt{\{1 - (x+y)^2\}\{1 - (x-y)^2\}} \times \{(1 - y^2)(1 + y^2 - x^2) - 4y^2\} && \text{(C.32)} \\
&= \frac{G^2 f^2}{8\pi} m^3 \sqrt{\{1 - (x+y)^2\}\{1 - (x-y)^2\}} \times \{1 - x^2 - 2y^2 - x^2y^2 + y^4\} && \text{(C.33)}
\end{aligned}
$$

replacement of the equation (A.33) with mass of each particles again, we gain

$$
\Gamma \propto \sqrt{\{1 - (\frac{M_{D_s}}{m} + \frac{m'}{m})^2\}\{1 - (\frac{M_{D_s}}{m} - \frac{m'}{m})^2\}} \times \{1 - (\frac{M_{D_s}}{m})^2 - 2(\frac{m'}{m})^2 - (\frac{M_{D_s}}{m})^2(\frac{m'}{m})^2 + (\frac{m'}{m})^4\}
$$

where, M_{D_s} means mass of D_s meson, m means mass of bottom quark and m' means mass of charm quark.

Appendix D

Phys. Rev. Lett. draft

VOLUME 92, NUMBER 1 PHYSICAL REVIEW LETTERS week ending 9 JANUARY 2004

Measurements of the D_{sJ} Resonance Properties

Y. Mikami,[38] K. Abe,[7] T. Abe,[7] H. Aihara,[39] M. Akemoto,[7] Y. Asano,[44] T. Aso,[43] T. Aushev,[11] S. Bahinipati,[4]
A. M. Bakich,[34] Y. Ban,[29] A. Bay,[16] I. Bizjak,[12] A. Bondar,[2] A. Bozek,[23] M. Bračko,[18,12] T. E. Browder,[6] Y. Chao,[22]
B. G. Cheon,[33] R. Chistov,[11] S.-K. Choi,[5] Y. Choi,[33] Y. K. Choi,[33] A. Chuvikov,[30] M. Danilov,[11] L. Y. Dong,[9] J. Dragic,[19]
S. Eidelman,[2] V. Eiges,[11] C. Fukunaga,[41] K. Furukawa,[7] N. Gabyshev,[7] A. Garmash,[2,7] T. Gershon,[7] G. Gokhroo,[35]
B. Golob,[17,12] F. Handa,[38] T. Hara,[27] H. Hayashii,[21] M. Hazumi,[7] I. Higuchi,[38] L. Hinz,[16] T. Hokuue,[20] Y. Hoshi,[37]
W.-S. Hou,[22] H.-C. Huang,[22] T. Iijima,[20] H. Ikeda,[7] K. Inami,[20] A. Ishikawa,[20] H. Iwasaki,[7] M. Iwasaki,[39] Y. Iwasaki,[7]
J. H. Kang,[47] J. S. Kang,[14] P. Kapusta,[23] N. Katayama,[7] H. Kawai,[3] N. Kawamura,[1] T. Kawasaki,[25] H. Kichimi,[7]
E. Kikutani,[7] H. J. Kim,[47] J. H. Kim,[33] K. Kinoshita,[4] P. Koppenburg,[7] P. Križan,[17,12] P. Krokovny,[2] R. Kulasiri,[4]
A. Kuzmin,[2] Y.-J. Kwon,[47] G. Leder,[10] S. H. Lee,[32] T. Lesiak,[23] S.-W. Lin,[22] D. Liventsev,[11] J. MacNaughton,[10]
G. Majumder,[35] F. Mandl,[10] M. Masuzawa,[7] T. Matsumoto,[41] A. Matyja,[23] T. Mimashi,[7] W. Mitaroff,[10] H. Miyata,[25]
G. R. Moloney,[19] T. Nagamine,[38] Y. Nagasaka,[8] T. T. Nakamura,[7] E. Nakano,[26] M. Nakao,[7] H. Nakazawa,[7]
Z. Natkaniec,[23] S. Nishida,[7] O. Nitoh,[42] T. Nozaki,[7] S. Ogawa,[36] Y. Ogawa,[7] K. Ohmi,[7] T. Ohshima,[20] N. Ohuchi,[7]
K. Oide,[7] T. Okabe,[20] S. Okuno,[13] S. L. Olsen,[6] W. Ostrowicz,[23] H. Ozaki,[7] P. Pakhlov,[11] H. Palka,[23] C.W. Park,[14]
H. Park,[15] K. S. Park,[33] N. Parslow,[34] L. E. Piilonen,[45] H. Sagawa,[7] S. Saitoh,[7] Y. Sakai,[7] O. Schneider,[16] C. Schwanda,[7,10]
A. J. Schwartz,[4] S. Semenov,[11] K. Senyo,[20] M. E. Sevior,[19] H. Shibuya,[36] T. Shidara,[7] B. Shwartz,[2] V. Sidorov,[2]
J. B. Singh,[28] N. Soni,[28] S. Stanič,[44,*] M. Starič,[12] R. Sugahara,[7] A. Sugi,[20] K. Sumisawa,[27] T. Sumiyoshi,[27] S. Suzuki,[46]
S. Y. Suzuki,[7] F. Takasaki,[7] M. Tanaka,[7] M. Tawada,[7] Y. Teramoto,[26] T. Tomura,[39] K. Trabelsi,[6] T. Tsuboyama,[7]
T. Tsukamoto,[7] S. Uehara,[7] S. Uno,[7] G. Varner,[6] Y. Watanabe,[40] B. D. Yabsley,[45] Y. Yamada,[7] A. Yamaguchi,[38]
H. Yamamoto,[38] Y. Yamashita,[24] M. Yamauchi,[7] H. Yanai,[25] Heyoung Yang,[32] J. Ying,[29] M. Yoshida,[7] Y. Yusa,[38]
Z. P. Zhang,[31] V. Zhilich,[2] and D. Žontar[17,12]

(Belle Collaboration)

[1]*Aomori University, Aomori*
[2]*Budker Institute of Nuclear Physics, Novosibirsk*
[3]*Chiba University, Chiba*
[4]*University of Cincinnati, Cincinnati, Ohio 45221*
[5]*Gyeongsang National University, Chinju*
[6]*University of Hawaii, Honolulu, Hawaii 96822*
[7]*High Energy Accelerator Research Organization (KEK), Tsukuba*
[8]*Hiroshima Institute of Technology, Hiroshima*
[9]*Institute of High Energy Physics, Chinese Academy of Sciences, Beijing*
[10]*Institute of High Energy Physics, Vienna*
[11]*Institute for Theoretical and Experimental Physics, Moscow*
[12]*J. Stefan Institute, Ljubljana*
[13]*Kanagawa University, Yokohama*
[14]*Korea University, Seoul*
[15]*Kyungpook National University, Taegu*
[16]*Institut de Physique des Hautes Énergies, Université de Lausanne, Lausanne*
[17]*University of Ljubljana, Ljubljana*
[18]*University of Maribor, Maribor*
[19]*University of Melbourne, Victoria*
[20]*Nagoya University, Nagoya*
[21]*Nara Women's University, Nara*
[22]*Department of Physics, National Taiwan University, Taipei*
[23]*H. Niewodniczanski Institute of Nuclear Physics, Krakow*
[24]*Nihon Dental College, Niigata*
[25]*Niigata University, Niigata*
[26]*Osaka City University, Osaka*
[27]*Osaka University, Osaka*
[28]*Panjab University, Chandigarh*
[29]*Peking University, Beijing*
[30]*Princeton University, Princeton, New Jersey 08545*
[31]*University of Science and Technology of China, Hefei*

 0031-9007/04/92(1)/012002(6)$20.00

[32]Seoul National University, Seoul
[33]Sungkyunkwan University, Suwon
[34]University of Sydney, Sydney NSW
[35]Tata Institute of Fundamental Research, Bombay
[36]Toho University, Funabashi
[37]Tohoku Gakuin University, Tagajo
[38]Tohoku University, Sendai
[39]Department of Physics, University of Tokyo, Tokyo
[40]Tokyo Institute of Technology, Tokyo
[41]Tokyo Metropolitan University, Tokyo
[42]Tokyo University of Agriculture and Technology, Tokyo
[43]Toyama National College of Maritime Technology, Toyama
[44]University of Tsukuba, Tsukuba
[45]Virginia Polytechnic Institute and State University, Blacksburg, Virginia 24061
[46]Yokkaichi University, Yokkaichi
[47]Yonsei University, Seoul

(Received 7 October 2003; published 6 January 2004)

We report measurements of the properties of the $D_{sJ}^+(2317)$ and $D_{sJ}^+(2457)$ resonances produced in continuum e^+e^- annihilation near $\sqrt{s} = 10.6$ GeV. The analysis is based on an 86.9 fb^{-1} data sample collected with the Belle detector at KEKB. We determine the masses to be $M(D_{sJ}^+(2317)) = 2317.2 \pm 0.5(\text{stat}) \pm 0.9(\text{syst})\ \text{MeV}/c^2$ and $M(D_{sJ}^+(2457)) = 2456.5 \pm 1.3(\text{stat}) \pm 1.3(\text{syst})\ \text{MeV}/c^2$. We observe the radiative decay mode $D_{sJ}^+(2457) \to D_s^+\gamma$ and the dipion decay mode $D_{sJ}^+(2457) \to D_s^+\pi^+\pi^-$ and determine their branching fractions. No corresponding decays are observed for the $D_{sJ}(2317)$ state. These results are consistent with the spin-parity assignments of 0^+ for the $D_{sJ}(2317)$ and 1^+ for the $D_{sJ}(2457)$.

DOI: 10.1103/PhysRevLett.92.012002 PACS numbers: 14.40.Lb, 13.20.Fc, 13.25.Ft

The narrow $D_s\pi^0$ resonance at 2317 MeV$/c^2$, recently observed by the BaBar Collaboration [1], is naturally interpreted as a p-wave excitation of the $c\bar{s}$ system. The observation of a nearby and narrow $D_s^*\pi^0$ resonance by the CLEO Collaboration [2] supports this view, since the mass difference of the two observed states is consistent with the expected hyperfine splitting for a p-wave doublet with total light-quark angular momentum $j = 1/2$ [3,4]. The observed masses are, however, considerably lower than potential model predictions [6] and similar to those of the $c\bar{u}$ $j = 1/2$ doublet states recently reported by Belle [7]. This has led to speculation that the new $D_s^{(*)}\pi^0$ resonances, which we denote D_{sJ}, may be exotic mesons [8–13]. Measurements of the D_{sJ} quantum numbers and branching fractions (particularly those for radiative decays) will play an important role in determining the nature of these states.

In this Letter we report measurements of the D_{sJ} masses, widths, and branching fractions using a sample of $e^+e^- \to c\bar{c}$ events collected with the Belle detector [14] at the KEKB collider [15].

We reconstruct D_s^+ mesons using the decay chain $D_s^+ \to \phi\pi^+$ and $\phi \to K^+K^-$. To identify kaons or pions, we form a likelihood for each track, $\mathcal{L}_{K(\pi)}$, from dE/dx measurements in a 50-layer central drift chamber, the responses from aerogel threshold Čerenkov counters, and time-of-flight scintillation counters. The kaon likelihood ratio, $P(K/\pi) = \mathcal{L}_K/(\mathcal{L}_K + \mathcal{L}_\pi)$, has values between 0 (likely to be a pion) and 1 (likely to be a kaon).

For $\phi \to K^+K^-$ candidates we use oppositely charged track pairs where one track has $P(K/\pi) > 0.5$ and the other has $P(K/\pi) > 0.2$, and with a K^+K^- invariant mass that is within 10 MeV$/c^2$($\sim$2.5σ) of the nominal ϕ mass. We define the ϕ helicity angle θ_H to be the angle between the direction of the K^+ and the D_s^+ in the ϕ rest frame. For signal events this has a $\cos^2\theta_H$ distribution, while for background it is flat; we require $|\cos\theta_H| > 0.35$.

We reconstruct D_s^+ candidates by combining a ϕ candidate with a π^+ candidate, which is a charged track with $P(K/\pi) < 0.9$, and requiring $M(\phi\pi^+)$ to be within 10 MeV$/c^2$($\sim$2σ) of the nominal D_s^+ mass. We use the D_s^+ sideband regions $1920 < M(\phi\pi^+) < 1940$ MeV$/c^2$ and $1998 < M(\phi\pi^+) < 2018$ MeV$/c^2$ for background studies.

For π^0 reconstruction, we use photons with e^+e^- rest frame (c.m.) energies greater than 100 MeV and select $\gamma\gamma$ pairs that have an invariant mass $M(\gamma\gamma)$ within 10 MeV$/c^2$($\sim$2σ) of the π^0 mass. For background studies we use the π^0 sideband regions $105 \le M_{\gamma\gamma} \le 115$ MeV$/c^2$ and $155 \le M_{\gamma\gamma} \le 165$ MeV$/c^2$.

We reconstruct D_s^{*+} in the $D_s^+\gamma$ final state. We use photons with c.m. energies greater than 100 MeV and require D_s^{*+} candidates to satisfy $127 \le \Delta M(D_s^+\gamma) \le 157$ MeV$/c^2$($\sim$3σ), where $\Delta M(D_s^+\gamma) = M(D_s^+\gamma) - M_{D_s^+}$. The D_s^{*+} sideband regions are defined as $87 \le \Delta M(D_s^+\gamma) \le 117$ MeV$/c^2$ and $167 \le \Delta M(D_s^+\gamma) \le 197$ MeV$/c^2$. The sideband yield is defined as an average of the two regions.

The $\Delta M(D_s^+\pi^0) = M(D_s^+\pi^0) - M_{D_s^+}$ mass-difference distribution for $D_s^+\pi^0$ combinations with $p^*(D_s^+\pi^0) > 3.5$ GeV/c is shown in Fig. 1(a). Here, and in analyses of other D_{sJ} states and modes, we require the c.m. momentum to satisfy $p^*(D_{sJ}) > 3.5$ GeV/c to remove contributions from $B\bar{B}$ events. We do not remove multiple candidates in the subsequent analysis. Also shown are the distributions for the D_s^+ (solid line) and π^0 (dashed line) sideband regions. The prominent peak in the figure corresponds to the $D_{sJ}(2317) \to D_s^+\pi^0$ signal; the peak at small ΔM values is due to $D_s^{*+}(2112) \to D_s^+\pi^0$. No peak is seen in the sideband distributions.

Figure 1(b) shows the $\Delta M(D_s^{*+}\pi^0) = M(D_s^{*+}\pi^0) - M_{D_s^{*+}}$ distribution for $p^*(D_s^{*+}\pi^0) > 3.5$ GeV/c, where a peak corresponding to $D_{sJ}(2457) \to D_s^{*+}\pi^0$ is evident. Also shown is the distribution for the D_s^{*+} sideband region, where we notice the presence of a wider peak in the $D_{sJ}(2457)$ region. The $\Delta M(D_s^{*+}\pi^0)$ distributions for the D_s^+ and π^0 sideband regions show no such peak.

To study the expected signal shape and detection efficiencies, and to determine the level of cross-feed between the two states, we use a Monte Carlo (MC) simulation that treats the $D_{sJ}(2317)$ as a scalar particle with mass 2317 MeV/c^2 decaying to $D_s^+\pi^0$ and the $D_{sJ}(2457)$ as an axial-vector particle with mass 2457 MeV/c^2 decaying to $D_s^{*+}\pi^0$. Zero intrinsic width is assigned to both states. We find that the $D_{sJ}(2317)$ produces a peak of width 7.1 ± 0.2 MeV/c^2 in the $\Delta M(D_s^+\pi^0)$ distribution at its nominal mass, and a broader reflection peak (of width 12.3 ± 1.8 MeV/c^2) at a mass of 8 MeV/c^2 above the $D_{sJ}(2457)$ peak. This latter peak corresponds to a D_s^+ and π^0 from a $D_{sJ}(2317)$ decay that are combined with a random photon that passes the $|M(D_s^+\gamma) - M_{D_s^{*+}}| < 15$ MeV/c^2 requirement. (We refer to this as "feed-up background.") The $D_{sJ}(2457)$ produces a peak of width 6.0 ± 0.2 MeV/c^2 at its nominal mass and a broader peak (of width 19.5 ± 3.6 MeV/c^2), also at its nominal mass. The latter peak is due to events in which the photon from $D_s^{*+} \to D_s^+\gamma$ is missed, and a random photon is reconstructed in its place (referred to as the "broken-signal background"). In addition, the $D_{sJ}(2457)$ produces a reflection in the $D_s^+\pi^0$ mass distribution with width 14.9 ± 0.8 MeV/c^2 at a mass of 4 MeV/c^2 below the $D_{sJ}(2317)$ peak (referred to as "feed-down background").

While we must depend on the MC for separating the signal peak and the feed-down background in the $D_{sJ}(2317)$ region, the feed-up and broken-signal backgrounds for the $D_{sJ}(2457)$ region occur when $D_s^{*+}\pi^0$ combinations are formed from candidates in the D_s^{*+} mass sideband. This is evident in Fig. 1(b).

Figure 2(b) shows the sideband-subtracted $\Delta M(D_s^{*+}\pi^0)$ distribution together with the results of a fit that uses a Gaussian to represent the $D_{sJ}(2457)$ signal and a second-order polynomial for the background. The fit gives a signal yield of 126 ± 25 events with a peak value of $\Delta M = 344.1 \pm 1.3$ MeV/c^2 (corresponding to $M = 2456.5 \pm 1.3$ MeV/c^2). The width from the fit, $\sigma = 5.8 \pm 1.3$ MeV/c^2, is consistent with MC expectations for a zero intrinsic width particle.

Figure 2(a) shows the fit result for the $D_{sJ}(2317)$. Here both the signal and the feed-down background are represented as Gaussian shapes modeled from the MC. The mean and σ of the feed-down component are fixed according to the MC and normalized by the measured $D_{sJ}(2457)$ yield. A third-order polynomial is used to represent the non-feed-down background. The fit gives a yield of 761 ± 44 events and a peak ΔM value of 348.7 ± 0.5 MeV/c^2 (corresponding to $M = 2317.2 \pm 0.5$ MeV/c^2). Here again, the width from the fit, $\sigma = 7.6 \pm 0.5$ MeV/c^2, is consistent with MC expectations for a zero intrinsic width particle.

There are systematic errors in the measurements due to uncertainties in the (i) π^0 energy calibration, (ii) parametrization of the cross-feed backgrounds, (iii) parametrization for the non-cross-feed backgrounds, (iv) possible discrepancies between the input and the output seen in the MC simulations, and (v) the uncertainty in the world average value for $M_{D_s^+}$ and $M_{D_s^{*+}}$.

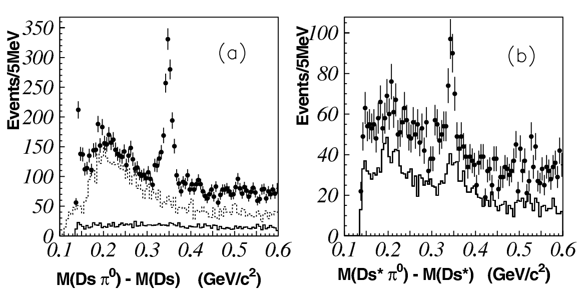

FIG. 1. (a) The $\Delta M(D_s^+\pi^0)$ distribution. Data from the D_s^+ (solid line) and π^0 (dashed line) sideband regions are also shown. (b) The $\Delta M(D_s^{*+}\pi^0)$ distribution. Data from the D_s^* sideband (histogram) region are also shown.

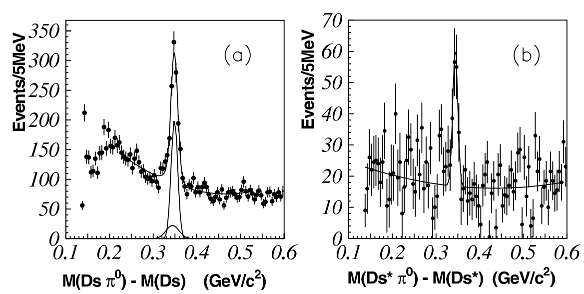

FIG. 2. (a) The $\Delta M(D_s^+\pi^0)$ distribution. The narrow Gaussian peak is the fitted $D_{sJ}(2317)$ signal, whereas the wider Gaussian peak is the feed-down background. (b) The $\Delta M(D_s^{*+}\pi^0)$ distribution after bin-by-bin subtraction of the D_s^{*+} sideband from the D_s^{*+} signal distribution. The curve is the fit result.

The π^0 energy calibration is studied using $D_s^{*+}(2112) \to D_s^+ \pi^0$ events in the same data sample. We measure $\Delta M = 144.3 \pm 0.1$ MeV$/c^2$ and $\sigma = 1.0 \pm 0.1$ MeV$/c^2$, which agrees well with the Particle Data Group (PDG) value of $\Delta M = 143.8 \pm 0.4$ MeV$/c^2$. The MC, which uses the PDG value as an input, gives $\Delta M = 143.9 \pm 0.1$ MeV$/c^2$ and $\sigma = 1.0 \pm 0.1$ MeV$/c^2$. (The errors quoted here are statistical only.) We attribute the difference to the π^0 energy calibration uncertainty and conservatively assign a ± 0.6 MeV$/c^2$ error to this effect. This error contributes only to the mass measurements.

For the cross-feed background to the $D_{sJ}(2317)$ signal, we vary the feed-down background parameters and the $D_{sJ}(2457)$ yield by $\pm 1\sigma$ and assign the variation in output values as errors. For the $D_{sJ}(2457)$, we determine the uncertainty of the feed-up fraction from the difference between the D_s^* signal region and the sideband region using the MC. For the non-cross-feed background, we repeat the fit using a second-order polynomial for the $D_{sJ}(2317)$ and a linear function for the $D_{sJ}(2457)$ and assign the difference as errors. Shifts between the MC input and output masses for the D_{sJ} can reflect possible errors arising from the choice of signal shape and other factors in the analysis. We observe a 0.3 MeV$/c^2$ shift for the $D_{sJ}(2317)$ and a 0.9 MeV$/c^2$ shift for the $D_{sJ}(2457)$. We assign these shifts as errors.

The final results for the masses are

$$M(D_{sJ}(2317)) = 2317.2 \pm 0.5(\text{stat}) \pm 0.9(\text{syst})\ \text{MeV}/c^2,$$

$$M(D_{sJ}(2457)) = 2456.5 \pm 1.3(\text{stat}) \pm 1.3(\text{syst})\ \text{MeV}/c^2.$$

The $M(D_{sJ}(2317))$ result is consistent with BaBar [1] and CLEO results [2]. Our $M(D_{sJ}(2457))$ value is consistent with BaBar [16] but significantly lower than that from CLEO [2]. We set upper limits for the natural widths of $\Gamma(D_{sJ}(2317)) \leq 4.6$ MeV$/c^2$ and $\Gamma(D_{sJ}(2457)) \leq 5.5$ MeV$/c^2$ (90% C.L.), respectively.

Using the observed signal yields of $761 \pm 44(\text{stat}) \pm 30(\text{syst})$ and $126 \pm 25(\text{stat}) \pm 12(\text{syst})$ for the $D_{sJ}(2317)$ and $D_{sJ}(2457)$, and the detection efficiencies of 8.2% and 4.7% for the $D_{sJ}(2317)$ and $D_{sJ}(2457)$, we determine the ratio

$$\frac{\sigma(D_{sJ}(2457))\mathcal{B}(D_{sJ}^+(2457) \to D_s^{*+}\pi^0)}{\sigma(D_{sJ}(2317))\mathcal{B}(D_{sJ}^+(2317) \to D_s^+\pi^0)} = 0.29 \pm 0.06(\text{stat}) \pm 0.03(\text{syst}).$$

The detection efficiencies are determined from the MC assuming the same fragmentation function for the two states. The dominant source of systematic error is the systematic uncertainty in the $D_{sJ}(2457)$ yield.

In the $D_{sJ}(2457)$ region of the $\Delta M(D_s^+\pi^0)$ distribution, we find 22 ± 22 events from a fit to a possible $D_{sJ}(2457)$ signal. From this, we obtain the upper limit

$$\frac{\mathcal{B}(D_{sJ}^+(2457) \to D_s^+\pi^0)}{\mathcal{B}(D_{sJ}^+(2457) \to D_s^{*+}\pi^0)} \leq 0.21\ (90\%\ \text{C.L.}).$$

The decay to a pseudoscalar pair is allowed for a state with a parity of $(-1)^J$. Thus, absence of such a decay disfavors $D_{sJ}(2457)$ having J^P of 0^+ or 1^-.

Figure 3(a) shows the $\Delta M(D_s^+\gamma) = M(D_s^+\gamma) - M_{D_s^+}$ distribution. Here photons are required to have energies greater than 600 MeV in the c.m. and those that form a π^0 when combined with another photon in the event are not used. A clear peak near $\Delta M(D_s^+\gamma) \sim 490$ MeV$/c^2$, corresponding to the $D_{sJ}(2457)$, is observed. No peak is found in the $D_{sJ}(2317)$ region. The D_s^+ sideband distribution, shown as a histogram, shows no structure. We fit the distribution with a double Gaussian for the signal, which is determined from the MC, and a third-order polynomial for the background. The fit yields 152 ± 18 (stat) events and a ΔM peak at $491.0 \pm 1.3(\text{stat}) \pm 1.9(\text{syst})$ MeV$/c^2$ (corresponding to $M = 2459.5 \pm 1.3(\text{stat}) \pm 2.0(\text{syst})$ MeV$/c^2$). The $D_{sJ}(2457)$ mass determined here is consistent with the value determined from $D_s^*\pi^0$ decays.

Using the detection efficiency of 10.2% for the $D_s^+\gamma$ decay mode, we determine the branching fraction ratio

$$\frac{\mathcal{B}(D_{sJ}^+(2457) \to D_s^+\gamma)}{\mathcal{B}(D_{sJ}^+(2457) \to D_s^{*+}\pi^0)} = 0.55 \pm 0.13(\text{stat}) \pm 0.08(\text{syst}).$$

This result, which has a statistical significance of 10σ, is consistent with the first measurement by Belle [17] $0.38 \pm 0.11(\text{stat}) \pm 0.04(\text{syst})$ with $B \to \bar{D}D_{sJ}(2457)$ decays, and with the theoretical predictions [3,13]. The existence of the $D_{sJ}(2457) \to D_s\gamma$ mode rules out the $0^\pm$ quantum number assignments for the $D_{sJ}(2457)$ state. For the $D_{sJ}(2317)$, we obtain the upper limit

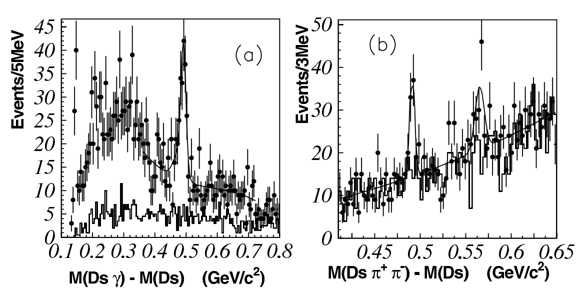

FIG. 3. (a) The $\Delta M(D_s^+\gamma)$ distribution. The curve is a fit using a double Gaussian for the signal and a third-order polynomial for the background. (b) The $\Delta M(D_s^+\pi^+\pi^-)$ distribution. The curve is a fit using Gaussian for the signals and a third-order polynomial for the background.

$$\frac{\mathcal{B}(D_{sJ}^{+}(2317) \to D_s^+\gamma)}{\mathcal{B}(D_{sJ}^{+}(2317) \to D_s\pi^0)} \leq 0.05 \text{ (90\% C.L.)}.$$

From the $M(D_s^{*+}\gamma) = M(D_s^{*+}\gamma) - M_{D_s^{*+}}$ distribution, we determine the upper limits

$$\frac{\mathcal{B}(D_{sJ}^{+}(2317) \to D_s^{*+}\gamma)}{\mathcal{B}(D_{sJ}^{+}(2317) \to D_s\pi^0)} \leq 0.18 \text{ (90\% C.L.)} \quad \text{and}$$

$$\frac{\mathcal{B}(D_{sJ}^{+}(2457) \to D_s^{*+}\gamma)}{\mathcal{B}(D_{sJ}^{+}(2457) \to D_s^{*+}\pi^0)} \leq 0.31 \text{ (90\% C.L.)}.$$

Figure 3(b) shows the $\Delta M(D_s^+\pi^+\pi^-) = M(D_s^+\pi^+\pi^-) - M_{D_s^+}$ distribution. For additional pions, we require at least one of them to have one momentum greater than 300 MeV$/c$ in the c.m., one with $P(K/\pi) < 0.1$ and another with $P(K/\pi) < 0.9$, and $|M(\pi^+\pi^-) - M_{K_S}| \geq$ 15 MeV$/c^2$. A clear peak near $\Delta M(D_s^+\pi^+\pi^-) \sim$ 490 MeV$/c^2$, corresponding to the $D_{sJ}(2457)$, is observed. Evidence of an additional peak near $\Delta M(D_s^+\pi^+\pi^-) \sim 570$ MeV$/c^2$ corresponding to $D_{s1}(2536)$ is also visible. No peak is found in the $D_{sJ}(2317)$ region. The D_s^+ sideband distribution, shown as a histogram, shows no structure. We fit the distribution with Gaussians for the signals, which are determined from the MC, and a third-order polynomial for the background. The fit yields 59.7 ± 11.5(stat) events and a ΔM peak at 491.4 ± 0.9(stat) $\pm$ 1.5(syst) MeV$/c^2$ [corresponding to $M = 2459.9 \pm 0.9$(stat) $\pm$ 1.6(syst) MeV$/c^2$] for $D_{sJ}(2457)$, and 56.5 ± 13.4(stat) events for $D_{s1}(2536)$. The statistical significance is 5.7σ for $D_{sJ}(2457)$, and 4.5σ for $D_{s1}(2536)$. This is the first observation of the $D_{sJ}(2457) \to D_s^+\pi^+\pi^-$ decay mode.

The existence of the $D_{sJ}(2457) \to D_s\pi^+\pi^-$ mode also rules out the 0^+ assignment for $D_{sJ}(2457)$. Using the detection efficiency of 15.8% for the $D_s\pi^+\pi^-$ decay mode which is determined assuming a phase space distribution for the $\pi^+\pi^-$ invariant mass, we determine the branching fraction ratio

$$\frac{\mathcal{B}(D_{sJ}^{+}(2457) \to D_s^+\pi^+\pi^-)}{\mathcal{B}(D_{sJ}^{+}(2457) \to D_s^{*+}\pi^0)} = 0.14 \pm 0.04\text{(stat)} \pm 0.02\text{(syst)},$$

where the systematic error is dominated by the systematic uncertainty of the $D_{sJ}(2457) \to D_s^{*+}\pi^0$ yield. We establish the upper limit

$$\frac{\mathcal{B}(D_{sJ}^{+}(2317) \to D_s^+\pi^+\pi^-)}{\mathcal{B}(D_{sJ}^{+}(2317) \to D_s^+\pi^0)} \leq 4 \times 10^{-3} \text{ (90\% C.L.)}.$$

Using the detection efficiency of 14.3% for the $D_{s1}(2536) \to D_s\pi^+\pi^-$ decay mode which assumes the same fragmentation function for the $D_{s1}(2536)$ and $D_{sJ}(2457)$, we establish the cross section times branching fraction ratio

$$\frac{\sigma(D_{s1}(2536))\mathcal{B}(D_{s1}^{+}(2536) \to D_s^+\pi^+\pi^-)}{\sigma(D_{sJ}(2457))\mathcal{B}(D_{sJ}^{+}(2457) \to D_s^+\pi^+\pi^-)} = 1.05 \pm 0.32\text{(stat)} \pm 0.06\text{(syst)}.$$

In summary, we observe radiative and dipion decays of the $D_{sJ}(2457)$ and set upper limits on the corresponding decays of the $D_{sJ}(2317)$. We determine the $D_{sJ}(2317)$ and $D_{sJ}(2457)$ masses from their decays to $D_s^+\pi^0$ and $D_s^{*+}\pi^0$, respectively, and set upper limits for their natural widths. We set an upper limit on the decay of $D_{sJ}(2457)$ to $D_s^+\pi^0$. These results are consistent with the spin-parity assignments for the $D_{sJ}(2317)$ and $D_{sJ}(2457)$ of 0^+ and 1^+, respectively.

We thank the KEKB accelerator group for the excellent operation of the KEKB accelerator. We acknowledge support from the Ministry of Education, Culture, Sports, Science, and Technology of Japan and the Japan Society for the Promotion of Science; from the Australian Research Council and the Australian Department of Education, Science and Training; from the National Science Foundation of China under Contract No. 10175071; from the Department of Science and Technology of India; from the BK21 program of the Ministry of Education of Korea and the CHEP SRC program of the Korea Science and Engineering Foundation; from the Polish State Committee for Scientific Research under Contract No. 2P03B 01324; from the Ministry of Science and Technology of the Russian Federation; from the Ministry of Education, Science and Sport of the Republic of Slovenia; from the National Science Council and the Ministry of Education of Taiwan; and from the U.S. Department of Energy.

*On leave from Nova Gorica Polytechnic, Nova Gorica.

[1] BaBar Collaboration, B. Aubert *et al.*, Phys. Rev. Lett. **90**, 242001 (2003).

[2] CLEO Collaboration, D. Besson *et al.*, Phys. Rev. D **68**, 032002 (2003).

[3] W. Bardeen, E. Eichten, and C. Hill, Phys. Rev. D **68**, 054024 (2003).

[4] In the heavy c-quark approximation, one expects two doublets of $c\bar{s}$ states with quantum numbers $J^P = 0^+, 1^+$ $(j = 1/2)$ and $J^P = 1^+, 2^+$ $(j = 3/2)$. The second doublet has already been observed in DK and D^*K decays [5].

[5] Particle Data Group, K. Hagiwara *et al.*, Phys. Rev. D **66**, 010001 (2002).

[6] J. Bartelt and S. Shukla, Annu. Rev. Nucl. Part. Sci. **45**, 133 (1995).

[7] Belle Collaboration, K. Abe *et al.*, hep-ex/0307021 (to be published).

[8] R. Cahn and D. Jackson, Phys. Rev. D **68**, 037502 (2003).
[9] T. Barnes, F. Close, and H. Lipkin, Phys. Rev. D **68**, 054006 (2003).
[10] E. Beveren and G. Rupp, Phys. Rev. Lett. **91**, 012003 (2003).
[11] H. Cheng and W. Hou, Phys. Lett. B **566**, 193 (2003).
[12] P. Colangelo and F. Fazio, Phys. Lett. B **570**, 180 (2003).
[13] S. Godfrey, Phys. Lett. B **568**, 254 (2003).
[14] Belle Collaboration, A. Abashian *et al.*, Nucl. Instrum. Methods Phys. Res., Sect. A **479**, 117 (2002).
[15] S. Kurokawa *et al.*, Nucl. Instrum. Methods Phys. Res., Sect. A **499**, 1 (2003).
[16] A. Palano, hep-ex/0309028.
[17] Belle Collaboration, P. Krokovny *et al.*, hep-ex/0308019.

Bibliography

[1] M. Kobayashi and T. Maskawa, Prog. Theor. Phys. **49**, 652 (1973).

[2] A.B. Carter and A.I. Sanda, Phys. Rev. Lett. **45**, 952 (1980); Phys. Rev. **D 23**, 1567 (1981).

[3] B. Aubert et al., Phys. Rev. Lett. **87**, 091801 (2001)

[4] K. Abe et al., Phys. Rev. Lett. **87**, 091802 (2001).

[5] L. Wolfenstein, Phys. Rev. Lett. **51**, 1945 (1983)

[6] Particle Data Group, D.E. Groom et al., Eur. Phys. J. C **15**, 41 (2000).

[7] CLEO Collaboration, B.H. Behrens et al., Phys. Rev. **D 61**, 052001 (2000).

[8] R. Aleksan, et al., Phys. Rev. **D 62**, 093017 (2000).

[9] G. ALTARELLI, et al., Nucl. Phys. **B 208**, 365 (1982).

[10] Y. Ushiroda et al., Belle note **273** (1999); Belle note **280** (2000).
S. Nishida et al., Belle note **350** (2000); Belle note **381** (2001); Belle note **423** (2001).

[11] CLEO software document homepage :
http://www.lns.cornell.edu/public/CLEO/soft/QQ/index.html (1998).

[12] R. Itoh, *QQ quick reference for BELLE* (1995).

[13] T. Sjöstrand, "PYTHIA 5.7 and JETSET 7.4 Physics and Manual", CERN-TH.7112/93 (1993).

[14] *"GEANT" Detector Description and Simulation Tool*, CERN program Library Long Writeup W5013 (1993).

[15] B. Casey, Belle note **390** (2001)

[16] G.C. Fox and S. Wolfram, Phys. Rev. Lett. **41**, 1581 (1978).

[17] Belle HOME PAGE, <http://belle.kek.jp/>.

[18] Particle Data Group, D.E.Groom et al., Eur. Phys. J. C **15**, 111 (2000).

[19] B. Aubert *et al.* (BaBar Collaboration), Phys. Rev. Lett. **90**, 242001 (2003).

[20] D. Besson *et al.* (CLEO Collaboration), hep/ex-0305017.

[21] W. Bardeen, E. Eichten, and C. Hill, hep-ph/0305049.

[22] In the heavy c-quark approximation, one expects two doublets of $c\bar{s}$ states with quantum numbers $J^P = 0^+$, 1^+ ($j = 1/2$) and $J^P = 1^+$, 2^+ ($j = 3/2$). The second doublet has already been observed in DK and D^*K decays [23].

[23] K. Hagiwara *et al.* (Particle Data Group), Phys. Rev. D **66**, 010001 (2002).

[24] J. Bartelt and S. Shukla, Ann. Rev. Nucl. Part. Sci. **45** 133, (1995).

[25] K. Abe *et al.* (Belle Collaboration), hep-ex/0307012.

[26] R. Cahn and D. Jackson, hep-ph/0305012.

[27] T. Barnes, F. Close and H. Lipkin, hep-ph/0305025.

[28] E. Beveren and G. Rupp, hep-ph/0305035.

[29] H. Cheng and W. Hou, hep-ph/0305038.

[30] P. Colangelo and F. Fazio, hep-ph/0305040.

[31] S. Godfrey, hep-ph/0305122.

[32] S.W. Lin, Belle note **645**

[33] A. Abashian *et al.* (Belle Collaboration), Nucl. Instr. and Meth. A **479**, 117 (2002).

[34] S. Kurokawa and E. Kikutani *et al.*, Nucl. Instr. and Meth. A **499**, 1 (2003).

[35] P. Krokovny, A. Bondar, *et al.* (Belle Collaboration), Phys. Rev. Lett. **91**, 262002 (2003)

[36] A. Palano, hep-ex/0309028.

[37] Isgur and Wise, Phys. Rev. Lett. **66**, (1991), 1130

[38] W. Bardeen, H. Eichten, and C. Hill, Phys. Rev. D **68**, 054024 (2003).

[39] P. Krokovny, *et al.* (Belle Collaboration), hep-ex/0408109